On Contractile Force Developed by the Spasmoneme, a Biological Spring of a Peritrich Ciliate *Vorticella convallaria*

by

Sangjin Ryu

Submitted to the Department of Mechanical Engineering
in partial fulfillment of the requirements for the degree of

Doctor of Philosophy in Mechanical Engineering

at the

MASSACHUSETTS INSTITUTE OF TECHNOLOGY

September 2009

Author .....
Department of Mechanical Engineering
August 31, 2009

Certified by .....
Paul Matsudaira
Professor of Biology and Biological Engineering
Thesis Supervisor

Certified by .....
Matthew J. Lang
Professor of Mechanical Engineering and Biological Engineering
Thesis Supervisor

Accepted by .....
David E. Hardt
Chairman, Department Committee on Graduate Students

On Contractile Force Developed by the Spasmoneme, a Biological Spring of a Peritrich Ciliate *Vorticella convallaria*

by

Sangjin Ryu

Submitted to the Department of Mechanical Engineering
on August 31, 2009, in partial fulfillment of the
requirements for the degree of
Doctor of Philosophy in Mechanical Engineering

Abstract

Vorticella convallaria, a sessile ciliated protozoan, has an about 100 μm long stalk that retracts the zooid toward a substrate in a few milliseconds generating the contractile force in the order of 10 nN. The spasmoneme, the contractile organelle inside the stalk, is a mechanochemical engine employing calcium ions as the energy source. In this thesis, I evaluate the lower and upper bounds of the contraction force of the *Vorticella* stalk and analyze the contraction dynamics and energetics.

The lower limit is the peak contraction force in normal contraction, and Stokes' law was used with the contraction force equated to the drag force on the spherically shrunken zooid. However, contraction-induced water flow does not satisfy approximations for Stokes' law because the Stokes number and Reynolds number greater than unity show that the induced flow is not only transient but also non-creeping and because the visualized flow shows that it is limited by the substrate. Instead of Stokes' law, I employ computational fluid dynamic simulations and propose a contraction force estimation model. Simulation-based estimates reveal that the combined effect of the unsteadiness, finite Reynolds numbers and the substrate comprises 35% of the total force and that the work done in the early phase of contraction and the maximum power output are similar regardless of the medium viscosity.

To measure the upper limit, the isometric force of the spasmoneme, I apply viscous fluid flow to *Vorticella* with a microfluidic channel. As the drag force increases, the cell contracts over shorter distance with lower speed, and latency between the zooid and stalk contraction increases whereas contraction propagation is not affected. The spasmoneme develops the contraction force at a rate of 40$\sim$50 nN/msec. The isometric force, in the order of 100 nN, linearly depends on the stalk length, and this linear dependence (2.5 nN/1 μm of the spasmoneme) enables estimating contractile force per filament of the spasmoneme. In terms of energetics, *Vorticella* in flow behaves differently than it does in stagnant media: the total work is constant regardless of the stall force whereas the maximum power output decreases as the stall force increases.

Thesis Supervisor: Paul Matsudaira
Title: Professor of Biology and Biological Engineering

Thesis Supervisor: Matthew J. Lang
Title: Professor of Mechanical Engineering and Biological Engineering

Acknowledgments

For the past five years in MIT, I have been able to well manage my life and research because there has been help and support from many great people. They made my five years in MIT one of the best times in my life.

I would like to thank my advisor Prof. Matsudaira for his support from many aspects. With patience, Paul allowed me to find questions about the research topic and to develop the questions into my thesis research. I thank Prof. Lang, my co-advisor and thesis committee chair. Having been friendly and supportive, Matt always tried to help me in my research and life. I also appreciate insightful comments of other committee members, Prof. Kamm and Prof. Grodzinsky.

My colleagues in the Matsudaira laboratory should be acknowledged. Help and guidance from Valeria Baru was indispensable in my *Vorticella* experiments. Danielle France introduced the *Vorticella* project to me and helped me start my own research. Michael Murrell, who has a good sense of humor, and Mariya Barch, who had the thesis defense on the same day, shared with me the end of the Matsudaira group. I appreciate other members: Alec Robertson, Guillermina Waller, Kazuyoshi Murata, Yelena Freyzon, James Evans, Nicki Watson, Winston Timp, Barney Tam, Mekhail Anwar, Ben Zeskind, Taro Muso, Jennifer Shin and Robert Burger. I also thank the Lang group members for their hospitality and my collaborators, Moeto Nagai, Rachel Pepper and Yoonsung Nam, for broadening my research on *Vorticella*.

My life in MIT was not boring because of many friends. I thank all of them. Especially, I thank my lunch/dinner family, Kanghyeun Ji and Dongchul Kim, for all the chats that we have had. I appreciate the effort of MIT KGSA Korean Class teachers to continue the class that I started.

Finally, I would like to thank my families. My families in Daejeon made me smile even when I had hard times. I also thank my in-laws in Incheon for their encouragement. I cannot thank enough my wife Eunjeong for her support and love. I also thank my son-to-be-born for giving me one of the biggest joys in my life.

THIS PAGE INTENTIONALLY LEFT BLANK

Contents

THIS PAGE INTENTIONALLY LEFT BLANK

List of Figures

THIS PAGE INTENTIONALLY LEFT BLANK

List of Tables

THIS PAGE INTENTIONALLY LEFT BLANK

Chapter 1

Introduction

1.1 How do cells move?

Cells have evolved diverse spectrum of motility [12, 26, 36]. Bacteria such as *Escherichia coli* swim around by rotating flagella, and eukaryotic cells such as spermatozoa also use their flagellum to move but in different ways from bacteria. They propagate waves along the length of their flagellum. Besides a long flagellum, many microscopic swimmers have hair-like cilia. Protozoa such as *Paramecium* use coordinated cilia beating for feeding and moving. In contrast to swimming protozoa, some unicellular animals such as *Amoebae* crawl or glide over a surface. Motile cells such as fibroblasts and white blood cells in a multicellular animal also adopt crawling to move through the extra cellular matrix or over the other cells [52]. They repeat cycles of ① extending their leading edge (pseudopodia or lamelipodia) over the substrate, ② attaching to the substrate by forming adhesion points, ③ pulling the rest body using the adhesion points and ④ releasing the adhesion points at the rear of the cell. On the other hand, animals sustain their life relying on the contraction of muscle cells: heart muscle for blood circulation and skeletal muscle for locomotion.

These cellular motions are based on a few common motors or motility mechanisms. Bacteria have flagella motors of which the energy source is the gradient of photons across the plasma membrane. Crawling cells protrude their leading edge by polymerizing actin dimers into filaments. Bacterium *Listeria* takes advantage of

this actin-polymerization mechanism inside its host cell to move inside the host's cytoplasm. Sperms of sea cucumber *Thyone* project the acrosomal process for fertilization based on actin polymerization. Force needed for mitosis is generated by the polymerization and depolymerization of microtubule. Besides force generation due to polymerization, these cytoskeletal filaments play a role as tracks for motor proteins. Muscle contraction is based on the movement of myosin on actin filaments. Organelle transport inside a cell is motored by the interaction between kinesin or dynein and microtubule. The motion of eukaryotic cilia and flagella is the result of sliding among tubulin filaments, and dynein enables this sliding. These motor proteins use ATP[1] as an energy source and convert chemical energy from ATP to mechanical motion, force and power.

Besides aforementioned motility mechanisms, some cells rely on unusual engines called biological springs [60]. In these springs, energy is stored in a form of conformation in chemical bonds that latch the energy, and it is released and converted into mechanical motion and force when the bonds are unlatched. During this process, small changes of the spring's subunits are amplified by the spring's geometry and structure. The acrosomal process of sperm cells of horseshoe crab *Limulus polyphemus* is an example of the biological spring [86]. A bundle of actin filaments is coiled inside the cell, and at fertilization this bundle extends from the cell up to 60 μm in about 5 seconds reacting the presence of calcium ions. As the bundle uncoils, the elastic energy stored in the coiled state is released and used to push the membrane and to penetrate the jelly coat of an egg. The bundle generates penetrating force up to 2 nN [87]. Another impressive biological spring is the contractile stalk of *Vorticella convallaria*.

1.2 *Vorticella convallaria*

The stalk of this sessile ciliate protozoan contracts incredibly fast (Figure 1-1). Besides the stalk, *Vorticella* has a bell-shaped body, called the zooid, and this zooid

[1] Adenosine triphosphate.

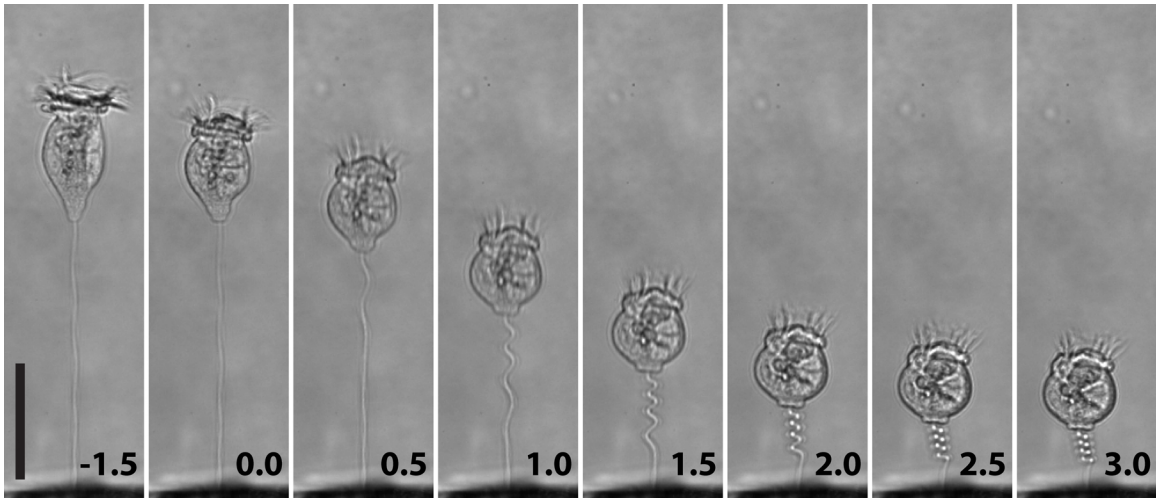

Figure 1-1: Sequential images of *Vorticella convallaria* contracting in water. Usually contraction begins from the zooid, which shrinks to a spherical shape, and propagates along the stalk toward the stalk base. The zooid rotates after contraction is completed (not shown in the figure) [67]. Time is listed in msec, and the stalk begins to coil at 0 msec. The size of the scale bar is 50 μm.

is tethered to a substrate by the stalk. During contraction, the stalk shortens to about 20∼40% of its extended length, and the zooid also shrinks. The contracted zooid is usually about 15∼20 μm in radius, and the stalk is 3∼4 μm in diameter and about 100 μm in length. Because contraction is completed in a few milliseconds, the maximum contraction rate is on the order of cm/sec whereas stalk relaxation takes a few seconds [45, 67, 95]. Figure 1-2 compares the stalk contraction of *Vorticella* with other motile cells and their motility mechanisms in terms of velocity and force, and *Vorticella* is unbeatable. In terms of specific power, the stalk of *Vorticella* performs better than typical passenger cars and striated muscle do [60]. Therefore, the *Vorticella* stalk is regarded as a candidate for biomimetic actuators [49]. In addition to *Vorticella*, *Carchesium* and *Zoothamnium* show similar stalk contraction, and their phylogenetic relations has been studied based on small subunit rRNA gene sequences [20, 40, 54].

The spasmoneme, the contractile organelle inside the stalk shown in Figure 1-3(b), is responsible for the stalk contraction of *Vorticella*. The spasmoneme consists of 2∼4 nm diameter fibers and tubules (Figure 1-3(c)) [3]. Underneath the sheath

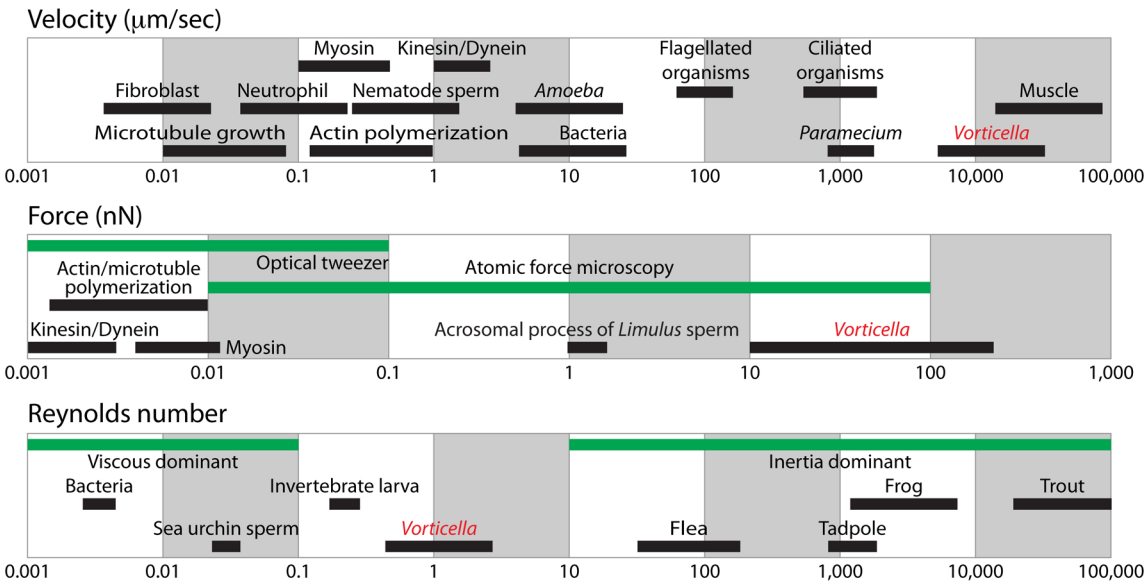

Figure 1-2: A comparison of key physical parameters of various motile cells and animals [11, 12, 17, 36, 60, 107].

surrounding the stalk, longitudinal fibers, the bâtonnets, are placed on the opposite side to the spasmoneme [3]. When contraction is triggered, the spasmoneme shortens taking the shortest path through the stalk sheath, and as a result the stalk coils helically and retracts the zooid toward the substrate [97]. Whereas the spasmoneme generates force for contraction, the driving force for the reextension of the stalk is the elastic recovery of the sheath [2].

Besides its speed and power, the contraction of *Vorticella* is distinctive because its energy source is not ATP but calcium ions. Studies using extracted models of *Vorticella* showed that the permeabilized stalk coils in the absence of ATP and that the stalk end-to-end length depends on the free calcium ion concentration of the medium [35]. The extracted stalk remains extended when $[Ca^{2+}]_{free} < 10^{-8}$ M and coiled when $[Ca^{2+}]_{free} > 10^{-6}$ M, and this process can be repeated with hysteresis by the changing free calcium ion concentration (Figure 1-4(a)) [9, 72]. The tension developed by the extracted stalk also shows hysteresis (Figure 1-4(b)) [69]. In contrast to extracted models, live *Vorticella* can repeat the contraction-relaxation cycle even in media deprived of calcium ion because calcium is stored in membraneous tubules

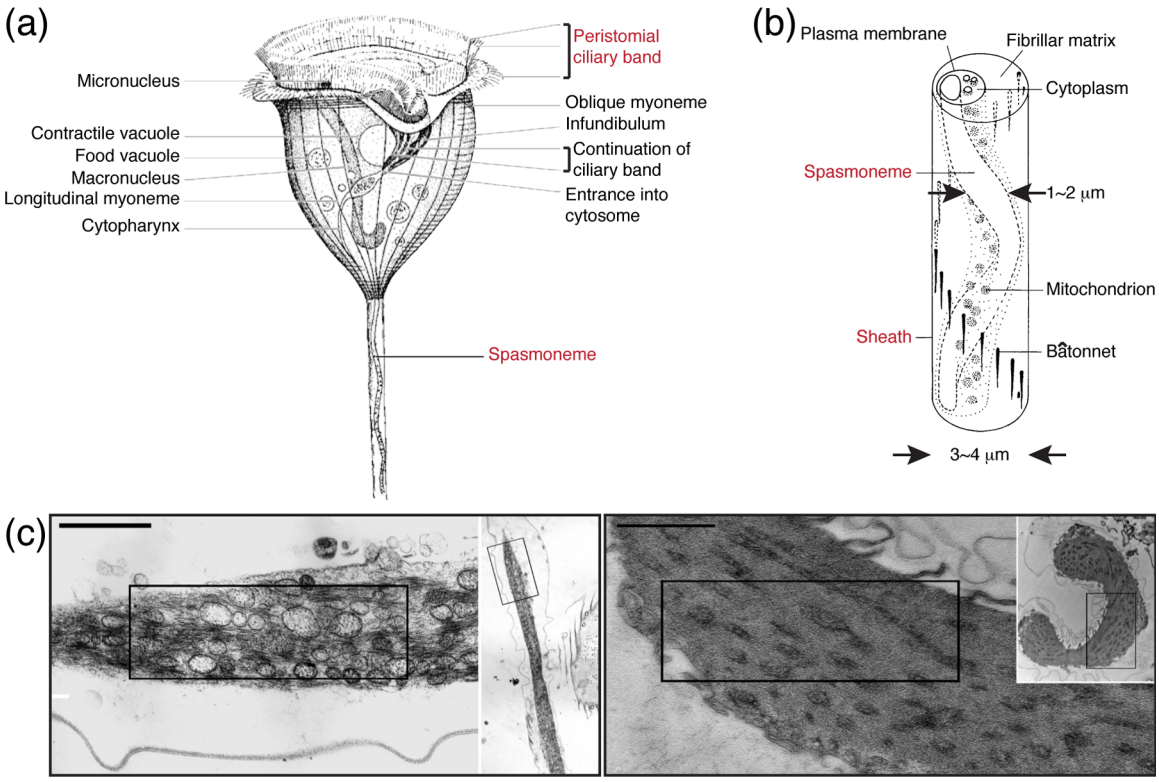

Figure 1-3: The anatomy of *Vorticella convallaria*: (a) A diagram of the zooid (the figure from [15]). (b) A diagram of the stalk (the figure from [3]). (c) Images of the spasmoneme in the extended (left) and contracted (right) state (the images from [27]). The size of the scale bar is 500 nm.

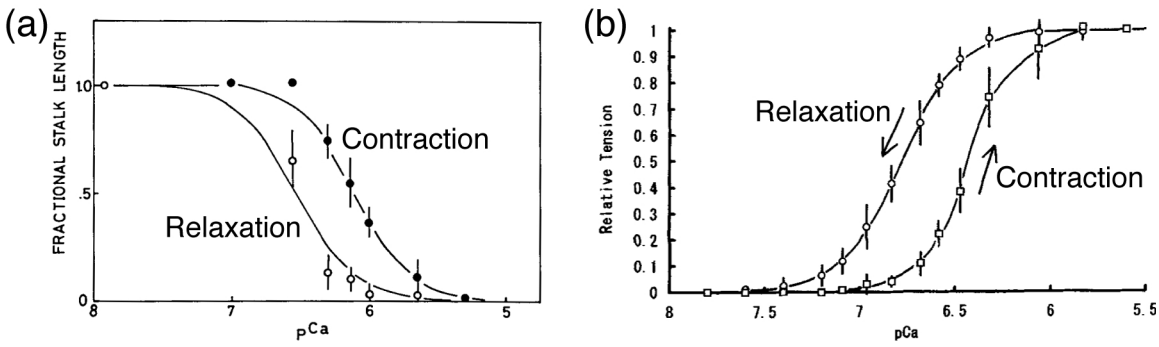

Figure 1-4: Calcium dependency of extracted *Vorticella convallaria*: (a) The end-to-end length of the stalk (the graph from [72]). The fractional stalk length, which is defined in Eq. 3.6, is 1.0 when the stalk is relaxed and 0 when the stalk is fully contracted. (b) The tension developed by the extracted stalk (the graph from [67]). The relative tension is the tension of the stalk normalized with its maximum. Here, $\mathrm{pCa} = -\log_{10}[\mathrm{Ca}^{2+}]_{\mathrm{free}}$.

inside the spasmoneme [3, 16]. Once contraction is triggered, calcium seems to be released from the intracellular storage sites, which are tubules of the spasmoneme [3, 44]. During relaxation, released calcium seems to be pumped back to its storage organelle by consuming ATP [68, 79].

It has been known that the extended spasmoneme has positive birefringence with respect to its length and that the birefringence vanishes during contraction [2]. This spasmoneme birefringence is due to form birefringence, which indicates that oriented structures of the spasmoneme are responsible for the birefringence [79]. This suggests that contraction is related with folding of structures rather than sliding of filament [4]. Amos argued that this structure cannot be nanoscale filaments of the organelle because they mostly remain longitudinal even in maximum contraction [3]. Instead, the birefringence change may be caused by a structural change with the filaments or other structures. Recently, France measured the birefringence of the spasmoneme with a high resolution polarization microscope, and she observed that the fully coiled stalk is still birefringent [27].

The stalk contraction commences from the junction of the zooid and the stalk, and it propagates along the stalk toward the base of the stalk (Figure 1-1). Sugi measured the contraction propagation speed of *Carchesium polypinum* by tracking the motion of particles adhered to the stalk [96]. The speed was in the range of 20$\sim$50 cm/sec in most normal cells. This contraction propagation is thought to be related to a signal triggering contraction. Candidates for a contraction triggering signal are a calcium ion wave related to calcium-induced calcium release [45], an electrical signal due to membrane potential change [66, 88] and protein conformation change propagating inside the spasmoneme [61]. However, Upadhaya et al. argued that calcium-induced calcium release is too slow to explain the response time of live *Vorticella* [104]. Having measured that the large pulse of membrane potential change always lagged behind the contraction of *Vorticella*, Shiono and Naitoh concluded that the large pulse does not trigger contraction [89]. On the other hand, Ochiai et al. suggested that this propagation of stalk coiling may be due to a difference of the spasmoneme's binding affinity to calcium ions along the stalk or the relative rigidity of the sheath [72].

1.3 Motor proteins and contraction models

A major protein composing the spasmoneme is spasmin, a 20 kDa EF-hand calcium binding protein [5]. A molecule of spasmin binds to about two calcium ions[2] [5, 9, 78]. Besides spasmin, the spasmoneme has putative spasmin-receptor protein named spaconnectin [8, 7, 24, 68]. The molecular weight of this protein is 190∼200 kDa for *Carchesium*, 90∼100 kDa for *Zoothamnium* and 50 kDa for *Vorticella* [7]. Although spasmin is thought to be a motor protein of the spasmoneme because of its abundance and affinity to calcium ion, there is no direct evidence that spasmin and spaconnectin are responsible for the spasmonemal contraction of vorticellidae.

Spasmin is a homolog of centrin, another EF-hand calcium binding protein ubiquitously found in eukaryotic cells [8, 50, 84]. Therefore, understanding centrin-based motility will lead us to better understanding of the contraction mechanism of *Vorticella*. Centrin (also known as caltractin in some organisms) is a highly conserved 20 kDa phosphoprotein [51, 80, 84]. In contrast to spasmin having two Ca^{2+} binding sites, centrin has four Ca^{2+} binding sites [39, 57]. Centrin is found in microtubule-organizing centers (MTOCs)-basal bodies of flagellated or ciliated cells, spindle pole bodies (SPBs) of yeast cells and centrosomes of higher eukaryotes-and Ca^{2+}-sensitive contractile filaments within and attached to MTOCs. The role of centrin is related to centrosome (basal body) duplication and separation during cell division, and microtubule severing during flagellar excision. Because the centrin-based fibers twist and supercoil, the mechanism of centrin-based contraction is dissimilar from the sliding filament mechanism of muscle contraction and the sliding microtubule mechanism of cilia and flagella [81].

[2]The contraction curve of Figure 1-4(a) can be expressed with Hill's equation give as

$$L^* = \frac{1}{1 + \left(\frac{[Ca^{2+}]_{\text{free}}}{K_m} \right)^n} \tag{1.1}$$

where L^* is the fractional stalk length (as defined in Eq. 3.6), $[Ca^{2+}]_{\text{free}}$ is the free calcium concentration, K_m is the dissociation constant, and n is Hill's parameter [72]. Having estimated that $n = 2$, Ochiai et al. suggested that two calcium ions cooperatively bind to a contractile element of the spasmoneme.

Centrin has binding partners, and this binding protein seems essential for centrin to form contractile nanofilaments. Yeast *Saccharomyces cerevisiae* has one centrin Cdc31p, and there are several Cdc31p-binding proteins. Among them, Sfi1p, a 120 kDa polypeptide, has about 20 repeats of the binding site (AX_7LLX_3F/LX_2W) to which a molecule of Cdc31p directly binds at low free Ca^{2+} concentration [47, 55, 82]. This centrin-binding protein having α helices may play a role as a short filament scaffold for Cdc31p and undergo conformation changes responding to the elevation of Ca^{2+} concentration. This conformational change may lead to a rapid coiling of the filament. Human cells have centrins, and HsCen2 binds to not only Sfi1p but also its own binding partner HsSfi1p which is a vertebrate homolog of Sfi1p [62]. Centrin is also present in the infraciliary lattice (ICL) of *Paramecium tetraurelia*, and its PtCenBP1p is an Sfi1p-like 460 kDa protein [30]. Being a major component of the contractile ICL, this centrin-binding protein of *Paramecium* forms the backbone of the lattice. Being similar to centrin, spasmin has its binding partner spaconnectin, but it is not known whether the binding site of spaconnectin has a sequence similar to that of Sfi1p.

Knowing the molecular mechanism of the spasmonemal contraction is crucial to in vitro reconstruction of the contraction mechanism and its engineering application such as nanoscale actuators. Several models have been suggested so far for the spasmonemal contraction and centrin-based contraction. In the electrostatic model that Hoffman-Berling proposed, calcium ions neutralize negatively charged filaments, which are aligned in parallel in the spasmoneme due to electrostatic repulsive force, leading them to collapse (Figure 1-5(a)) [35]. Tendency to increasing entropy drives this collapse and generates force. However, this model cannot explain the spasmoneme's specificity for calcium ion and its reaction over a wide range of ionic strength of the medium [34, 79]. Weis-Fogh and Amos suggested an entropic rubber model based on their birefringence and length/tension measurement on the spasmoneme [111]. According to this model, the spasmoneme consists of polypeptides free to fold responding to calcium ion change and stable cross-links connecting these polypeptides in a nonrandom fashion [4]. A drawback of this rubber model

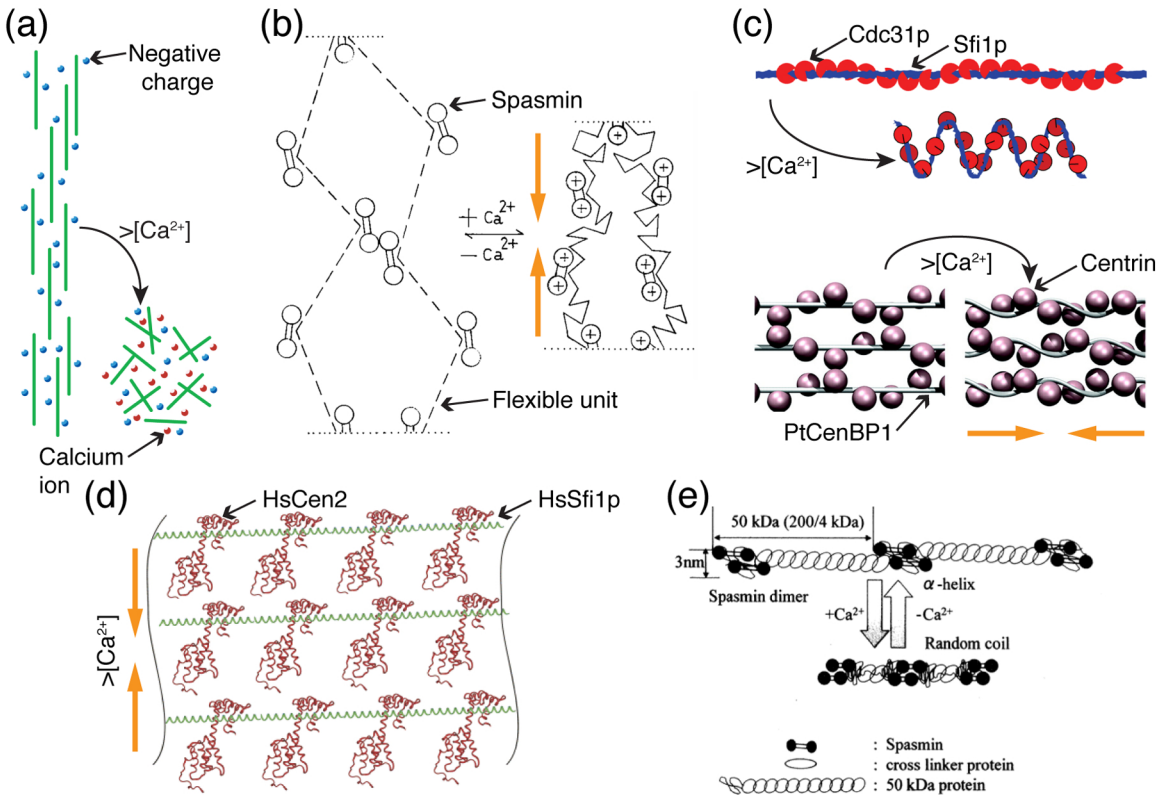

Figure 1-5: Suggested models for the spasmoneme or related centrin-based contraction: (a) The electrostatic model based on the concept of the entropic spring (the figure from [60]). (b) The rubber-like elastic model suggested for the *Vorticella* spasmoneme (the figure from [68]). (c) Models suggested for the Cdc31p-Sfi1p complex (Top, the figure from [82]) and the contraction of *Paramecium* (Bottom, the figure from [30]). (d) A model suggested for the HsCen2-HsSfi1p complex (the figure from [62]). (e) A model suggested for the *Vorticella* spasmoneme (the figure from [6]).

is that it cannot explain why the birefringence of the spasmoneme is mostly form birefringence [79]. By applying the rubber-like elasticity theory, Moriyama et al. proposed that the intramolecular folding of contractile elements induced by calcium binding is the contractile mechanism of the spasmoneme (Figure 1-5(b)) [68]. These models are based on the filamentous structure of the spasmoneme, but they do not consider the components of those filaments. The discovery of Sfi1p resulted in two-component models of centrin-based contraction (Figure 1-5(c) and (d)). These models assume that a molecular thread consists of a Ca^{2+}-responding regulator (centrin) and a pliable backbone (centrin-binding protein). Because the backbone has repeated centrin-binding sites with a certain spacing, multiple molecules of centrin bind to the backbone at low free Ca^{2+} concentration. Influx of Ca^{2+} ions induces the conformation change of the regulator molecules leading to the deformation of filaments. When the free Ca^{2+} concentration decreases to the lower level, the filaments relax as the regulator molecules return to the original state. In the models proposed by Kilmartin and Gogendeau et al., centrin molecules interact with neighboring centrin molecules on the same thread, so the filament shortens by twisting and bending [30, 47]. In contrast, Martinez-Sanz et al. suggested that centrin molecules interact with adjacent centrin molecules belonging to other neighboring threads, so shortening occurs among filaments [62]. When it comes to the spasmoneme, Asai proposed a two-component model (Figure 1-5(e)) [6]. The contractile filaments of the spasmoneme consist of dimers of spasmin and α-helix of spaconnectin connecting the dimers. As the free Ca^{2+} concentration increases, spaconnectin molecules become random coils, so the filament shortens. Although plausible, these models should be experimentally verified with in vitro assays.

1.4 Contraction Force Estimations

1.4.1 Experimental measurements

The contraction force of *Vorticella* is one of the key parameters to characterize the mechanics of *Vorticella* contraction, and it is a physical bound for any possible model of *Vorticella*'s contraction mechanism. The contraction force was measured with extracted *Vorticella* cells or other similar but bigger protozoa such as *Carchesium* and *Zoothamnium* because the size of *Vorticella* and its fast contraction make it challenging to measure the contraction force of live *Vorticella*. Ueda measured the tension of live *Carchesium polypinum*'s spasmoneme to be $9\sim15\times10^4$ N/m^2 [102]. Rahat et al. measured tension developed by contracting live *Carchesium* to be $4\sim8\times10^4$ N/m^2 [77]. Moriyama et al. used a glycerinated stalk of *Vorticella convallaria* and suggested that the isometric tension is 40 nN on average and 120 nN at maximum [69]. This range corresponds to the isometric tension of $3.5\sim5.1\times10^4$ N/m^2.

Recently, France attempted to measure the maximum contraction force of live *Vorticella convallaria* with two methods [27]. The first method was to apply centrifugal force to the cells in the direction opposite to contraction. Having observed that *Vorticella* in water could contract even at 11,477 **g**, where **g** is the gravitational acceleration (9.8 m/sec^2), France evaluated that the cell can generate the contraction force up to 350 nN. In the second method, France held the zooid with a micropipette of known bending stiffness to stall or slow down contraction, so *Vorticella* had to bend the micropipette to contract. Based on extrapolation of the bending force over stalk length ratio, a ratio of the end-to-end length of the contracted stalk to that of the extended stalk, France suggested that the isometric force of live *Vorticella* is about 180 nN. It is noticeable that France's values are one order of magnitude greater than Moriyama et al.'s measurement. Although Moriyama et al. argued that extracted cells can represent live cells in terms of contraction force generation [67], this difference in the isometric force discriminates live *Vorticella* from extracted ones.

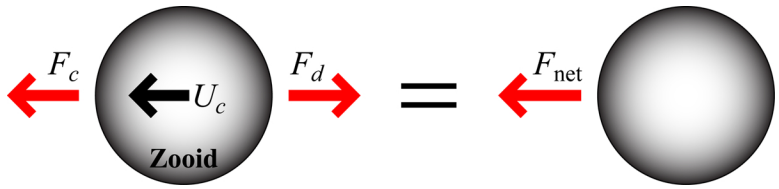

Figure 1-6: Forces acting on the moving zooid in normal contraction. F_c is the contractile force of the stalk, F_d is the drag force from the viscous medium, U_c is the contraction speed of *Vorticella*, and F_{net} is the net force on the zooid.

1.4.2 Estimations based on Stokes' law

Instead of experimentally measuring the contraction force, one can estimate the force based on a measured contraction speed by equating the contraction force to the drag force on the zooid (Figure 1-6). This is possible because the inertia of the zooid is negligibly small as the following:

$$m_z \frac{dU_c}{dt} = F_c - F_d \xrightarrow{m_z \dot{U}_c \ll F_c} F_c \approx F_d \tag{1.2}$$

where m_z is the mass of the zooid, U_c is the contraction rate of the stalk, equal to the moving velocity of the zooid, t is time, F_c is the contractile force of the stalk and F_d is the drag force exerted on the zooid by a surrounding fluid.

Assuming the shrunken zooid to be a rigid sphere moving in otherwise quiescent water, Amos estimated minimum work done by one contraction to be 0.69 pJ with Stokes' law given as

$$F_d = -6\pi\mu R U_c \tag{1.3}$$

where μ is the viscosity of the fluid, and R is the radius of the contracted zooid [2]. This contraction rate is negative because the stalk shortens during contraction. The negative sign of Eq. 1.3 means that the drag force is exerted in the direction opposite to the zooid motion. Based on values that Amos chose based on Jones et al.'s measurement [41] ($R = 20$ μm, $U_c = -2.3$ cm/sec), the contraction force is calculated to be 8.6 nN (1.1×10^4 N/m^2) [5]. Because the contraction velocity used in Amos' calculation is an averaged value, the estimated force can be regarded as averaged.

Moriyama et al. also employed Stokes' formula ($R = 25$ μm, $|U_c|_{\max} = 8.8$ cm/sec) and evaluated that the force generated by the stalk of *Vorticella convallaria* is 55.8 nN, which is greater than their isometric force measurement [69, 67]. As Routledge et al. pointed out, this force estimation is the lower bound of the spasmonemal contractile force because the spasmoneme must generate more force to overcome elastic resistance of the sheath and internal viscous resistance of the stalk [79].

Having realized that the contraction-induced flow is unsteady, Upadhyaya et al. used the unsteady Stokes drag formula given as [104]

$$F_d(t) = -6\pi\mu R U_c(t) - \frac{2}{3}\pi\rho R^3 \frac{dU_c(t)}{dt} - 6R^2\sqrt{\pi\mu\rho}\int_0^t \frac{dU_c(t)}{dt}\Big|_{t=s} \frac{ds}{\sqrt{t-s}}. \qquad (1.4)$$

The first term on the right-hand side is the quasi-steady Stokes drag force based on the instantaneous velocity, and the second term is the added mass force that the sphere experiences due to accelerating the surrounding fluid. The last term is called the history force related to growth of a viscous boundary layer on the sphere, and it shows the memory effect of the fluid. Although Upadhyaya et al. discussed the unsteady effect, they used Eq. 1.3 in calculating the contraction force and mechanical power output of *Vorticella convallaria* because in their analysis the history force accounted for at most 20% of the total force in the case of contraction in water. Upadhaya et al. suggested that the contraction of *Vorticella* is power-limited because the maximum power output is similar regardless of the medium viscosity.

1.5 Research scope and goals

The main goal of this thesis is to estimate force developed by the stalk of contracting *Vorticella convallaria*. There are two limits in the contraction force: the lower bound is the peak contraction force developed during *Vorticella*'s normal contraction, and the upper bound is the isometric force that the *Vorticella* stalk develops when its contraction is completely stalled. Therefore, this thesis consists of two parts.

The first part deals with estimating the lower bound. In Chapter 2, flow induced

by contracting *Vorticella* is visualized based on the particle tracking velocimetry technique, and the effect of *Vorticella*'s residence substrate is demonstrated. In Chapter 3, after limitations of using the Stokes drag formula are discussed, as an alternative, the computational fluid dynamics simulation is employed for the lower bound estimation. The simulation result shows that the *Vorticella* stalk generates the contractile force greater than the Stokes drag and confirms that the stalk contraction of *Vorticella* is power-limited. In Chapter 4, I propose a new fluid dynamic model to estimate the contraction force developed during normal contraction.

The second part of the thesis is related to stalled contraction of *Vorticella convallaria*. In Chapter 5, it is explained how to measure the isometric force of the *Vorticella* stalk by applying viscous drag force to the cell with a microfluidic channel. The measured isometric force suggests that the isometric force depends on the relaxed stalk length, and its biophysical meaning is also discussed. In Chapter 6, the contraction dynamics and energetics of stalled *Vorticella* are investigated. It appears that, as the stall force increases, *Vorticella* contracts over a shorter distance with a lower speed taking a longer time whereas the propagation of the stalk contraction is not significantly affected by the stall force. Furthermore, the stalk contraction of *Vorticella* seems to be limited in the total work, not in the maximum power, in the viscous fluid flow. Finally, in Chapter 7, main results of this thesis are summarized, and a future work is suggested.

Chapter 2

Visualization of Contraction-induced Flow

2.1 Introduction

Vorticella convallaria generates two kinds of flow: flow generated by peristomial cilia beating for food collection (Figure 2-1(a)) and flow induced by contraction for an unknown reason. Sleigh and Barlow observed feeding currents of *Vorticella convallaria* by tracking particles in the vicinity of the zooid [91]. They found that *Vorticella* can move particles that are 450 μm away from the oral part of the zooid. Their particle paths showed that the feeding current is a three-dimensional vortex ring having a torus-like shape (Figure 2-1(b)). According to their measurements, the fluid velocity is on the order of 100 μm/sec near the peristome.

Vopel et al. also measured marine *Vorticella*'s feeding currents as well as seawater flow at several points around the cell caused by the contraction of *Vorticella* [108]. They used a flow microsensor whose diameter was 50 μm, with a response time less than 1 sec. However, the spatial and temporal resolution of their measurement does not seem high enough because the typical zooid size and contraction time of *Vorticella* are about 40 μm and a few msec, respectively. Observing the difference in amount of water moved between fast contraction and slow relaxation of *Vorticella*, they proposed that the contraction-relaxation cycle makes suspended bacteria, food for *Vorticella*,

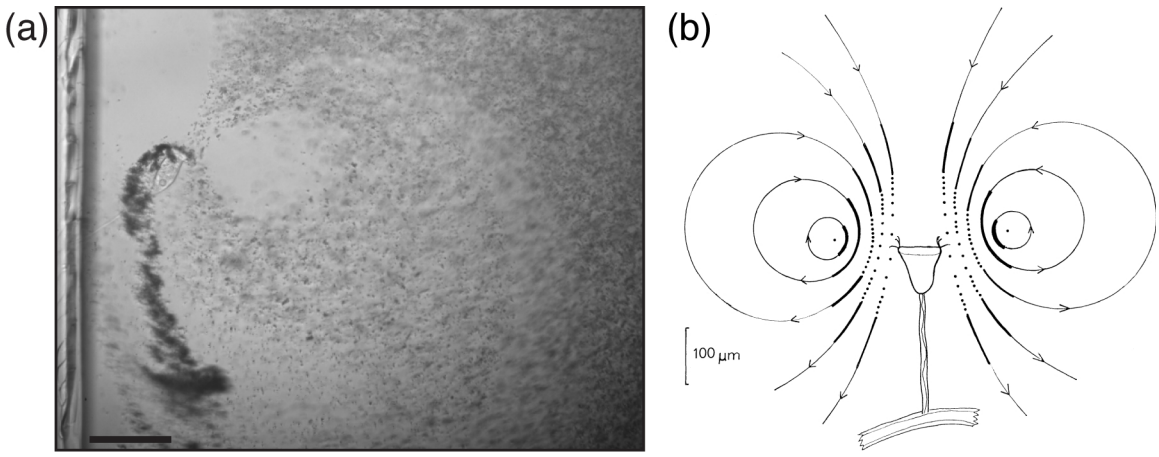

Figure 2-1: The feeding current of *Vorticella*: (a) Feeding current visualized with 1 μm polystyrene beads. The size of the scale bar is 100 μm. (b) Trajectories of particles moved by cilia beating (the image from [91]).

enter into the feeding current.

Recently Nagai et al. measured the feeding current of *Vorticella picta* with the confocal micro-particle image velocimetry (PIV) [71]. They reconstructed the three-dimensional two-component flow velocity field of the current and observed that the flow pattern is similar to the observation of Sleigh and Barlow. Based on their flow rate measurement, Nagai et al. not only discussed the feeding strategies of *Vorticella* but also suggested a possibility of using *Vorticella* as a microscale pump or mixer in microfluidic systems.

On the other hand, Pepper et al. found that eddies of *Vorticella*'s feeding current is due to the influence of boundaries [75]. Although it is unavoidable to sandwich *Vorticella* between pieces of glass for the sake of observation, these top and bottom surfaces play a role as the no-slip boundary. Pepper et al. revealed that the size of the feeding current eddy, i.e., the distance from the cell to the center of the eddy, increases as the spacing between the top and bottom surfaces increases.

Although there have been flow visualization studies about the feeding current, there has bee no such study to visualize flow induced by contracting *Vorticella*. In this study, I employ the particle tracking velocimetry (PTV) technique to visualize water flow around contracting *Vorticella*. Visualized flow will offer information about

the contraction-induced flow required for rigorous estimation of the contraction force.

2.2 Methods

Cell culture and sample preparation

Vorticella convallaria cells are cultured in the laboratory based on the method that Vacchiano et al. proposed [106]. Cells grow in 1 l flasks with about 500 ml wheat fusion solution. The flasks were shaken at about 100 rpm on a shaker for about 24 h so that the zooid abandoned the stalk and became telotroch form. Shaken solution from two flasks was poured into a sterile flask, and cells were allowed to regrow their stalk on the bottom for about 10 h. After that, the solution was changed to about 200 ml inorganic medium (2.4×10^{-4} M KCl, 2.4×10^{-5} M $MgSO_4$, 4.8×10^{-5} M $CaH_4(PO_4)_2 \cdot H_2O$), and the flask was shaken for another 24 h. Cells were filtered with 50 μm Nitex nylon mesh (Lab Pak, Sefar Filtration, Depew, NY), and then the filter was laid on a petri dish filled with spring water (Poland spring, Poland, MA). Pieces of No. 1 cover glass fragment were placed on the bottom of the dish so that cells left on the filter could attach to those fragments [105]. A cell on the vertical side of a fragment was chosen for experiments because its stalk was parallel to the microscope stage and therefore easy to observe.

Ciliary beating inhibition

In this flow visualization experiment, *Vorticella*'s ciliary beating is not desirable because it spreads beads unevenly. Starving *Vorticella* for days or intoxicating the cell with a dynein-related poison can stop the cilia beating. In this study, ammonium vanadate (NH_4VO_3, Fisher Scientific, Pittsburgh, PA) was used which is known to hinder dynein-based cell motility [90]. After being prepared as described in the previous section, the *Vorticella* samples were placed in about 1 mM vanadate solution for about 1 h. Significant reduction in ciliary beating was observed.

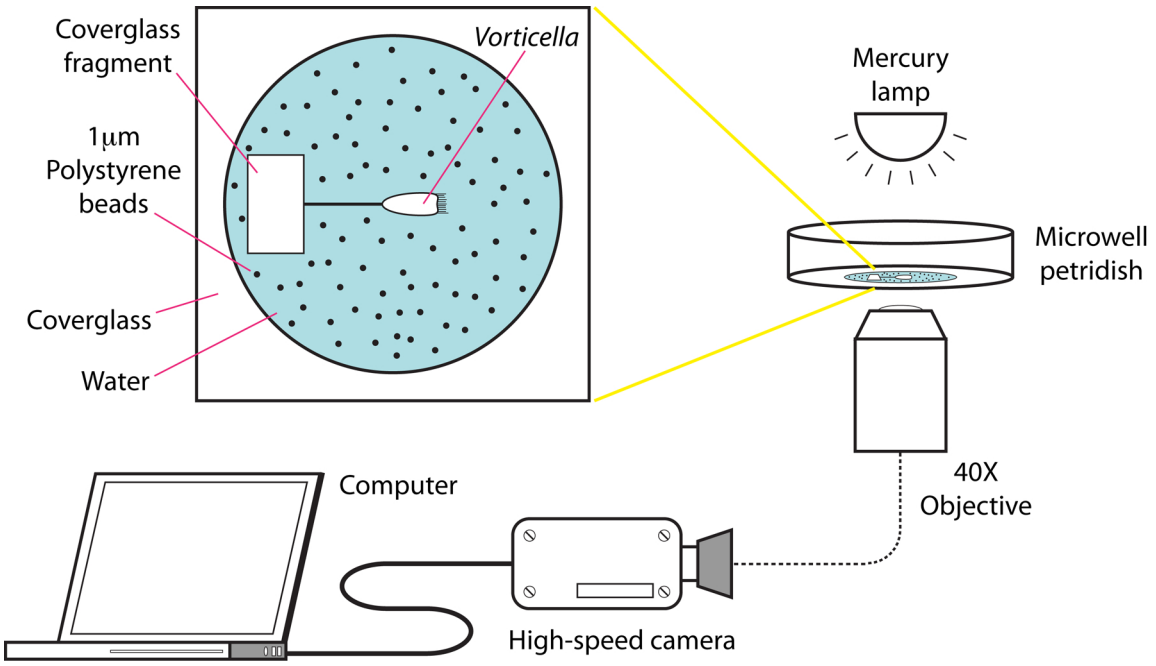

Figure 2-2: A schematic diagram of the flow visualization experiment setup.

Flow visualization

A glass fragment having *Vorticella* on the side was placed in a microwell petri dish (Glass Bottom Culture Dish, MatTek, Ashland, MA) filled with fresh water (Figure 2-2). The bottom of the microwell has the same thickness as No. 1.5 cover glass. As a flow tracer, 1 μm diameter polystyrene beads (1.05 g/cm^3, Bang Laboratories, Fishers, IN) were used. Because the contraction of the *Vorticella* stalk is fast, capturing contraction requires very high temporal resolution [41, 67]. Contractions of the cell were captured at 8123 fps with a high-speed camera (Phantom V7, Vision Research, Wayne, NJ) and an inverted light microscope (Nikon Eclipse TE300, Nikon Instruments, Melville, NY) having a 40× objective lens (NA 0.6). The image size is 512×512 pixels, and at this magnification one pixel corresponds to 0.5 μm. Particle Tracker plug-in of ImageJ (National Institute of Health, Bethesda, MD) was used to identify and track particles [83]. Before particle tracking, raw images were pre-processed with ImageJ to make particles more distinguishable: dim images of particles were removed with Subtract Background command, and the image intensity

was adjusted. MATLAB (The MathWorks, Natick, MA) was used to post-process data obtained from Particle Tracker. In addition to spring water, PVP[3] solutions of 2% and 4% w/w concentration (MW 360,000, Sigma-Aldrich, St. Louis, MO) were used.

2.3 Results

Visualized water flow around contracting *Vorticella* shows that the flow is limited by the substrate (Figure 2-3). As the zooid approaches the substrate, water between the zooid and the substrate is squeezed out, so particles in this region move outward. In contrast, particles above the zooid move inward because water fills up space displaced by the zooid.

Trajectories of seeded particles show how far a contracting *Vorticella* moved the particles (Figure 2-4(a)). Particle paths reconfirm that the induced water flow is confined by the substrate. I also tracked particles for different cells in 2% and 4% PVP solutions and observed that resulting flow patterns are similar (Figure 2-4(b) and (c)).

2.4 Discussion

Understanding the contraction-induced flow of *Vorticella* is indispensable to estimate its contraction force and to identify a biological reason of contraction. Although Vopel et al. measured flow generated by *Vorticella* contraction, there has been no rigorous study on the contraction-induced flow so far because they sampled flow velocity only at several points with low measurement resolution [108]. The current study is the first one to analyze the overall flow field based on flow visualization and CFD simulation.

However, the high contraction speed of *Vorticella* makes it difficult to study the contraction-induced flow experimentally. The micro-PIV/PTV technique is an ideal method to investigate the induced flow because it does not interfere with the flow and

[3]Polyvinylpyrrolidone

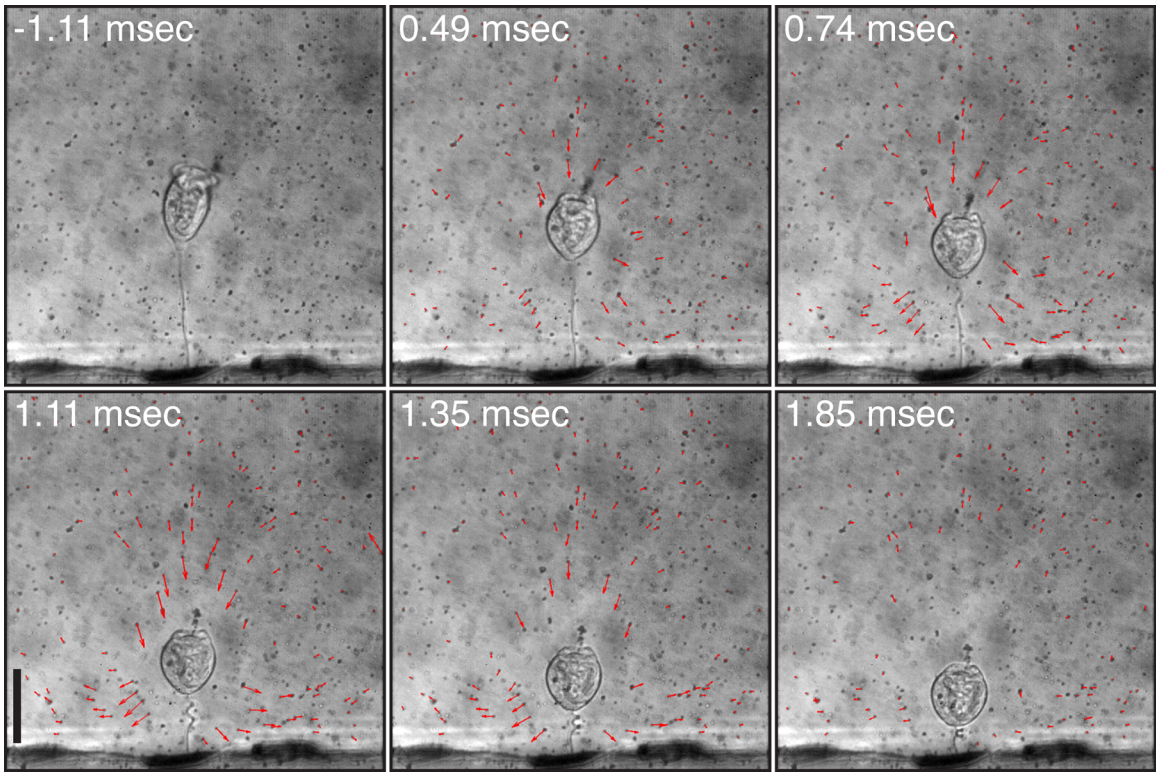

Figure 2-3: Experimentally visualized water flow around contracting *Vorticella*. $t = 0$ msec indicates a point when the stalk begins to coil. The scale of velocity vectors is arbitrary, and the size of the scale bar is 50 μm.

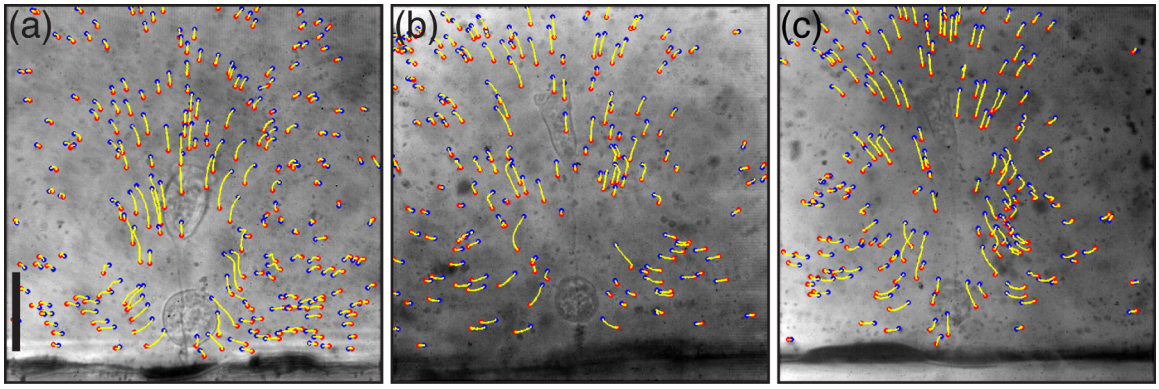

Figure 2-4: Experimentally obtained particle trajectories around contracting *Vorticella* in (a) water, (b) 2% PVP solution and (c) 4% PVP solution. Yellow lines are particle paths, and blue and red dots indicate where particles start and stop, respectively. Images before and after contraction are overlapped. The size of the scale bar is 50 μm.

because it has appropriate measurement resolution. The technique usually employs fluorescent tracers to remove unnecessary information from flow field, but the current study could not use such tracers. Exposure time less than 40 μsec is required to obtain clear images of contracting *Vorticella*, but our preliminary PIV experiment showed that this is not long enough to capture the motion of fluorescent beads. Another problem in using fluorescent beads is that *Vorticella* engulfs a significant number of beads. The zooid after consuming the beads appears too bright compared to other single beads.

Recognizing the aforementioned problems, I tried the bright field PTV technique. This is a compromise between a low signal-to-noise ratio and high temporal resolution. In this case, the depth of field (δ_z) is calculated with

$$\delta_z = \frac{n\lambda_0}{\mathrm{NA}^2} + \frac{n}{\mathrm{M\ NA}}e \tag{2.1}$$

where n is the refractive index of the medium (1 for air), λ_o is the wavelength of light in a vacuum, e is the smallest resolvable distance of the camera sensor (0.5 μm), M is the magnification ratio (40×), and NA is the numerical aperture (0.6) [38]. Because the longest wavelength of intensity peaks of mercury arc lamps is 579 nm, the estimated depth of field is approximately 2 μm. Although this depth of field is comparable to the stalk diameter, obtained images are not as clean as ones that can be obtained with fluorescence because beads out of focus still exist in those images. Although low quality of images resulted in error in tracking beads, pre-processing of raw images and post-processing of identified particle trajectories enabled a qualitative analysis of flow field induced by contracting *Vorticella*. The PIV technique employing a very thin laser sheet or volume illumination will enable more accurate analyses of the contraction-induced flow [28, 64].

THIS PAGE INTENTIONALLY LEFT BLANK

Chapter 3

CFD-based Force Estimation

3.1 Introduction: Stokes' law revisited

It is well known that Eq. 1.3 is valid for steady flow of an unbounded fluid when the Reynolds number is much less than unity. However, water flow induced by contracting *Vorticella* does not satisfy these conditions, and hence contraction force estimates made with Stokes' law can only suggest the order of magnitude of the contractile force. Therefore, I investigate characteristics of the induced flow by revisiting the Navier-Stokes equation that governs incompressible flow of a Newtonian fluid. The equation with the body force term omitted is

$$\rho\Big(\frac{\partial\vec{u}}{\partial t}+\vec{u}\cdot\nabla\vec{u}\Big)=-\nabla p+\mu\nabla^2\vec{u} \tag{3.1}$$

where ρ is fluid density, $\vec{u}$ is flow velocity, t is time, and p is pressure. The equation is nondimensionalized with characteristic length scale L, velocity scale U and time scale τ. Then the variables and operator of the equation become as the following: $\nabla^*=L\nabla$, $\vec{u}^*=\vec{u}/U$, $t^*=t/\tau$ and $p^*=p/(\mu U/L)$, and the Navier-Stokes equation becomes

$$\frac{\rho L^2}{\mu\tau}\frac{\partial\vec{u}^*}{\partial t^*}+\frac{\rho LU}{\mu}\vec{u}^*\cdot\nabla^*\vec{u}^*=-\nabla^* p^*+\nabla^{*2}\vec{u}^*. \tag{3.2}$$

One can judge whether flow is steady or not with the Stokes number (St) defined

as

$$\mathrm{St} = \frac{\rho L^2}{\mu\tau} = \frac{4R^2}{\nu\tau_{\max}} \tag{3.3}$$

where ν is the kinematic viscosity of the fluid. This dimensionless number is the coefficient of the time derivative term of Eq. 3.2, and it represents a ratio of the transient inertia force to the viscous shear force. If $\mathrm{St} \ll 1$, the time derivative term of the Navier-Stokes equation is negligible, so the flow is regarded as steady. In the case of contracting *Vorticella*, L can be the diameter of the zooid ($2R \approx 40$ μm), and τ can be $\tau_{\max}$ which is the time when *Vorticella* reaches its maximum contraction speed (≈ 1 msec). The Stokes number of the induced water flow is about 1.6, which means that the transient inertia force is not negligible compared to the viscous shear force. Therefore, the induced water flow should be regarded as transient.

The second dimensionless number of interest is the Reynolds number (Re) which is

$$\mathrm{Re} = \frac{\rho L U}{\mu} = \frac{2R|U_c|}{\nu}. \tag{3.4}$$

This number represents a ratio of the convective inertia force to the viscous shear force. Therefore, one can judge with the Reynolds number whether flow is viscously dominated ($\mathrm{Re} \ll 1$) or inertially dominated. In the case of contracting *Vorticella*, U can be $|U_c|$. The average Reynolds number of Amos' study is 0.9, and the maximum Reynolds number of Moriyama et al.'s study is 4.4. Although Stokes' law is known to be experimentally valid up to $\mathrm{Re} = 1$ [112], the Reynolds number greater than unity suggests that the induced flow is not a creeping flow any more and that the convective inertia force of the induced water flow plays a role especially when $t \approx \tau_{\max}$.

Furthermore, the induced flow is not infinite but bounded by the substrate of *Vorticella*'s residence as Figure 2-3 shows. Because the thickness of the substrate, which is a No. 1 cover glass fragment, is 0.13∼0.16 mm and its width is infinite compared to the zooid, the substrate area is always large enough to affect flow around *Vorticella*. For the low Reynolds number drag force on an impermeable sphere slowly moving perpendicularly toward a rigid plane, Brenner and Maude separately obtained

the following analytic solution [13, 63]:

$$
\begin{aligned}
&F_d = -6\pi\mu R U_c \lambda \\
&\lambda = \frac{4}{3}\sinh\alpha \sum_{i=1}^{\infty} \frac{i(i+1)}{(2i-1)(2i+3)} \left[\frac{2\sinh(2i+1)\alpha + (2i+1)\sinh 2\alpha}{4\sinh^2(i+1/2)\alpha - (2i+1)^2\sinh^2\alpha} - 1 \right] \\
&\alpha = \cosh^{-1}\left(\frac{R}{H}\right)
\end{aligned}
\tag{3.5}
$$

where λ is the wall effect correction factor, and H is the distance from the center of the sphere to the plane. In the case of *Vorticella*'s contraction, this gap distance is the sum of the contracted zooid radius and the stalk end-to-end length ($H = R + L_s$). If the gap distance is much larger than the sphere radius, the influence of the surface is negligible. In the case of *Vorticella*, however, the gap distance is about 120 μm ($R \approx 20$ μm and $L_s \approx 100$ μm), several times the zooid radius, so the wall effect correction factor is greater than unity even in the extended state. Hence, the effect of the substrate must not be ignored.

Therefore, Stokes' law can suggest the order of magnitude of the contraction force, and for a rigorous estimation of the contraction force, the combined effect of the unsteadiness, the finite Reynolds number and the substrate should be considered. Although Upadhyaya et al. discussed the unsteady effect in estimating the contraction force of *Vorticella convallaria*, they did not consider the effect of the substrate and the finite Reynolds number [104]. In this study, I adopt computational fluid dynamic (CFD) simulations to estimate the contraction force of *Vorticella convallaria* and to analyze the contraction-induced flow. By solving the governing equations of the contraction-induced flow with appropriate boundary conditions, it is possible to take into account the aforementioned complicated characteristics of the induced flow. For the simulations, I assume that the zooid of contracting *Vorticella* is a rigid sphere unsteadily moving perpendicularly toward a rigid plane (Figure 3-1(a)). By doing so, it is possible to take into account the combined effects of the unsteadiness, the substrate and the finite Reynolds number for more rigorous estimation of *Vorticella*'s contraction force. In this model, the stalk and any other surfaces are not considered.

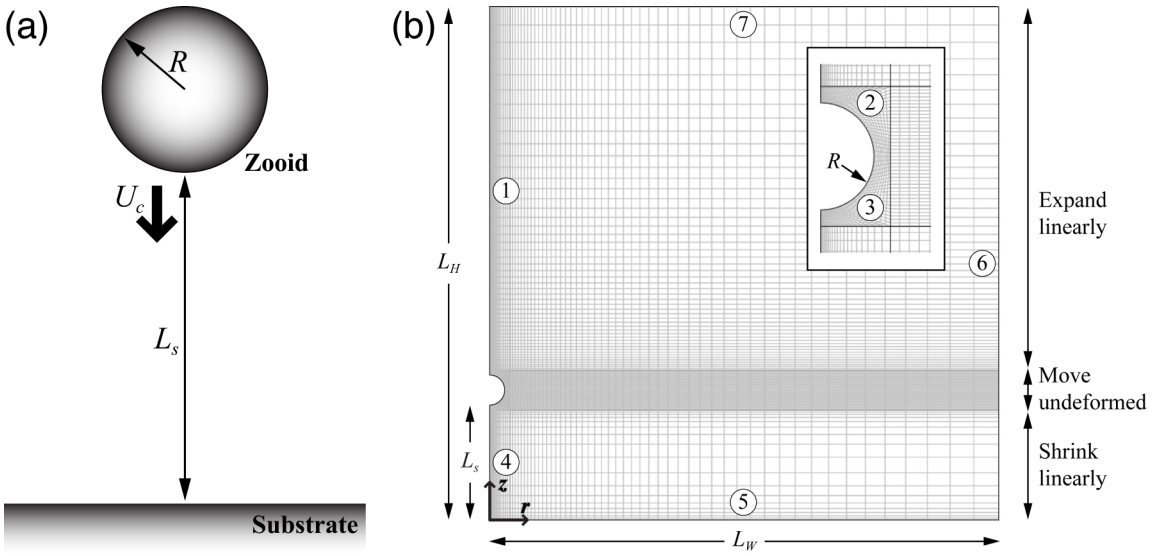

Figure 3-1: The CFD simulation model: (a) A simplified model of contracting *Vorticella*. The sphere of radius R represents the shrunken zooid, and it moves at the contraction velocity U_c perpendicularly toward the rigid plane. The plane represents the substrate which is the stalk length L_s away from the zooid. (b) A two-dimensional axisymmetric mesh used for the CFD simulation. The z-axis is the axis of symmetry. Both the width (L_W) and height (L_H) of the mesh are 512 μm. The inset is a magnified view of the sphere area. The radius of the sphere (R) and the gap distance (L_s) were assigned according to the dimension of *Vorticella*. Elements of the mid-section move downward as a whole according to Eq. 3.7. Assigned boundary conditions are the axisymmetric condition for ① and ④, the no-slip wall condition for ⑤ representing the substrate, the moving wall condition for ② and ③ representing the zooid, and the open condition for ⑥ and ⑦.

In the case of water, using the Stokes drag formula underestimates the peak value of the contraction force by about 35% compared to the CFD-based estimate. In addition to discussing the contribution of the effect of the unsteadiness, finite Reynolds numbers and the substrate, I discuss the energetics of *Vorticella*'s contraction based on the CFD simulation results. Because the work done in the force developing stage and the maximum power output are similar regardless of viscous loading conditions, it is confirmed that the stalk contraction of *Vorticella* is power-limited.

3.2 Methods

PVP solution property

As a viscous liquid, PVP solutions of 1%, 2% and 3% w/w concentration were prepared, and the pH of the solution was titrated to between 6.5 and 7.0 with KOH solution. The viscosity of the PVP solutions was measured with a rheometer (ARG 2, TA Instrument, New Castle, DE) and a ϕ60 mm 2° cone plate at 20°C, and its constant viscosity shows that the prepared PVP solutions are Newtonian. The density of the PVP solutions was measured with a density meter (DMA 38, Anton Paar, Ashland, VA) at 20°C. Table 3.1 shows measured properties of the PVP solutions. 0% PVP solution refers to spring water.

Table 3.1: Properties of the PVP solutions and key fluid dynamic parameters.[4]

PVP wt %	ρ (g/cm^3)	μ (mPa·sec)	$\lvert U_c\rvert_{\max}$ (cm/sec)	$\tau_{\max}$ (msec)	τ_c (msec)	$\mathrm{Re}_{\max}$ (-)	St (-)
0%	1.000	1.00	5.78	0.96	3.9	1.90	1.12
1%	1.001	2.74	3.52	0.90	7.9	0.42	0.44
2%	1.003	6.93	2.39	1.03	13.6	0.11	0.15
3%	1.005	10.31	1.77	1.04	20.3	0.06	0.10

Contraction speed measurement

The contraction rate of a single cell was measured in water and in the prepared PVP solutions. Methods of sample preparation and image acquisition are same as Section 2.2 except frame rate (8000 fps). After several contractions of the cell were captured, the cell was transferred to a different medium. Captured images were processed with ImageJ and MATLAB, and the end-to-end length of the stalk was measured by obtaining the coordinates of the both ends of the stalk from images. Finally, the contraction speed was calculated from stalk length data. For each solution,

[4]The radius of shrunken zooid was measured for each contraction, and its average value ($R = 16.4\ \mu$m) was used for the dimensionless number calculation and CFD simulations. $\lvert U_c\rvert_{\max}$ and $\tau_{\max}$ were obtained from Eq. 3.7, and τ_c was calculated from Eq. 3.6 so that $(L_s(\tau_c) - L_{s,\min})/(L_{s,\max} - L_{s,\min}) = 0.01$.

one representative case was chosen in which the whole stalk lies in the focal plane forming right angle to the substrate. Key parameters of *Vorticella* contraction and related fluid dynamic parameters are shown in Table 3.1.

Stalk length data fitting

It is ideal to represent the measured stalk length and contraction velocity with a single curve. I employed a hyperbolic secant function for the fractional stalk length change:

$$\frac{L_s(t) - L_{s,\min}}{L_{s,\max} - L_{s,\min}} = \left[\mathrm{sech}\left(\frac{t}{c_1}\right)^{c_2}\right]^{c_3} \tag{3.6}$$

where $L_{s,\max}$ and $L_{s,\min}$ are the end-to-end length of the extended and fully coiled stalk, respectively. $t = 0$ indicates a point when the stalk begins to coil. The corresponding velocity curve is

$$\frac{U_c(t)}{L_{s,\max} - L_{s,\min}} = -\frac{c_2 c_3}{{c_1}^{c_2}} t^{c_2-1} \tanh\left(\frac{t}{c_1}\right)^{c_2} \left[\mathrm{sech}\left(\frac{t}{c_1}\right)^{c_2}\right]^{c_3}. \tag{3.7}$$

I obtained values of the coefficients (c_i, $i = 1\sim3$) shown in Table 3.2 by fitting Eq. 3.6 against the experimentally measured stalk length data with the method of least squares. Obtained fitting curves well represent the time course of stalk length and contraction velocity (Figure 3-2).

Table 3.2: The end-to-end length of the extended and contracted stalk, and the values of the fitting curve coefficients.[5]

PVP wt %	$L_{s,\max}$ (μm)	$L_{s,\min}$ (μm)	c_1 (sec)	c_2 (-)	c_3 (-)
0%	116.8	22.5	9.263×10^{-4}	1.243	0.873
1%	115.8	25.2	9.945×10^{-4}	0.915	0.772
2%	114.6	23.0	1.557×10^{-3}	0.781	0.973
3%	113.8	25.5	2.203×10^{-3}	0.697	1.149

[5]The R-square values are greater than 0.999 in all cases. It is noticeable that c_2, a characteristic time scale of Eq. 3.6, has similar values to $\tau_{\max}$ chosen as the characteristic time scale for *Vorticella* contraction in Table 3.1.

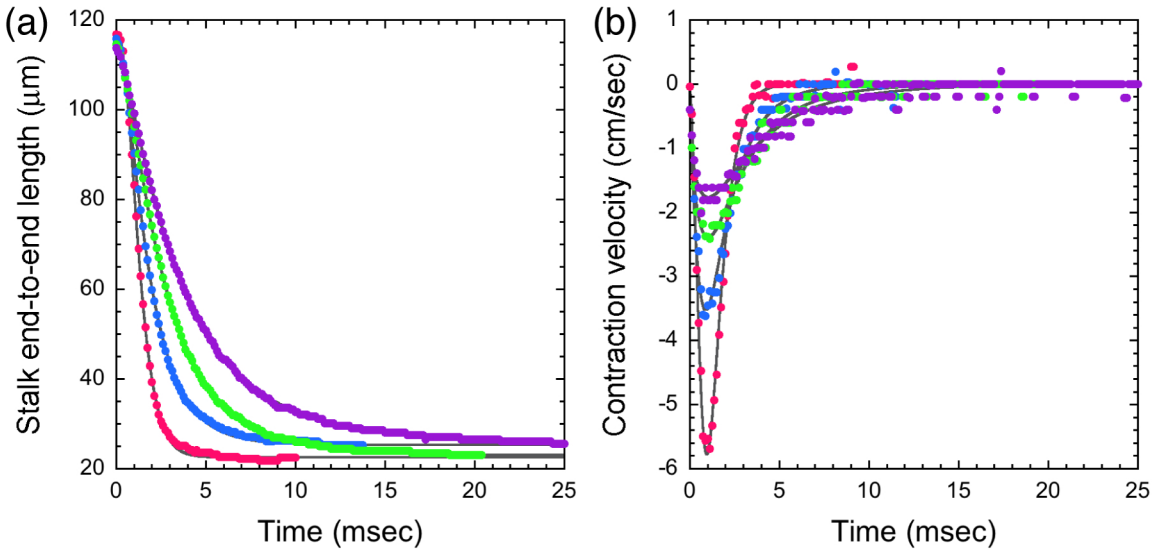

Figure 3-2: Fitting curves for contraction force estimation: (a) The measured end-to-end length change of the stalk and corresponding stalk length curves represented by Eq. 3.6. (b) The contraction rate of the stalk, which is the velocity of the zooid, and corresponding contraction velocity curves represented by Eq. 3.7. The PVP concentration of the medium: red - 0% (1 cP), blue - 1% (2.7 cP), green - 2% (6.9 cP) and magenta - 3% (10.3 cP).

CFD simulation

Governing equations for the induced flow are the Navier-Stokes equation (Eq. 3.1) and the continuity equation for incompressible flow which is

$$\nabla \cdot \vec{u} = 0. \tag{3.8}$$

These equations were solved numerically based on the finite element-method (FEM) with COMSOL Multiphysics and Script (COMSOL, Natick, MA). For the simulation, a two-dimensional axisymmetric mesh including moving interior boundaries was created with rectangular elements (Figure 3-1(b)). The mesh is divided into three subdomains as Thompson et al.'s approach [101]. The middle subdomain including the sphere moves downward as a whole at *Vorticella*'s contraction velocity given as Eq. 3.7, and the other subdomains expand or shrink accordingly in the z-direction. This moving mesh strategy prevents any deformation of elements around the sphere,

which makes the simulation stable. The drag force on the sphere was calculated by integrating the stress over the sphere's surface.

Numerical integration of the history force

Although the quasi-steady force and added mass force can be analytically calculated with Eq. 3.7, the history force requires numerical integration because of its kernel. As Eq. 1.4 shows, the history force has a singularity as s approaches t, so it requires a special treatment in numerical integration. This singularity was evaded in numerical integration by following Kim et al.'s remedy, which is

$$\begin{aligned}
&\int_0^t \frac{\dot{U}_c}{\sqrt{t-s}}ds = \int_0^{N\Delta t} \frac{\dot{U}_c}{\sqrt{t-s}}ds \\
&= \frac{\Delta t}{6}\sum_{i=1}^{N-1}\left[\frac{\dot{U}_{c_{i-1}}}{\sqrt{N\Delta t-(i-1)\Delta t}} + \frac{2(\dot{U}_{c_{i-1}}+\dot{U}_{c_i})}{\sqrt{N\Delta t-(i-0.5)\Delta t}} + \frac{\dot{U}_{c_i}}{\sqrt{N\Delta t-i\Delta t}}\right] \\
&+ \frac{0.9\Delta t}{6}\left[\frac{\dot{U}_{c_{N-1}}}{\sqrt{N\Delta t-(N-1)\Delta t}} + \frac{2(\dot{U}_{c_{N-1}}+\dot{U}_{c_{N-0.1}})}{\sqrt{N\Delta t-(N-0.55)\Delta t}} + \frac{\dot{U}_{c_{N-0.1}}}{\sqrt{N\Delta t-(N-0.1)\Delta t}}\right] \\
&+ \frac{0.1\Delta t}{2}\left[\frac{8\sqrt{2}}{3}\frac{\dot{U}_{c_N}}{\sqrt{N\Delta t-(N-0.05)\Delta t}} - \frac{4}{3}\frac{\dot{U}_{c_N}}{\sqrt{N\Delta t-(N-0.1)\Delta t}}\right]
\end{aligned} \tag{3.9}$$

where N is the number of time intervals and Δt is the size of the interval [10, 48].

3.3 CFD model verification

To verify the simulation model, I simulated three flow cases and compared the drag force obtained from the simulation with a known drag correlation and formulae. The first case is steady flow passing by the stationary sphere. For this simulation, the no-slip wall condition was set for boundary ② and ③, and the inlet velocity condition for boundary ⑤. The drag coefficient (C_d) was calculated from the simulation result as the following:

$$C_d = \frac{F_d}{\frac{1}{2}\rho U_c^2 \cdot \pi R^2}, \tag{3.10}$$

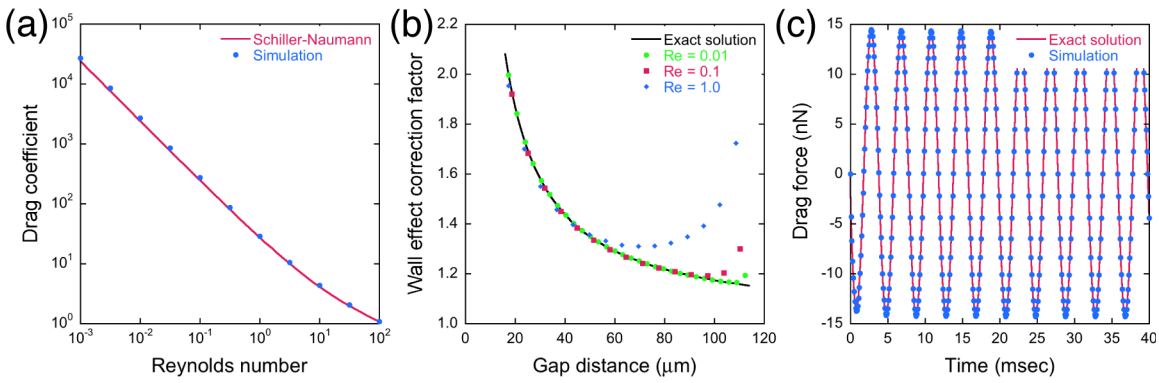

Figure 3-3: Verification of the CFD model: (a) The steady drag coefficient of a sphere. (b) The wall effect correction factor for the drag force on a sphere steadily moving toward a rigid plane. (c) The unsteady drag force on an oscillating sphere.

and the values are were compared to the Schiller-Nauman formula, a standard drag correlation given as [21]

$$C_d = \frac{24}{\mathrm{Re}}\Big(1 + 0.15\mathrm{Re}^{0.687}\Big). \tag{3.11}$$

This formula is valid for $\mathrm{Re} < 800$. As Figure 3-3(a) shows, the simulation results are in a good agreement with the formula.

For the second case, the sphere of the model was set to move toward boundary ⑤ at constant velocity with the assigned boundary conditions unchanged. In this case, the analytic solution of the drag force is given as Eq. 3.5, and it is valid when $L_s > R$ and $\mathrm{Re} \ll 1$. The wall effect correction factor was calculated by dividing the drag force obtained from the simulation with the corresponding Stokes drag force. Figure 3-3(b) shows that simulation results agree well with the exact solution for $\mathrm{Re} < 1$. Because the sphere starts moving suddenly in the simulations, the obtained correction factor shows deviations from that of the exact solution at the beginning of the sphere's motion and convergence to that of the exact solution as the flow develops.

In the last case, the sphere part was set to oscillate in the z-direction according to velocity given as

$$U_c = \mathrm{Re}\frac{\mu}{2\rho R}\sin\Big(2\pi\frac{t}{0.004}\Big). \tag{3.12}$$

Because $\tau_{\max} \approx 1$ msec in Figure 3-2(b), the oscillation period was chosen to be 4

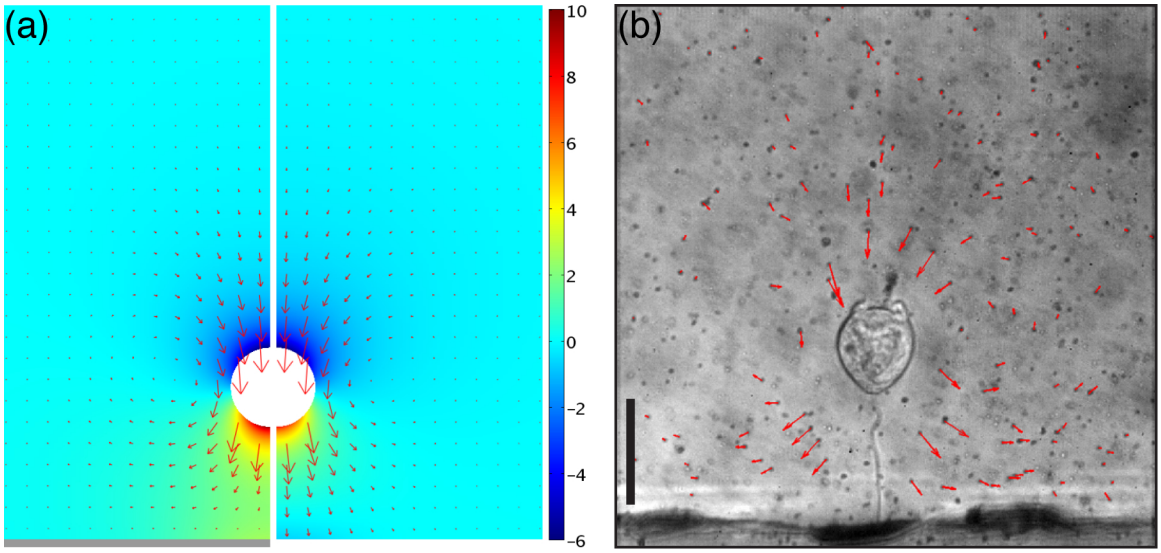

Figure 3-4: A flow field comparison between the CFD simulation and the flow visualization at $t = 0.74$ msec, around $\tau_{\max}$: (a) Flow velocity vectors with pressure distribution obtained from the CFD simulations. The unit of the color bar is Pa, and the scale of velocity vectors is arbitrary. The left and right half of the figure show flow field simulated with and without the substrate, respectively. A thick gray line is added at the bottom in the left figure to represent the substrate. The radius of the contracted zooid is 19.1 μm, and the maximum Reynolds number is 2.3. The coefficients of Eq. 3.6 are $L_{s,\max} = 80.1$ μm, $L_{s,\min} = 14.6$ μm, $c_1 = 7.174 \times 10^{-4}$ sec, $c_2 = 1.257$, and $c_3 = 1.086$. (b) Experimentally visualized flow field. The scale of velocity vectors is arbitrary, and the size of the scale bar is 50 μm.

msec. In the case of $\mathrm{Re} \ll 1$, the drag force on the oscillating sphere can be calculated with Eq. 1.4. The simulation results show a good agreement with the unsteady Stokes drag formula up to $\mathrm{Re} = 1$. Figure 3-3(c) shows the result of $\mathrm{Re} = 1.0$.

3.4 Results

3.4.1 Comparison with visualized flow

The CFD simulation clearly illustrates the wall effect from the substrate. Fig. 3-4(a) compares simulation results with and without the substrate in terms of flow velocity and pressure distribution at $t = 0.74$ msec. For the simulation without the substrate, boundary ⑤ of the simulation model was modified to the open boundary condition.

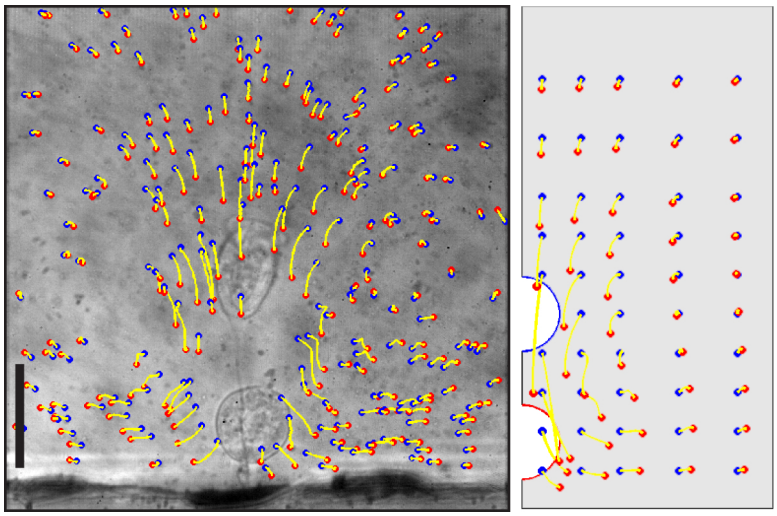

Figure 3-5: A particle path comparison between the CFD simulation and the flow visualization: The left micrograph shows experimentally obtained particle paths, and the right figure shows particle paths calculated from the CFD simulation result with the 4^{th} order Runge-Kutta method. Yellow lines are particle paths, and blue and red dots indicate where particles start and stop, respectively. Images before and after contraction are overlapped. The size of the scale bar is 50 μm.

The simulation result with the substrate (the left half of the figure) agrees well with the flow visualization result. Blocked by the substrate, water flows laterally outward near the bottom. In contrast, the simulation result without the substrate (the right half of the figure) shows that the flow pattern below the zooid is different. The pressure distribution is also different. Compared with the right graph, the left graph shows that higher pressure builds up below the zooid because of the substrate. This higher pressure means that the zooid in the left graph experiences greater upward force, which is the drag force. The drag force on the zooid is calculated to be 34.4 nN with the substrate and 31.8 nN without the substrate. The wall effect of the substrate is responsible for this drag force difference. Figure 3-5 compares particle paths obtained from the flow visualization experiment and from the CFD simulation, and both results agree well to each other.

3.4.2 Contraction force estimation

Figure 3-6 shows time courses of the contraction force developed by *Vorticella* in four different viscous media estimated with four different methods: Stokes' law (F_s, Eq. 1.3), the Stokes drag formula with the wall effect correction factor (F_{sw}, Eq. 3.5), the unsteady Stokes drag formula (F_{us}, Eq. 1.4) and the CFD simulation (F_{cfd}). Maximum values of the estimated contraction force and the time when the contraction force reaches the maximum are summarized in Table 3.3.

Figure 3-6(a) shows force estimation results for water. The difference between F_s and F_{sw} illustrates how significant the wall effect is. The maximum of F_{sw} is about 22% greater than that of F_s. The effect of the transient inertia force is responsible for the difference between F_s and F_{us}. F_{us} is greater than F_s by about 35% in the maximum. Because the added mass force is negligibly small, this difference is mainly due to the history force. Another observed difference between F_s and F_{us} is the time to the peak force. Considering that F_s reaches its maximum at $\tau_{\max}$, this difference implies that the contraction force reaches its maximum before the contraction speed does. Our CFD simulation also resulted in the time to the maximum force similar to that of F_{us}, but its maximum force is greater than that of F_{us}. This is because the CFD simulation takes account of the effects of the unsteadiness, the substrate and the finite Reynolds number simultaneously. In water, the maximum of F_{cfd} is approximately 55% greater than that of F_s. Therefore, using Stokes' law underestimates the contraction force of *Vorticella*.

It is noticeable in Figure 3-6(a) that F_{us} becomes negative in the later stage of contraction. This means that the zooid experiences the drag force in the direction

Table 3.3: The peak contraction force and the time to the peak contraction force.

PVP wt %	F_s (nN)/(msec)	F_{sw} (nN)/(msec)	F_{us} (nN)/(msec)	F_{cfd} (nN)/(msec)
0%	17.9/0.96	21.9/1.01	24.2/0.76	27.7/0.79
1%	29.9/0.90	35.9/0.95	35.3/0.71	38.8/0.75
2%	51.3/1.03	61.4/1.10	55.4/0.85	62.2/0.98
3%	56.4/1.04	67.1/1.11	59.4/0.85	67.5/1.02

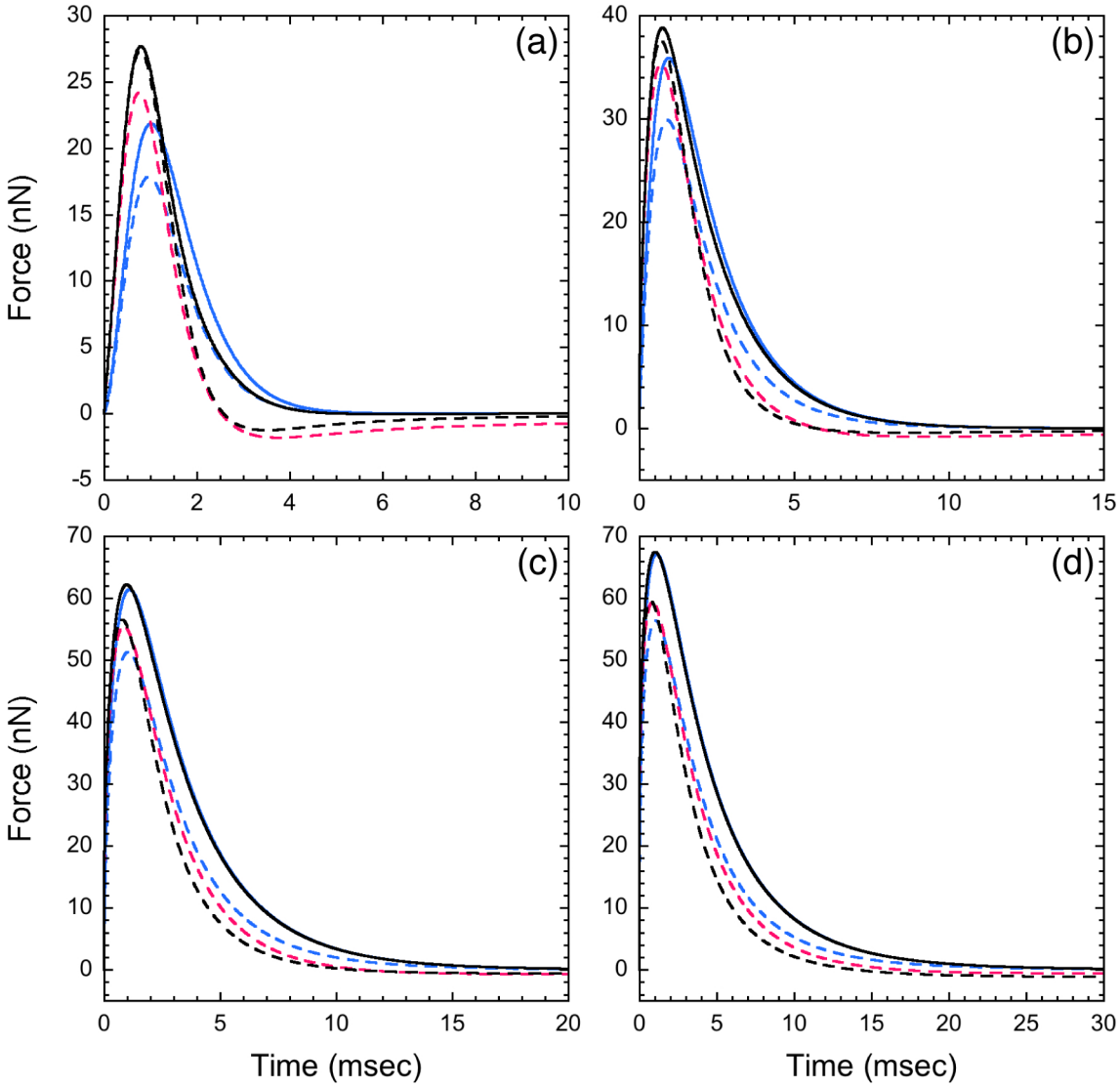

Figure 3-6: Contraction force estimation results for (a) 0%, (b) 1%, (c) 2% and (d) 3% PVP solution. The viscosity of the PVP solutions: 0% - 1 cP, 1% - 2.7 cP, 2% - 6.9 cP and 3% - 10.3 cP. F_s - blue dashed line, F_{sw} - blue solid line, F_{us} - red dashed line, F_{cfd} - black solid line and $F_{cfd,nw}$ - black dashed line.

of contraction, i.e., toward the substrate. The memory effect of the fluid accounts for this negative drag. Although the zooid almost stops its motion, the induced flow cannot stop immediately because of its inertia, so the flow exerts force on the zooid. However, F_{cfd}, the most rigorous estimate, does not show such negative force. The difference is due to the substrate. Figure 3-6(a) also shows a CFD-based contraction force estimate with the substrate omitted ($F_{cfd,nw}$), which means that the wall effect is ignored. Although $F_{cfd,nw}$ agrees with F_{cfd} in the early stage of contraction, it also turns negative in the later stage. Therefore, the substrate prevents the negative drag force by blocking the following flow due to the memory effect.

Because $F_{cfd,nw}$ assumes that the contraction-induced flow is not confined by the substrate, its flow condition is same as that of F_{us} except the difference in the Reynolds number. Hence, the difference of F_{us} and $F_{cfd,nw}$ shows how significant the effect of the convective inertia force is. The maximum of $F_{cfd,nw}$ (27.3 nN) is about 13% greater than that of F_{us}. On the other hand, the agreement between F_{cfd} and $F_{cfd,nw}$ in the early stage means that the wall effect is negligible in this phase. Therefore, in the case of contraction in water, the effect of the unsteadiness and the finite Reynolds number is significant in the early stage of contraction because of acceleration and high speed whereas the wall effect is dominant in the later stage because of proximity to the substrate.

As the medium viscosity increases, the maximum contraction speed ($|U_c|_{\max}$) decreases, and the contraction time (τ_c) increases whereas the time to the maximum contraction speed ($\tau_{\max}$) is almost constant (Table 3.1). Although with the decreasing contraction speed, the contraction force increases due to the increasing medium viscosity. The decreasing difference of F_s and F_{us} with the increasing medium viscosity means that the transient inertia effect becomes negligible in more viscous liquids as the decreasing Stokes number predicts. The decreasing difference of F_{us} and $F_{cfd,nw}$ shows the decreasing effect of the convective inertia force as the decreasing Reynolds number predicts. The increasing kinematic viscosity of the medium ($\nu = \mu/\rho$) implies that the viscous characteristic time scale (R^2/ν) decreases and that any change in flow field diffuses away in a shorter time. Hence, the memory effect of the fluid

becomes more negligible. This trend is evident in Figure 3-6 in which F_{us} shows the negligible negative force in 1%, 2% and 3% PVP solutions. Furthermore, because the maximum Reynolds number of the 3% PVP case is much smaller than unity, the induced flow can be regarded as a creeping flow. The perfect agreement between F_{cfd} and F_{sw} supports this (Figure 3-6(d)).

3.4.3 Contraction energetics

Because the contraction distance of *Vorticella* ($L_{s,\max} - L_{s,\min}$) is almost constant regardless of the medium viscosity in this study, the greater contraction force in more viscous media means that the cell has done more work to contract (Table 3.4 and Figure 3-7).

Table 3.4: The total work, maximum power output and efficiency of the spasmoneme.[6]

PVP	W_{tot} (pJ)				ϵ	$P_{\max}$ (nW)			
wt %	Eq. 1.3	Eq. 3.5	Eq. 1.4	CFD	(%)	Eq. 1.3	Eq. 3.5	Eq. 1.4	CFD
0%	1.14	1.46	1.31	1.64	8.0	1.03	1.26	1.35	1.56
1%	1.74	2.17	1.85	2.25	11.0	1.05	1.26	1.23	1.36
2%	2.94	3.69	2.99	3.72	18.2	1.23	1.47	1.32	1.49
3%	3.02	3.77	3.02	3.79	18.5	1.00	1.19	1.05	1.19

The energy source for *Vorticella*'s contraction is not ATP but calcium ions. Therefore, the increasing total work (W_{tot}) implies that, under higher loading conditions, the spasmoneme better converts energy obtained from the calcium binding to mechanical work. Amos estimated the maximum energy available from the calcium binding ($\Delta\mu_{Ca}$) with

$$\Delta\mu_{Ca} = \mathbf{R}\mathbf{T}\ln\frac{[\mathrm{Ca}^{2+}]_{\text{high}}}{[\mathrm{Ca}^{2+}]_{\text{low}}} \tag{3.13}$$

where $\mathbf{R}$ is the universal gas constant (8.314 J/K·mol), $\mathbf{T}$ is the temperature (293 K), and $[\mathrm{Ca}^{2+}]_{\text{high}}$ and $[\mathrm{Ca}^{2+}]_{\text{low}}$ are calcium ion concentrations for the extended/contracted stalk ($[\mathrm{Ca}^{2+}]_{\text{high}} = 10^{-6}$ M and $[\mathrm{Ca}^{2+}]_{\text{low}} = 10^{-8}$ M), respectively [2]. Then, the maxi-

[6]The CFD-based estimate of the total work for water is approximately twice Amos' estimate, 0.9 pJ [2]. The maximum specific power, the power output divided with the wet mass of the spasmoneme, is $5.80 \sim 7.61$ W/g whereas that of Amos based on Stokes' law is 2.67 W/g.

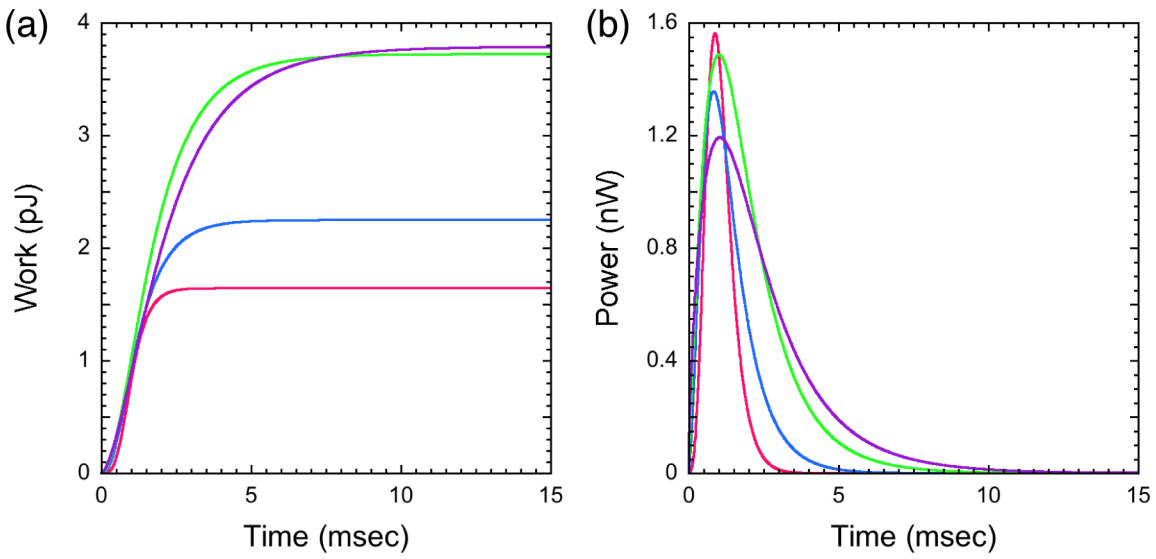

Figure 3-7: Energetics of the *Vorticella* contraction: (a) Mechanical work done, (b) Power dissipated by the spasmoneme to overcome viscous resistance in four PVP solutions. The PVP concentration of the medium: red - 0% (1 cP), blue - 1% (2.7 cP), green - 2% (6.9 cP) and magenta - 3% (10.3 cP).

mum available energy is calculated to be approximately 11.2 kJ per 1 mole of calcium ion, and *Vorticella* converts this energy to mechanical work with a certain efficiency. Moriyama et al. calculated the total amount of energy available from the calcium binding (Q) and the efficiency of the spasmoneme (ϵ) as the following:

$$Q = N_{Ca} L_{s,\max} \Delta\mu_{Ca} \tag{3.14}$$

$$\epsilon = \frac{W_{\text{tot}}}{Q} \tag{3.15}$$

where N_{Ca} is the amount of calcium ions bound to 1 μm of the spasmoneme [69]. Using *Zoothamnium geniculatum*, Routledge et al. measured that 1.7 g of calcium binds to 1 kg of dry mass of the spasmoneme and that the dry mass concentration of the spasmoneme is 21 g/100 ml [78]. Moriyama et al. converted these values to 6.6×10^{-18} mole/μm with Amos' spasmoneme radius (0.5 μm) as the following:

$$N_{Ca} = \frac{\pi}{4} d_s^2 \cdot C_s \cdot m_{Ca} \cdot \frac{1}{A_{Ca}} \tag{3.16}$$

where d_s is the diameter of the spasmoneme, C_s is the dry mass concentration of the spasmoneme (21 g/100 ml), m_{Ca} is the amount of calcium bound to 1 kg of dry mass of the spasmoneme (1.7 g), and A_{Ca} is the atomic weight of calcium (40.1 g/mole) [69]. In the current case, because the diameter of the spasmoneme is about 1.5 μm [27] and the stalk length is about 116 μm, N_{Ca} is calculated to be 1.57×10^{-17} mole/μm, and the total energy is approximately 20.4 pJ. The efficiency of the spasmoneme is summarized in Table 3.4. Moriyama et al. evaluated that the efficiency of the extracted stalk is 7% [69], which is comparable to the efficiency found in the current study. Considering that the evaluated total work does not include work done to overcome the internal resistance of the spasmoneme and the elastic resistance of the sheath, the efficiency is expected to be higher than the current estimation.

In contrast to the increasing total work, the maximum power output of the *Vorticella* spasmoneme appears to be rather constant compared to the significantly varying medium viscosity (Table 3.4). Upadhyaya et al. suggested with the Stokes drag formula that the stalk contraction of *Vorticella* is power-limited [104], and the CFD-based power estimate also shows power-limitedness. It seems that, under viscous loading, power-limited *Vorticella* adjusts its contraction behavior by decreasing the contraction rate and by increasing the efficiency of the spasmoneme. The motility of bacteria is also power-limited [85]. Having constant power input to the flagellum, bacteria alter the conformation and efficiency of the flagellum according to the medium viscosity. This power-limitedness suggests that *Vorticella* generate and consume energy for contraction in the same fashion even in different loading conditions because the instantaneous work is very similar in terms of amount and gradient for all cases in the early stage of contraction although the total work is greater in more viscous environment (Figure 3-7).

3.5 Discussion

The CFD-based estimation of the contraction force proves that a rigorous force estimation requires consideration of the transient/convective inertia force of the contraction-

induced flow and the wall effect of the substrate. In the case of water, any of the used drag formulae cannot evaluate the contraction force accurately. As the medium viscosity increases, the contribution of the transient/convective inertia force decreases as the decreasing Reynolds number and Stokes number imply. However, the wall effect still remains even in highly viscous media, so the estimate based on Eq. 3.5 agrees well with the CFD-based one for the 3% PVP solution.

However, because this study deals with only one *Vorticella*'s contractions in different viscous media, work and power output should be calculated over a significant number of *Vorticella* cells with CFD simulations or an appropriate fluid dynamic model to confirm power-limitedness. Furthermore, the CFD-based force estimation can be used to confirm the scaling law that Upadhyaya et al. proposed ($F_{d,\max} \sim \mu^{0.5}$) based on Stokes' law and power-limitedness [104].

On the other hand, *Vorticella*'s contraction may be power-limited only under passive loading conditions. The stagnant medium surrounding *Vorticella* can exert resistance force only when the cell contracts, so the medium cannot maintain significant resistance in the early and later stage of contraction. In other words, viscous resistance force is coupled with the moving speed of the zooid. France's micropipette experiment is similar in that the stall force is coupled with the contraction distance of *Vorticella*, but the bent micropipette exerts force even after contraction is completed [27]. In contrast, applying centrifugal force is an active loading condition because the cell is always under the influence of the force [27]. The passive loading condition may be a reason for almost constant $\tau_{\max}$ in different viscous media. When *Vorticella* is laid in a viscous fluid flow, $\tau_{\max}$ varies according to the magnitude of stalling force as will be shown in Section 6.3.2. This suggests that the dynamics of *Vorticella* contraction may depend on the type and condition of external loadings. Therefore, the power-limitedness must be confirmed for contraction in active loading conditions.

Chapter 4

Contraction Force Estimation Model

4.1 A new approach

In the previous chapter, the CFD technique was used to estimate the contractile force of the spasmoneme and to analyze the energetics of its contraction. Instead of using the demanding numerical simulation, it is worthwhile to propose a fluid dynamic model considering all the effects from the transient inertia force, the small but finite Reynolds number and the substrate. When it comes to such a model, one may refer to Yang's model that was developed to predict the trajectory of a sphere pendulum approaching a rigid plane [114]. In this study, I propose a new fluid dynamic model to estimate the contraction force of *Vorticella* based on Yang's model.

In the model, the zooid of contracting *Vorticella* is assumed to be a solid sphere transiently moving perpendicularly toward a rigid plane in an ambient stagnant fluid, which is same as the CFD simulation (Figure 3-1(a)). As mentioned earlier, because of the negligible inertia of the cell body, the contraction force of *Vorticella* can be equated to the drag force on the body as the following:

$$F_c \approx F_d = F_{QS} + F_{AM} + F_{HS}. \tag{4.1}$$

The effect of the unsteadiness is embodied in the model by dividing the drag force into three components as Eq. 1.4 is: the quasi-steady drag force (F_{QS}), added mass force (F_{AM}) and history force (F_{HS}). The simultaneous effect of the finite Reynolds number and the substrate is incorporated in the model as a correction factor of each term that are functions of the Reynolds number and a ratio of the gap distance to the sphere radius.

4.2 A new model for contraction force estimation

4.2.1 Quasi-steady drag force

The quasi-steady drag force is the drag force that the sphere experiences when it is assumed to steadily move at the instantaneous velocity. Regarding the analytic correction factor for the quasi-steady drag force, Cox and Brenner suggested an analytic solution of the correction factor [22]. However, their correction factor is not applicable to the contraction of *Vorticella* because it is valid for an infinitesimal gap between the sphere and the rigid boundary. On the other hand, Joseph used the product of a Reynolds number effect correction factor obtained from a standard drag correlation and Brenner's wall effect correction factor [42]. Yang also employed this approach, but their correction factor is unproven [114].

To my best knowledge, there has been no experimental measurement of the wall correction factor at the finite Reynolds number. In most relevant studies about particles sedimenting or rebounding in a liquid, the driving force is gravity, so the particle Reynolds number is less than unity near the surface. This means that Eq. 3.5 is enough to calculate the drag force. Only Zhang et al. suggested an empirical correlation of the wall effect correction factor based on their particle collision experiment as the following:

$$\lambda\left(\mathrm{Re}, \frac{\rho_p}{\rho}, \frac{R}{H}\right) = \exp\left(\left(\frac{\mathrm{Re}}{1.7}\right)^{0.44}\left(\frac{\rho_p}{\rho}\right)^{0.19}\left(\frac{R}{H}\right)^{\mathrm{Re}^{0.47}}\right) \tag{4.2}$$

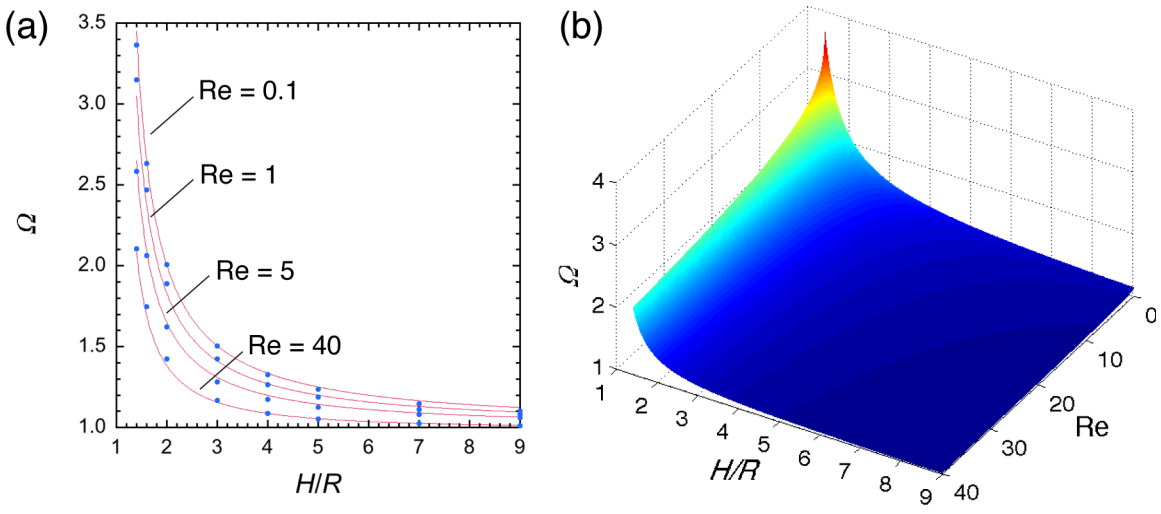

Figure 4-1: The wall effect correction factor correlation: (a) Eq. 4.4 (red lines) is compared to the result of Wu and Lee (blue dots) shown in Table 4.1 [113]. (b) The wall effect correction factor increases as the sphere approaches the wall closer or as the Reynolds number decreases.

where ρ_p is the density of a solid particle [116]. This correlation is valid for $5 \leqq \mathrm{Re} \leqq 300$, $1.2 \leqq \rho_p/\rho \leqq 8$ and 1 mm $\leqq R \leqq$ 6.35 mm, so this correlation is not applicable to contracting *Vorticella*. On the other hand, Wu and Lee tabulated values of the correction factor based on their CFD simulations (Table 4-1) [113].

Table 4.1: The wall effect correction factor as a function of Re and H/R [113].[7]

$\frac{H}{R}$	Re = 0.0	0.1	1	5	10	20	30	40
1.4	3.736	3.364	3.148	2.585	2.367	2.203	2.113	2.103
1.6	2.849	2.633	2.468	2.062	1.924	1.823	1.756	1.748
2.0	2.126	2.008	1.888	1.621	1.547	1.486	1.434	1.424
3.0	1.569	1.504	1.424	1.281	1.252	1.215	1.174	1.166
4.0	1.380	1.327	1.265	1.174	1.158	1.130	1.093	1.087
5.0	1.285	1.238	1.188	1.125	1.115	1.092	1.058	1.054
7.0	1.190	1.147	1.113	1.080	1.077	1.058	1.027	1.024
9.0	1.142	1.102	1.080	1.061	1.061	1.044	1.015	1.011

In this study, I express the quasi-steady drag force in terms of the drag coefficient

[7] Values of λ at Re = 0.0 were calculated with Eq. 3.5.

(C_d) and the wall effect correction factor (Ω) as the following:

$$\begin{aligned} F_{QS} &= \pi R^2 \cdot \frac{1}{2}\rho U_c^2 \cdot C_d \cdot \Omega \\ C_d &= \frac{24}{\mathrm{Re}}\Big(1 + 0.15\mathrm{Re}^{0.687}\Big). \end{aligned} \tag{4.3}$$

Regarding the wall effect correction factor, I propose the following correlation obtained from Table 4.1:

$$\Omega = \frac{\lambda}{(1+\sqrt{\mathrm{Re}})^{0.39(H/R)^{-0.85}}}. \tag{4.4}$$

where λ is the wall effect correction factor of Eq. 3.5. The suggested correlation agrees well with the values of Table 4.1 (Figure 4-1), and it is valid for $0 \leqq \mathrm{Re} \leqq 40$ and $1.4 \leqq H/R \leqq 9$.

4.2.2 Added mass force

The added mass force is an additional force that the sphere experiences while accelerating fluid in front of it and eventually increasing the kinetic energy of the surrounding fluid. In contrast to the quasi-steady force, the added mass force does not depend on the Reynolds number [48, 109]. One can easily conjecture this because the form of the added mass force for the creeping flow is same as that for the potential flow of which the Reynolds number is infinite. Therefore, only the wall effect of the substrate needs to be considered in the present study, and it can be easily incorporated based on the potential flow theory. In the potential flow theory, flow caused by the sphere perpendicularly moving toward the plane can be represented with flow caused by two identical spheres moving toward each other. In such a case, the added mass is given as [65]

$$F_{AM} = -\frac{4}{3}\pi\rho R^3\left[\frac{1}{2}\Big(1+\frac{3R^3}{8H^3}\Big)\frac{dU_c}{dt} + \frac{1}{4}\frac{9R^3}{8H^4}U_c^2\right]. \tag{4.5}$$

4.2.3 History force

The history force is related with the memory effect of a fluid. For example, let's imagine that you move your hand in water. When you stop your hand, you can

still feel water flow in the direction of your hand motion. This following water flow shows that there is a time lag for momentum to be transferred from the hand to water through a boundary layer around the hand. Therefore, the history force is also related to the growth of a boundary layer on an object. In the creeping flow regime, the analytic solution of the history force is known called the Basset-Bousinessque force (the last term in Eq. 1.4). The history force depends not only on the Reynolds number but also on motion patter of an object such as sudden start/stop and oscillation. Kim et al. proposed a form of the convective inertia effect corrected history force based on various numerical simulation results [48]. Recently, Yang added the wall effect correction factor to Kim et al.'s model as the following:

$$
\begin{aligned}
F_{HS} &= -6\pi\mu R K_H^{\frac{3}{2}} \int_0^t \frac{dU_c}{dt}\Big|_{t=s} \frac{ds}{K(t-s)} \\
K_H &= 1 + \frac{0.375 - \dfrac{0.03125}{(1-2H^{*2})^3}}{H^{*3}} - \frac{3}{(1-4H^{*2})^3} - \frac{0.015625}{(H^*-2h^{*3})^3} \\
&\quad + \frac{3}{(1-12H^{*2}+16H^{*4})^3} + \frac{0.375}{(3H^*-16H^{*3}+16H^{*5})^3} \\
H^* &= \frac{H}{R} \\
K(t-s) &= \left\{ \Big[\frac{\pi(t-s)\nu}{R^2}\Big]^{0.2} + G(s)\Big[\frac{\pi}{2}\frac{|U_c|^3_{t=s}(t-s)^2}{R\nu f_H^3}\Big]^{0.2} \right\}^{2.5} \\
G(t) &= \frac{1}{1+\beta(t)\sqrt{M_1(t)}} \\
\beta(t) &= \frac{22.0}{1+\dfrac{\phi_r(t)^{1.25}}{0.07[\phi_r(t)+\phi_r(t)^{0.25}]}} \\
\phi_r(t) &= \frac{M_2(t)}{M_1(t)} \\
M_1(t) &= \frac{2R}{U_c^2}\left|\frac{dU_c}{dt}\right| \\
M_2(t) &= \frac{(2R)^2}{|U_c|^3}\left|\frac{d^2U_c}{dt^2}\right| \\
f_H &= 0.75 + 0.126\mathrm{Re}
\end{aligned}
\tag{4.6}
$$

where K_H accounts for the wall effect, and the kernel inside the integration term, $K(t-\tau)$, accounts for the effect of the finite Reynolds number [114].

4.3 Methods

The stalk length and contraction rate data of *Vorticella* used for the CFD simulation were used for the newly proposed model. The quasi-steady drag force and the added mass force were directly calculated with Eq. 3.6 and 3.7 with a time step of 0.01 msec. The history force was calculated with the numerical integration recipe used in Section 3.2, and, in this case, the recipe is modified to be

$$\begin{aligned}
&\int_0^t \frac{\dot{U}_c}{K(t-s)}ds = \int_0^{N\Delta t} \frac{\dot{U}_c}{K(t-s)}ds \\
&= \frac{\Delta t}{6}\sum_{i=1}^{N-1}\left[\frac{\dot{U}_{c_{i-1}}}{K\big(N\Delta t-(i-1)\Delta t\big)} + \frac{2(\dot{U}_{c_{i-1}}+\dot{U}_{c_i})}{K\big(N\Delta t-(i-0.5)\Delta t\big)} + \frac{\dot{U}_{c_i}}{K\big(N\Delta t-i\Delta t\big)}\right] \\
&+ \frac{0.9\Delta t}{6}\left[\frac{\dot{U}_{c_{N-1}}}{K\big(N\Delta t-(N-1)\Delta t\big)} + \frac{2(\dot{U}_{c_{N-1}}+\dot{U}_{c_{N-0.1}})}{K\big(N\Delta t-(N-0.55)\Delta t\big)} + \frac{\dot{U}_{c_{N-0.1}}}{K\big(N\Delta t-(N-0.1)\Delta t\big)}\right] \\
&+ \frac{0.1\Delta t}{2}\left[\frac{8\sqrt{2}}{3}\frac{\dot{U}_{c_N}}{K\big(N\Delta t-(N-0.05)\Delta t\big)} - \frac{4}{3}\frac{\dot{U}_{c_N}}{K\big(N\Delta t-(N-0.1)\Delta t\big)}\right]
\end{aligned} \tag{4.7}$$

where Δt is 5×10^{-4} msec [10, 48]. For calculation, MATLAB was used.

4.4 Results

Figure 4-2 compares force estimates of the new model to other estimates shown in Section 3.4.2. In Figure 4-2(a), the quasi-steady drag force estimated with the new model is greater than that based on Brenner's solution (Eq. 3.5) around $\tau_{\max}$. This difference is due to the convective inertia force that becomes dominant as the Reynolds number becomes greater than unity for this moment. The new model shows a good agreement with Brenner's solution otherwise.

Figure 4-2(b) compares the added mass force estimate of the new model and that

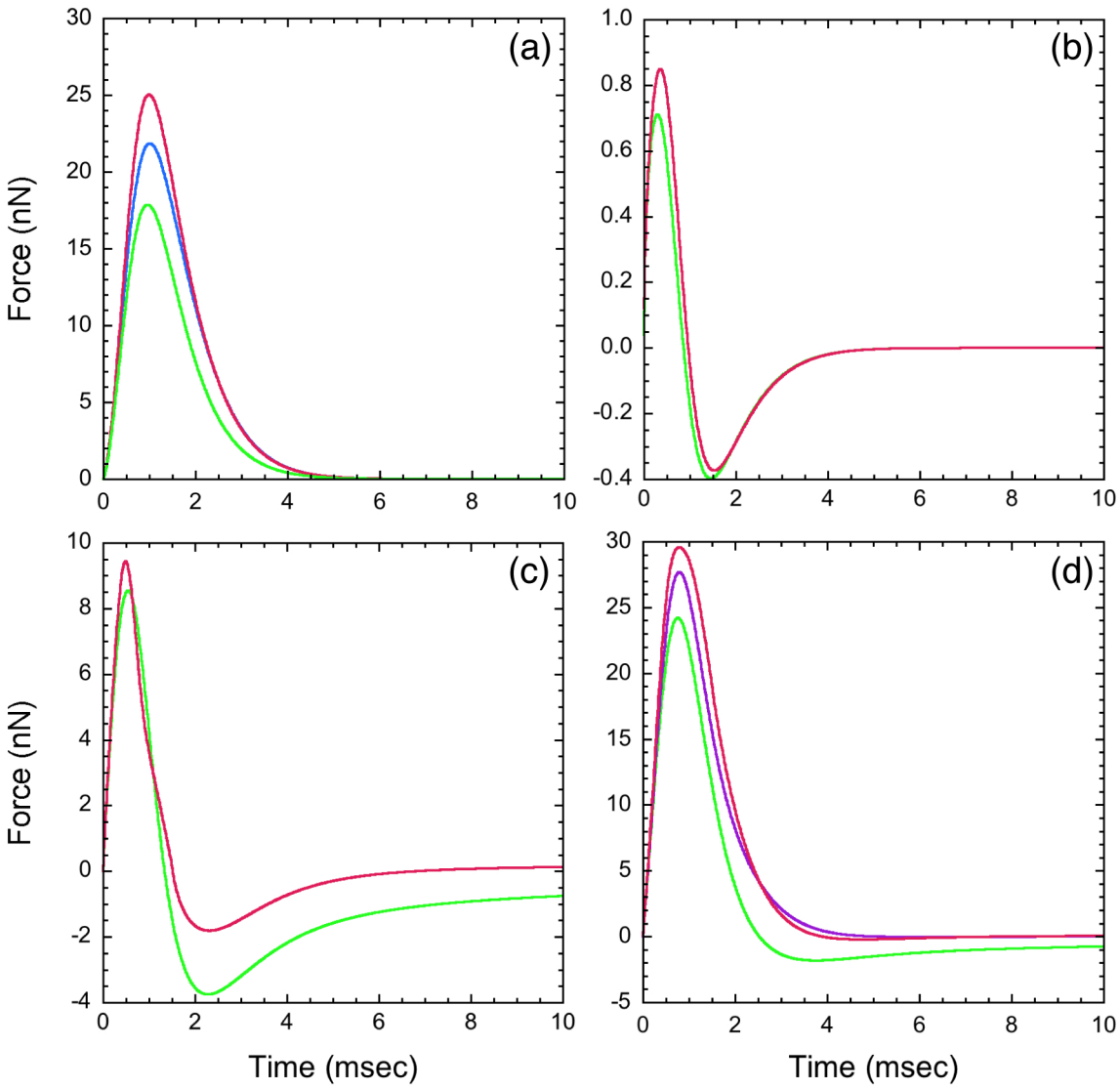

Figure 4-2: Force estimation results of the new model applied for contraction in water: (a) The quasi-steady drag force. (b) The added mass force. (c) The history force. (d) The total drag force. Red line - the new model, green line - the unsteady Stokes drag formula (Eq. 1.4), blue line - Brenner's solution (Eq. 3.5) and magenta line - the CFD simulation.

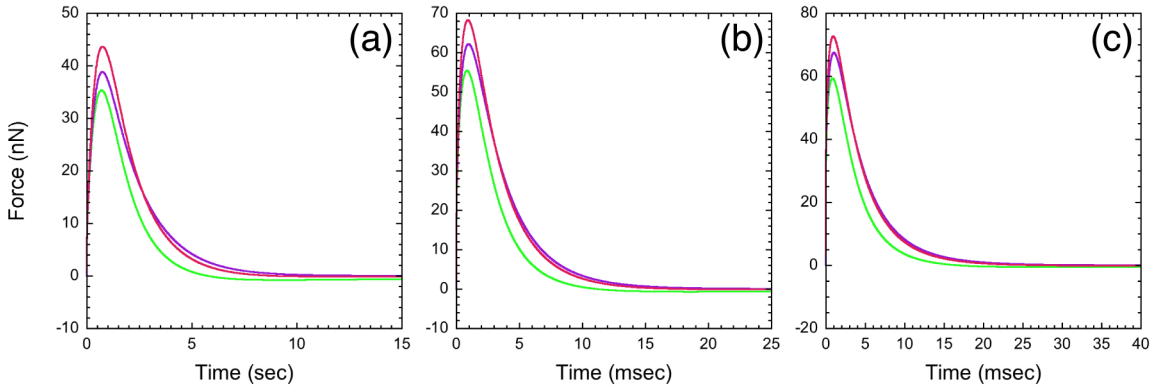

Figure 4-3: Contraction force estimates made with the new model for (a) 1%, (b) 2% and (c) 3% PVP solution. Red line - the new model, green line - the unsteady Stokes drag formula and magenta line - the CFD simulation.

of the unsteady Stokes drag formula (Eq. 1.4). Although the new model estimates the added mass force a little greater than the unsteady Stokes formula does, the force component is negligible compared to the total drag force.

The wall effect from the substrate is drastic in the history force estimation in Figure 4-2(c). Although the new model shows a little difference from the unsteady Stokes drag formula in terms of the history force in the early stage of contraction ($t < 1$ msec), the new model results in less negative history force than the unsteady Stokes drag formula does in the later stage. In Section 3.4.2, the suppression of the negative drag force by the substrate is discussed based on the CFD simulation.

The contraction force estimated with the new model is compared to the CFD-based estimate in Figure 4-2(d). Although the model's estimate is a little greater than the CFD-based estimate, they show a reasonable agreement to each other. Especially, it is noticeable that the new model results in negligible negative force in the later stage of contraction unlike the unsteady Stokes drag formula as predicted in Figure 4-2(c). On the other hand, the difference in the maximum contraction force is mainly due to the difference in the peak quasi-steady drag force.

Figure 4-3 shows contraction force estimates made with the new model for contractions in 1%, 2% and 3% PVP solutions, and Table 4.2 compares the new model and the CFD simulation in terms of the peak contraction force and the time to the

peak contraction force. Although the new model results in the contraction force estimates similar to the CFD-based estimates, its maximum value is greater than that of the CFD simulation result. Examinations of each force term revealed that the difference in the maximum quasi-steady drag force between the new model and Brenner's solution decreases as the maximum Reynolds number decreases and that the difference in the maximum history force between the new model and the unsteady Stoke drag formula does not change much. Therefore, differences of the new model and the CFD-based estimate in the medium of higher PVP concentration seem due to the differences in the history force estimate.

Table 4.2: The peak contraction force and the time to the peak contraction force estimated with the new model.

PVP wt%	New model (nN) / (msec)	CFD simulation (nN) / (msec)
0%	29.6 / 0.79	27.7 / 0.79
1%	43.6 / 0.75	38.8 / 0.75
2%	68.2 / 0.92	62.2 / 0.98
3%	72.7 / 0.94	67.5 / 1.02

4.5 Discussion

Compared to the CFD-based contraction force estimate, the new model proposed here seems to estimate *Vorticella*'s contractile force reasonably accurately. However, the model still has a room for further improvement. First of all, the quasi-steady force term of the current model employs the wall effect correction factor obtained from the CFD simulation of Wu and Lee [113]. Because their simulation model was not verified properly, this correction factor must be proven with experimental measurements: the drag force on a solid ball can be directly measured while the ball moves toward a rigid plane at a constant velocity that makes the Reynolds number greater than unity. Second of all, the history force term of the model needs a fine tuning because the kernel used in the model is a semi-empirical model that was optimized for an oscillating sphere over a certain range of the Reynolds number. Furthermore,

the wall effect correction factor of the history force was not well verified theoretically or experimentally. This correction factor must be a function of dimensionless gap distance and the Reynolds number as the wall correction factor of the quasi-steady drag force term is. Finally, the model must be verified with properly designed experiments [43, 53]: the aforementioned wall effect correction factor measurement setup can be used with an unsteady velocity profile. In such an experiment, the solid ball is a scaled-up model of the *Vorticella* zooid, and its motion profile should be determined based on the contraction speed of *Vorticella* and fluid dynamic similarity.

Chapter 5

Isometric Force Measurement

5.1 Introduction

Whereas the previous chapters are about estimating the contraction force developed by *Vorticella* contracting in a stagnant viscous medium, it will be examined from this chapter on how *Vorticella* behaves in viscous fluid flow. Especially, this chapter deals with how to measure the isometric force of the *Vorticella* stalk by applying the viscous drag force. The isometric force refers to the maximum contraction force that the *Vorticella* stalk can generate while it cannot contract at all.[8] Therefore, this maximum contraction force is different from the peak contraction force reached in motionless viscous media, and it is the upper bound of the contraction force of the *Vorticella* stalk.

As introduced in Section 1.4.1, there have been efforts to stall the contraction of *Vorticella* to measure the isometric force. Upadhyaya et al. attempted to increase the drag force on contracting *Vorticella* by placing the cell in highly viscous but stagnant media [104]. In a stagnant fluid, however, *Vorticella* does not experience any resistance unless it contracts, and the cell experiences little resistance at the beginning and ending of contraction because the magnitude of the drag force on the zooid is determined by the contraction rate of *Vorticella*. Furthermore, the *Vorticella* stalk

[8] Although the end-to-end length of the stalk does not decrease, the stalk's ability to contract is also regarded as the contraction force.

can contract maximally unless the medium viscosity is infinite. Therefore, placing the cell in motionless viscous media is a passive way to hinder its contraction, and it is impossible to completely stall contraction with this method.

In contrast, it is an active way to apply an external stall force to contracting *Vorticella* in the opposite direction to contraction because the cell always experiences resistance regardless of its motion. France used centrifugal force and the elastic restoring force of a micropipette as the stall force [27]. A problem of applying centrifugal force is that the magnitude of the force depends on the density difference between the cell and medium (it is easier to increase the viscosity of a medium than its density). In addition, the method requires a specialized microscope that has a limitation on using a high-speed camera [37]. Hence, France could not analyze the dynamics of *Vorticella* contracting under centrifugal force. On the other hand, using a micropipette enables more investigation into stalled contraction with a high-speed camera, but the method still has a limitation that it is difficult to control the bending stiffness of the pipette as desired and to stall a single cell with different pipettes. For these reasons, France averaged data from several cells for each pipette and obtained an ensemble-averaged value of the isometric force, not the value of each cell.

In this study, I apply viscous drag force on *Vorticella* using a microfluidic channel. Fixed at the stalk base, *Vorticella* lies down in the flow direction in the channel. Because the zooid is much larger than the stalk, most of the drag force that *Vorticella* experiences is applied to the zooid. As a result, the drag force retards the contraction of *Vorticella*. Compared to previous methods, this approach has an advantage that it is possible to control the magnitude of the stall force by adjusting the flow rate and the medium viscosity and to observe several contractions of a single cell per each flow condition with a high-speed camera. It was observed in this study that, under the applied viscous drag force, *Vorticella* contracts over a shorter distance generating greater contraction force. The measured isometric force of the *Vorticella* stalk is in the range of 150$\sim$350 nN. The isometric force of the *Vorticella* stalk appears linearly proportional to the stalk length, and this linear dependence suggests that 1 μm of the spasmoneme can generate the contraction force up to approximately 2.5 nN.

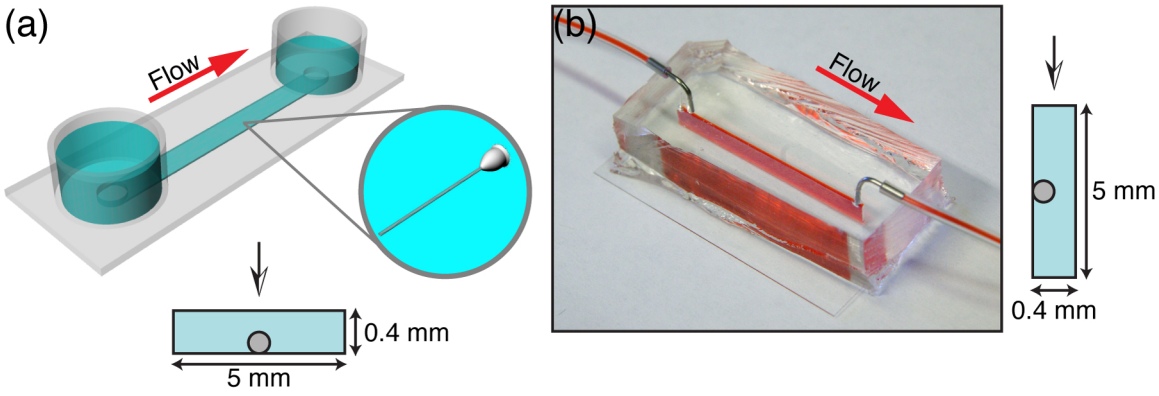

Figure 5-1: Microfluidic channels used to stall *Vorticella*'s contraction: (a) The plastic channel. The circular inset shows a magnified *Vorticella* cell in the channel. The cell lies down in the flow direction when flow is applied and contracts in the opposite direction to the flow. Therefore, experiencing the drag force, the cell is stalled. (b) The PDMS channel. The cross-section of each channel is shown with dimension. The gray circle and arrow represent the cell and the line of sight, respectively.

5.2 Methods

Microfluidic channels

Figure 5-1 shows two kinds of microfluidic channel used in this study: a plastic channel (μ-Slide I: hydrophobic/uncoated/sterile, ibidi, Germany, Figure 5-1(a)) for the stall experiment and a PDMS[9] channel (Figure 5-1(b)) for side-view observation. The dimension of the plastic channel is 400 μm in height, 5 mm in width and 50 mm in length. Because the thickness and optical properties of the bottom matches those of No. $1\frac{1}{2}$ cover glass, the plastic channel is appropriate for the bright field microscopy. The plastic channel has reservoirs at both ends for tube connection, and the length of the channel refers to the distance between centers of reservoirs.

For developing the contraction force estimation model shown in Section 5.4, it was required to observe contracting *Vorticella* from the side. However, the plastic channel does not accommodate side-viewing. Having a similar problem, Cao et al. developed a side-view flow channel system to observe cells of interest under viscous shear flow [18]. In this study, a simpler approach was tried. A 90° rotated channel was made

[9]Polydimethylsiloxane

with PDMS (SYLGARD 184 Silicone Elastomer Kit, Dow Corning, Midland, MI), i.e., the PDMS channel has the same cross-sectional dimension as the plastic channel, but it is rotated 90° with respect to the streamwise direction (see the channel cross-section in Figure 5-1). Therefore, the height and width of the PDMS channel is 5 mm and 400 μm, respectively. This PDMS channel and an extra-long-working-distance objective enabled acquiring images of *Vorticella* cells on the sidewall of the channel (Figure 5-7(b)).

For the PDMS channel, an aluminum alloy mold was machined instead of a typical silicon wafer mold because of the channel height. After being peeled off from the mold, a cured PDMS channel body was bonded to No. $1\frac{1}{2}$ cover glass (22 mm×44 mm) with a plasma cleaner (Expanded Plasma Cleaner, Harrick Plasma, Ithaca, NY). The PDMS channel was connected to tube (inner diameter: 0.02 inch, Tygon Flexible Tubing, Saint-Gobain Performance Plastics, Granville, NY) with stainless steel tube (Type 304, New England Small Tube, Litchfield, NH).

Cell injection

Vorticella cells were cultured and harvested as described in Section 3.2. Cells on the bottom of a petri dish were scrapped and transferred to a small container. Harvested cells were centrifuged at 2,900 **g** for 10 minutes. After supernatant being removed from the container, suspended cells were injected into channels. Cells were allowed one or two days to attach to the channel's surface and to grow their stalk. During the procedure of harvest and cell injection, the number of injected cells was controlled for small number of cells to be injected into the channel because high population is not desirable as discussed in Section 5.4.3.

Experimental setup & procedure

As Figure 5-2 shows, one reservoir of the plastic channel was connected to a syringe (60 ml, BD, Franklin Lakes, NJ) installed on a syringe pump (PHD 22/2000, Harvard Apparatus, Holliston, MA), and the other reservoir was led to a waste dump. The

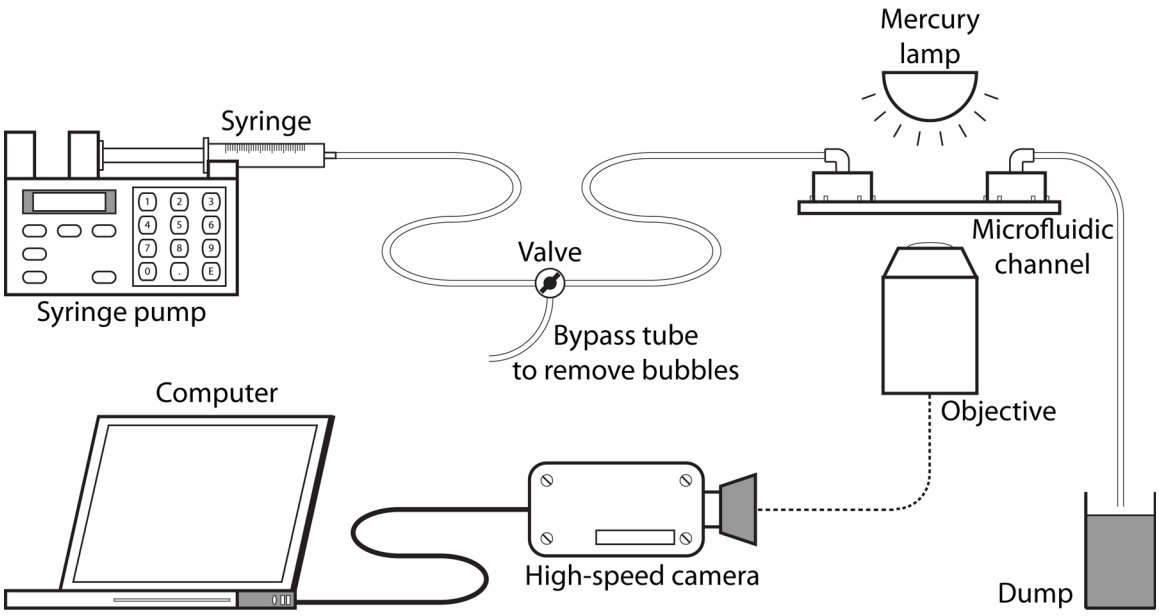

Figure 5-2: A schematic diagram of the microfluidic channel experiment setup.

tube connecting the syringe and the channel had a bypass valve and tube to remove air bubbles trapped inside the tube. In addition to spring water, PVP solutions of 1%, 2% and 3% w/w concentration (see Table 3.1 for fluid properties) were injected into the channel at various flow rates (1, 5, 10 and 15 ml/min).

For image acquisition, two high-speed cameras were used: Phantom V7 for high temporal resolution (10,000 fps) to analyze the dynamics of stalled contraction and FASTCAM-PCI (Photron, San Diego, CA) for low temporal resolution (30 fps) to analyze the effect of the stall force on relaxation. The Nikon inverted light microscope was used with a 40× objective lens (NA 0.6) for the high frame rate imaging and a 20× objective lens (NA 0.45) for the low frame rate imaging. The size of acquired images is 512×256 pixels, and one pixel of images corresponds to 0.5 μm at 40× with Phantom V7 and 0.79 μm at 20× with FASTCAM-PCI. MATLAB was used to post-process images and to measure dimensions of cells.

A *Vorticella* cell was chosen from the experiment zone explained in Section 5.3.2. For each flow condition shown in Table 5.2, 4∼5 contractions of the cell were recorded. Between recordings, the cell was allowed to rest for a few minutes. When the medium needed to be changed to a different one, the injection rate was set to low (0.2∼0.5

ml/min) not to fatigue the cell, and the cell was allowed to rest for 10∼30 minutes after every medium replacement. The order of injection is from spring water to 3% PVP solution.[10] Depending on the cell's status, the medium viscosity and flow rate were determined. In some cases, low flow rate or low medium viscosity was tried in the middle of a high drag condition to examine whether the stalk contracted accordingly. If the cell showed abnormal contraction, the corresponding data set was discarded.

5.3 Flow inside the channel

5.3.1 Poiseuille flow in a rectangular channel

Knowing flow condition inside the channel is essential to design the experiment and to develop a model for contraction force estimation. Because of the rectangular cross-section, fully developed flow inside the channel is two-dimensional Poiseuille flow. The profile of the streamwise velocity (V) is given as

$$V(y,z) = \frac{16w^2}{\mu\pi^3}\left(-\frac{dp}{dx}\right)\sum_{i=1,3,5,\cdots}^{\infty}(-1)^{(i-1)/2}\left[1-\frac{\cosh(i\pi z/2w)}{\cosh(i\pi h/2w)}\right]\frac{\cos(i\pi y/2w)}{i^3} \quad (5.1)$$

where x is the streamwise direction, y is the spanwise direction ($-w \leqq y \leqq w$), z is the binormal direction ($-h \leqq z \leqq h$), dp/dx is the streamwise pressure gradient, and $2h$ and $2w$ are the height and width of the rectangular channel, respectively (Figure 5-3) [112]. In the case of the plastic channel, $2h$ is 0.4 mm, and $2w$ is 5 mm. The center velocity ($V_{ch} = V|_{y=0,z=0}$) is given as

$$V_{ch} = \frac{16w^2}{\mu\pi^3}\left(-\frac{dp}{dx}\right)\sum_{i=1,3,5,\cdots}^{\infty}\frac{(-1)^{(i-1)/2}}{i^3}\left[1-\frac{1}{\cosh(i\pi h/2w)}\right] \quad (5.2)$$

and the velocity profile in the vertical symmetry plane ($y = 0$) is parabolic:

$$V(y=0,z) = V_{ch}\left[1-\left(\frac{z}{h}\right)^2\right]. \quad (5.3)$$

[10]The reverse order was tried, but the reverse order is undesirable because the cell was exhausted too quickly, i.e., the cell would not contract or showed incomplete contraction.

With the given pressure gradient, the flow rate through the channel (Q_{ch}) is given as [112]

$$Q_{ch} = \frac{4w^3h}{3\mu}\left(-\frac{dp}{dx}\right)\left[1 - \frac{192w}{\pi^5 h}\sum_{i=1,3,5,\cdots}^{\infty}\frac{\tanh(i\pi h/2w)}{i^5}\right]. \tag{5.4}$$

Based on Eq. 5.2 and 5.4, the correlation between the center velocity and the flow rate is found as

$$V_{ch} = 0.0131 Q_{ch} \tag{5.5}$$

where the units of V_{ch} and Q_{ch} are m/sec and ml/min, respectively. Therefore, it is possible to convert the flow rate set by the syringe pump to the channel center velocity.

The basic assumption for obtaining Eq. 5.5 is that flow developing inside the channel is laminar. This assumption can be confirmed with the channel Reynolds number given as

$$\mathrm{Re}_{ch} = \frac{2\rho h V_{ch}}{\mu}. \tag{5.6}$$

In the case of water flow at 15 ml/min (the highest Reynolds number case from Table 5.2), the channel Reynolds number is about 157, which is smaller than the critical Reynolds number for the channel flow (≈ 2000) [112]. Therefore, flow inside the channel is laminar, and assuming Poiseuille flow is justified.

Furthermore, the channel flow rate was measured by measuring the volume of water from the channel for a certain period of time. The measured flow rate agreed well with that set by the pump. The center velocity was measured by tracking beads flowing fastest in the channel, and the measured center velocity agreed well with Eq. 5.5.

5.3.2 CFD simulation for experimental zone identification

According to the contraction force estimation model explained in Section 5.4, this experiment needs the cell lying in one-dimensional Poiseuille flow, i.e., the streamwise flow velocity changes only in the z-direction as Eq. 5.3. Therefore, it is necessary to identify the experiment zone inside the channel that has one-dimensional Poiseuille

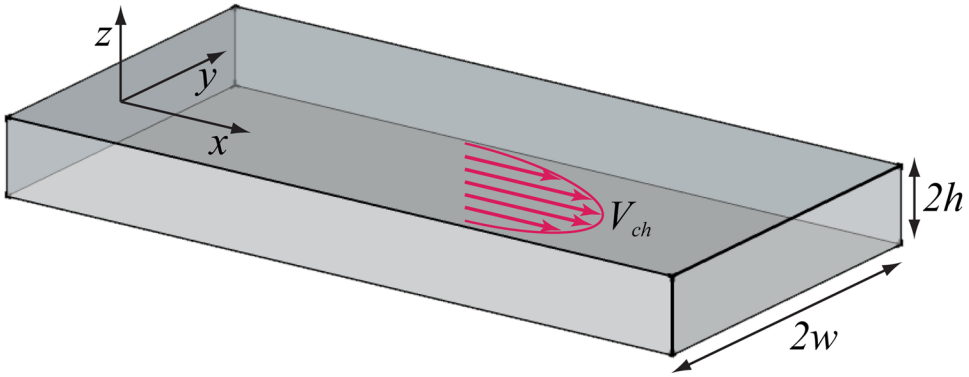

Figure 5-3: A diagram of the rectangular channel and Poiseuille flow. The height and width of the channel are $2h$ and $2w$, respectively. The x-direction is the streamwise direction, the y-direction is the spanwise direction, and the z-direction is the bi-normal direction. V_{ch} is the flow velocity at the channel center.

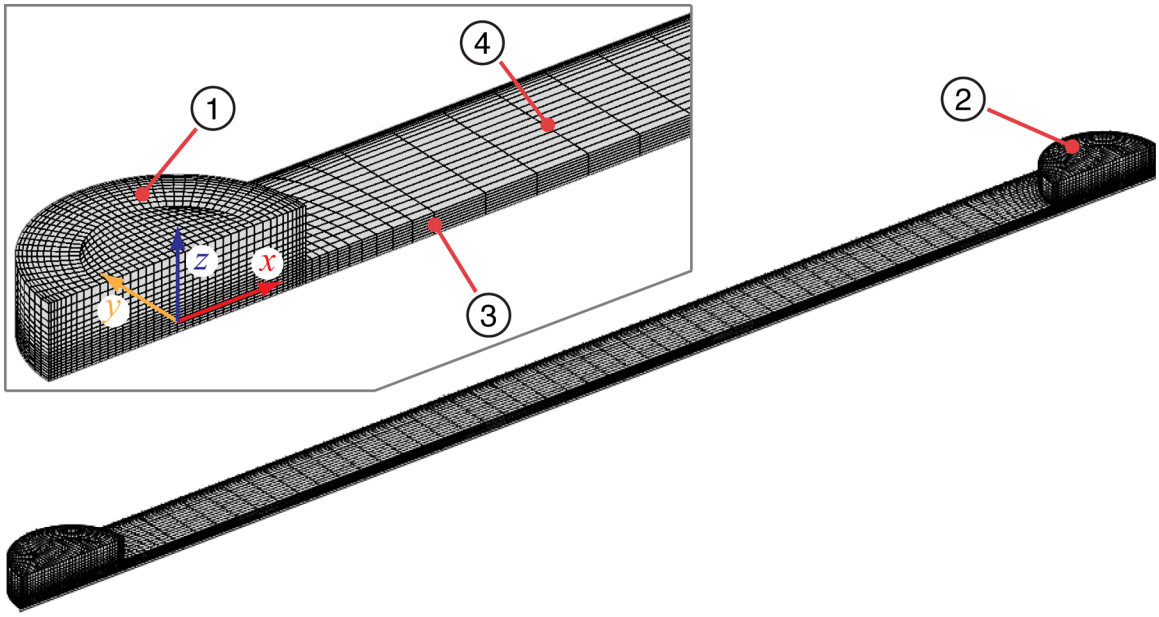

Figure 5-4: The three-dimensional mesh used for the channel flow simulation: The x-z plane ($y = 0$) is the plane of symmetry. The width of the mesh is 2.5 mm, and the heights of the channel part and the inlet/outlet are 0.4 mm and 1.4 mm, respectively. The inset is a magnified view of the inlet area, and it shows where the origin is. Assigned boundary conditions are the inlet condition for ①, the constant pressure condition for ②, the symmetric condition for ③, and the no-slip wall condition for ④ representing the rest surfaces.

flow because Eq. 5.1 and 5.5 are valid for fully developed flow, which is not the case around the channel's inlet and outlet. In other words, *Vorticella* cells in this zone were selected for the experiment. For this purpose, I simulated flow inside the channel using COMSOL Multiphysics.

The governing equations for incompressible flow of a Newtonian fluid (Eq. 3.1 and 3.8) were solved with the CFD simulation model made of hexahedron elements (Figure 5-4). Because the channel is symmetric with respect to the $y = 0$ plane, only half of the channel was modeled with both reservoirs omitted to save calculation time. As the inlet boundary condition for for the inlet (boundary ①), a paraboloidal velocity distribution was assumed as the following:

$$V_{\text{in}} = \frac{2Q_{ch}}{\pi w^2}\left(1 - \frac{x^2 + y^2}{w^2}\right). \tag{5.7}$$

The constant pressure boundary ($p_{\text{out}} = 0$) was assigned to the outlet (boundary ②), and for the plane of symmetry (boundary ③), the symmetric boundary condition was chosen. For the rest surfaces, the no-slip wall boundary condition was assigned. Flow inside the channel was simulated for water at 1, 5, 10 and 15 ml/min and 3% PVP solution at 10 ml/min.

Streamwise velocity profiles obtained from the simulation agree well with Eq. 5.1 and 5.5. Figure 5-5(a) shows that the center velocity reaches a constant value when the flow is fully developed (10 mm $< x <$ 40 mm) and that this value agrees well with Eq. 5.5. Figure 5-5(b) and (c) compare the streamwise velocity profile obtained from the analytic solution and that obtained at $x = 15$ mm from the CFD simulation. Both profiles agree well with each other.

Figure 5-6 shows streamwise velocity distribution at 20 μm from the channel bottom ($z = -180$ μm) where the zooid center is approximately located. Boundary layers growing on the sidewalls and developing flow near the inlet and outlet are clearly shown. Based on the CFD simulation results, the experimental zone was chosen as the blue-marked region in the middle of the channel (Figure 5-6), which is 10 mm $< x <$ 40 mm and -1.5 mm $< y <$ 1.5 mm.

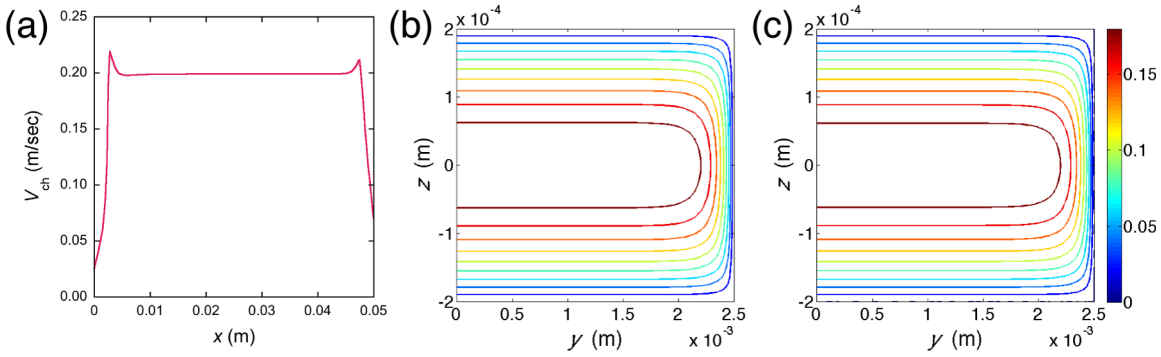

Figure 5-5: Streamwise velocity profiles obtained from the CFD simulation: (a) The center velocity as a function of x. (b) The streamwise velocity profile obtained from Eq. 5.1. (c) The streamwise velocity profile at $x = 15$ mm obtained from the CFD simulation. The channel flow rate is 15 ml/min, so the channel center velocity is about 0.2 m/sec. The scale of the color bar is m/sec.

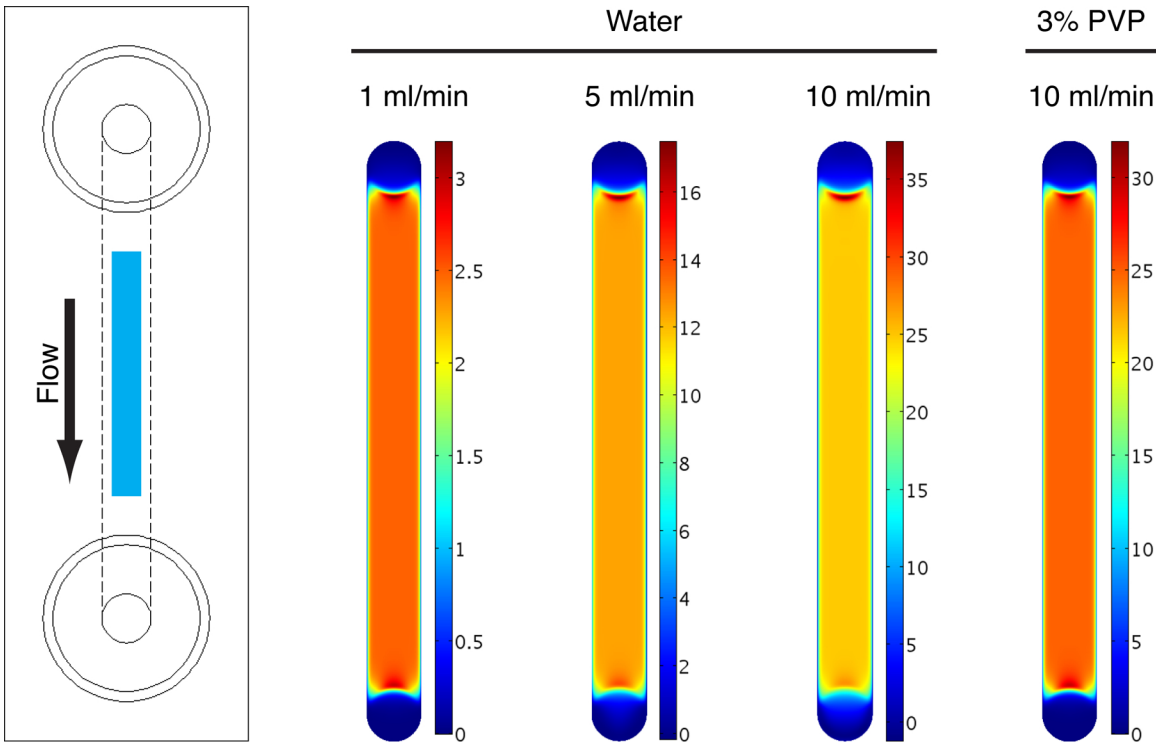

Figure 5-6: Streamwise velocity distribution at 20 μm from the bottom ($z = -180$ μm). The blue zone in the left channel diagram shows the experiment zone identified with the CFD simulation. The scale of color bars is cm/sec.

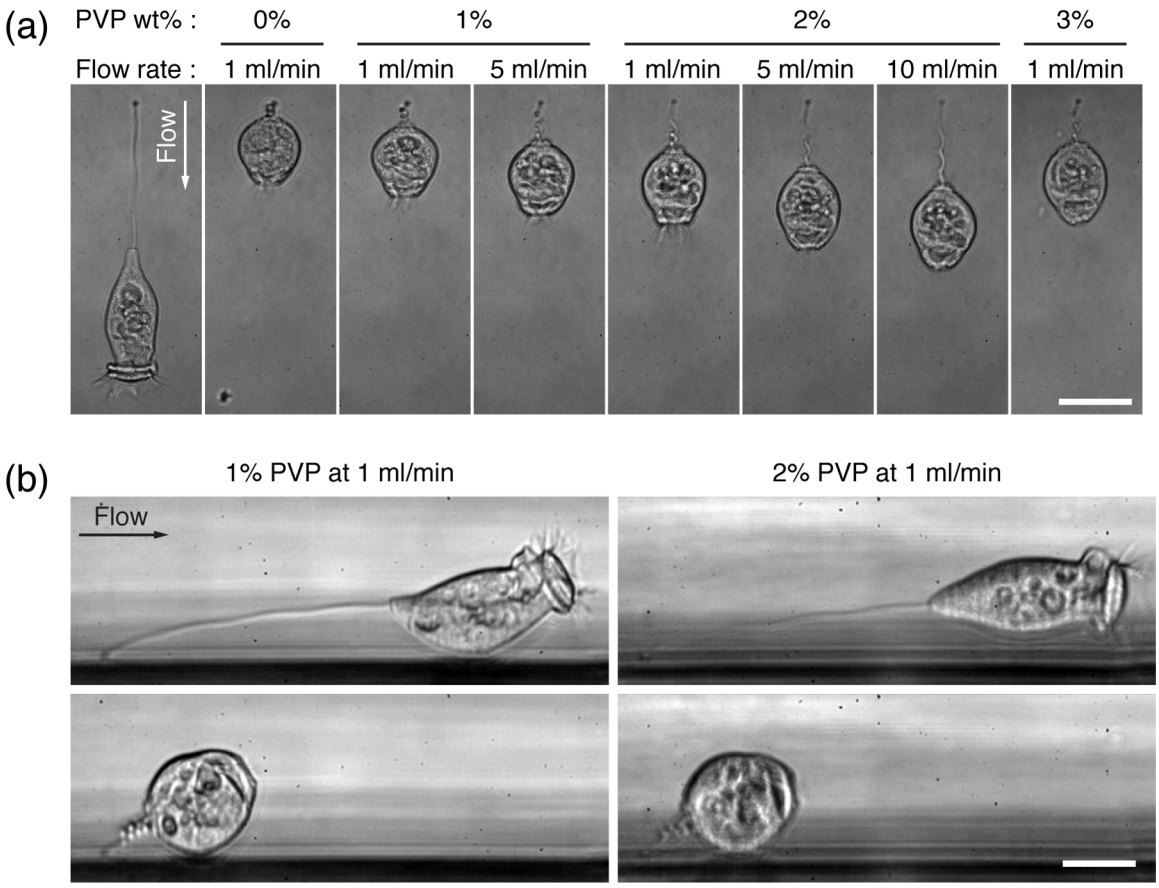

Figure 5-7: Stalled *Vorticella* cells in microfluidic channels: (a) Top view. (b) Side view. The size of scale bars is 50 μm.

5.4 Contraction force estimation model

5.4.1 Stalled *Vorticella* and its simplified model

The viscous drag force applied to *Vorticella* definitely retards the cell's stalk contraction. Figure 5-7(a) shows a *Vorticella* cell stalled in different flow conditions. As the viscous drag force increases, the cell's contraction distance decreases in contrast to contraction in stagnant viscous media, i.e., the end-to-end length of the contracted stalk increases. This suggests that it is possible to measure the stall force under which the stalk of *Vorticella* cannot contract at all and to estimate the isometric force of the stalk from the magnitude of this stall force. In contrast to the stalk, the contracted zooid is less affected by the drag force.

Based on Figure 5-7(b) showing another cell seen from the side in the PDMS channel, the zooid of extended *Vorticella* is assumed to be a body of revolution contacting the channel bottom with its axis of symmetry being parallel to the flow direction (Figure 5-8(a)). In the contracted state, the zooid is assumed to be a solid sphere contacting the channel bottom with its center lying on the extension of the line connecting both ends of the stalk (Figure 5-8(b)).

As Figure 5-8(c) shows, I measured the shortest distance from the stalk base to the zooid (S) and the radius or half width of the zooid (R and R_z) from acquired images. In the relaxed state, the end-to-end length of the stalk was calculated with

$$\begin{aligned} \theta &= \tan^{-1}\left(\frac{R_z}{S_{\max}}\right) \\ L_{s,\max} &= \frac{S_{\max}}{\cos\theta} \end{aligned} \tag{5.8}$$

where θ is angle between the stalk and the channel bottom. Contracted *Vorticella* has a different geometry from the relaxed state, so the end-to-end length of the stalk was calculated with

$$\begin{aligned} \theta &= \tan^{-1}\left(\frac{R}{R+S_{\min}}\right) \\ L_{s,\min} &= \frac{R}{\sin\theta} - R. \end{aligned} \tag{5.9}$$

As the drag force increases, θ becomes smaller, so $S_{\min}$ becomes closer to $L_{s,\min}$.

5.4.2 Forces on the contracted zooid

In the aforementioned model, the contractile force that the contracted stalk retains should be estimated based on the channel geometry, flow condition and the dimension of *Vorticella*. Because of the parabolic velocity profile of Poiseuille flow, the contracted zooid experiences the torque (T) as well as the drag force (F_d) as Figure 5-8(b) shows. Furthermore, there should be the lift force (F_l) on the zooid due to the inertia effect represented by the non-zero Reynolds number and and the friction force (F_f) due

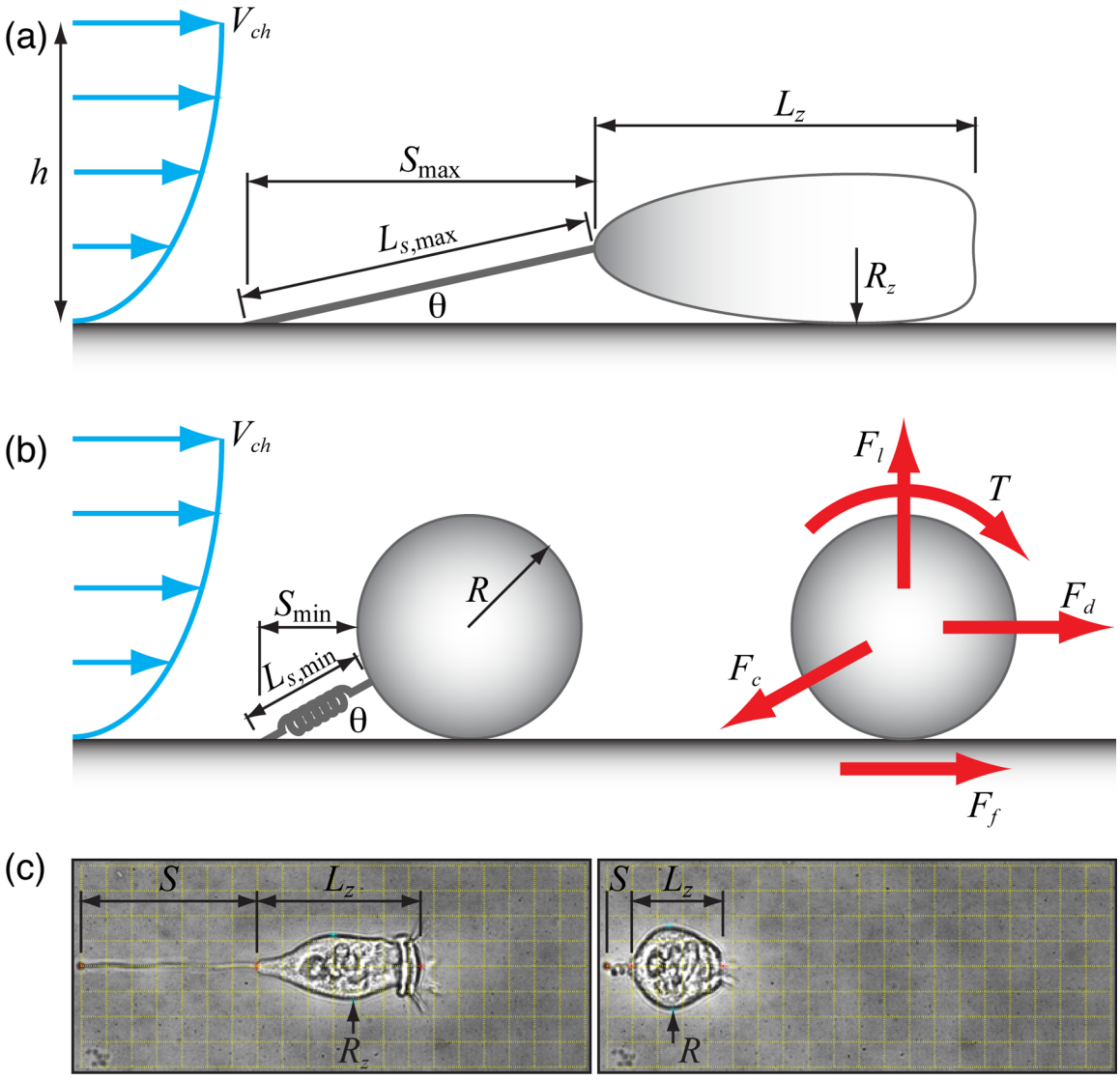

Figure 5-8: Simplified models for *Vorticella* in Poiseuille flow: (a) Relaxed state. (b) Contracted state. (c) Examples of dimensions measured from images (left: relaxed state, right: contracted state). S is the shortest distance between the stalk base and zooid, L_z is the zooid length, R_z is the zooid half width, θ is angle between the stalk and channel surface, F_l is the lift force, F_f is the friction force, and T is the torque.

to physical contact between the zooid and channel surface. However, the contractile force (F_c) of the stalk depends only on the drag force and torque as the following:

$$F_c = \frac{F_d + \dfrac{T}{R}}{\cos\theta} \tag{5.10}$$

The above relation is obtained from torque balance at the zooid-surface contact point. In the case of a sphere fixed in creeping Poiseuille flow, the drag force and torque are estimated with

$$\begin{aligned} F_d &= 6\pi\mu R V_{ch} F^p \\ T &= 8\pi\mu R^2 V_{ch} T^p \end{aligned} \tag{5.11}$$

where F^p and T^p are correction factors that reflect the effect of the parabolic profile on the drag force and torque.

For low Reynolds number flow, these correction factors are determined solely by a ratio of the sphere diameter to the channel height (R/h). Having calculated motion of a spherical particle in Poiseuille flow in a two-dimensional channel using the boundary-integral method, Staben et al. suggested values of the correction factors in the limit of infinitesimally small spacing between the sphere and channel wall [93]. These correction factors approach constant values in the limit, and values of the factors are summarized in Table 5.1 as a function of R/h for the range of $0.1 \leqq R/h \leqq 0.95$.

On the other hand, Poiseuille flow can be represented with semi-infinite unidirectional shear flow parallel to a plane wall of which the unperturbed velocity field is

Table 5.1: Correction factors for drag forces and torque on a sphere in Poiseuille flow in the limit of infinitesimally small gap between the sphere and channel surface [94].

	R/h									
	0.1	0.2	0.3	0.4	0.5	0.6	0.7	0.8	0.9	0.95
ΔF^t	2.51	2.10	1.86	1.71	1.60	1.54	1.51	1.50	1.50	1.50
F^p	0.32	0.61	0.89	1.15	1.42	1.69	1.95	2.21	2.45	2.57
T^p	0.085	0.15	0.20	0.24	0.26	0.25	0.23	0.17	0.098	0.052

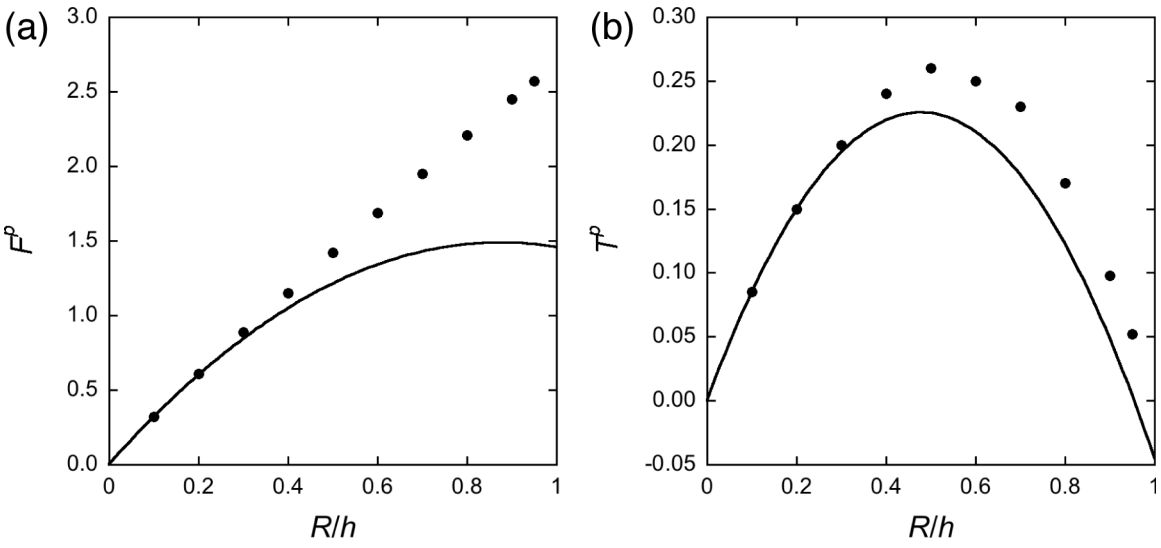

Figure 5-9: A comparison of the drag and torque correction factors for Poiseuille flow: (a) The drag force correction factor. (b) The torque correction factor. Solid line - Eq. 5.12 [76] and solid dot - Table 5.1 [94].

expressed with a second-order polynomial. In contrast to Poiseuille flow, the semi-infinite flow has only one wall. Having calculated the drag force and torque on a spherical particle fixed on the wall in the semi-infinite flow with the boundary element method (BEM), Pozrikidis proposed the following correlations for the correction factors [76]:

$$\begin{aligned} F^p &= \frac{1}{3}\Big(\frac{R}{h}\Big)\left[10.2 - 5.82\Big(\frac{R}{h}\Big)\right] \\ T^p &= \frac{1}{4}\Big(\frac{R}{h}\Big)\left[3.78 - 3.96\Big(\frac{R}{h}\Big)\right]. \end{aligned} \tag{5.12}$$

Pozrikidis suggested that the above expressions can give reasonable predictions of F^p and T^p for Poiseuille flow when $h > 3R$ and accurate predictions when $h > 5R$. Pasol et al. had a similar approach using the bipolar coordinates technique, and their correction factor correlations agree well with those of Pozrikidis (see Appendix B)[73].

Figure 5-9 compares Eq. 5.12 and Table 5.1. As Pozrikidis suggested, his correlations agree well with Staben et al.'s result when $R/h < 0.2$. Because R/h is about 0.1 for the most cases in this study, Eq. 5.12 was used to calculate the drag force and

torque on the contracted zooid.

5.4.3 Other flow and force considerations

I selected several flow conditions in which the particle Reynolds number of the contracted zooid is small so that Eq. 5.11 is valid for the current experiment. For a sphere fixed at the channel surface in Poiseuille flow, the particle Reynolds number is defined with shear rate on the wall as

$$\mathrm{Re}_s = \frac{2\rho R^2 V_{ch}}{\mu h}. \tag{5.13}$$

Flow around the sphere can be regarded as the creeping flow when the above Reynolds number is less than 0.2 [14]. Flow conditions for the stall experiment were selected based on this Reynolds number criterion, and they appear bold in Table 5.2.

However, the Reynolds number criterion is loosely applied in low PVP concentration cases such as 0% and 1% PVP solutions. Although the drag force is expected to be higher than Eq. 5.11 at the small but finite Reynolds number, using the equation for such cases seems reasonable because the estimated contraction force is relatively small compared to the force estimated in other cases of higher stall force.

On the other hand, the drag force increase due to the inertia effect in Poiseuille flow can be roughly estimated with an inertia effect correction factor for Couette flow. Zeng et al. calculated forces on the sphere placed near the wall in Couette flow using the direct numerical simulation (DNS) [115]. First, they found a fit for the zero Reynolds number drag force as a function of the dimensionless spacing between the

Table 5.2: The Reynolds number of the contracted zooid in the channel ($R = 20$ μm).

PVP	ρ	μ	Flow rate (ml/min)			
wt %	(g/cm^3)	(mPa·sec)	1	5	10	15
0%	1.000	1.00	**0.052**	0.262	0.524	0.786
1%	1.001	2.74	**0.019**	**0.096**	**0.191**	0.287
2%	1.003	6.93	**0.008**	**0.038**	**0.076**	**0.114**
3%	1.005	10.31	**0.005**	**0.026**	**0.051**	**0.077**

sphere and the wall ($\delta = H/R - 1$) as the following:

$$C_{d0} = \frac{24}{\mathrm{Re}}\left(1 + 0.138\exp(-2\delta) + \frac{9}{16(1+2\delta)}\right) \tag{5.14}$$

where C_{d0} is the drag coefficient at the zero Reynolds number. They incorporated the Reynolds number dependence into the drag formula as the following:

$$C_d = C_{d0}(1 + \alpha_s \mathrm{Re}^{\beta_s}) \tag{5.15}$$

where

$$\begin{aligned} \alpha_s &= 0.150 - 0.046(1 - 0.16\delta^2)\exp(-0.7\delta) \\ \beta_s &= 0.687 + 0.066(1 - 0.76\delta^2)\exp(-\delta^{0.9}). \end{aligned} \tag{5.16}$$

For a sphere in contact with the wall, δ becomes zero, so the above drag correlation becomes

$$\lambda_{C_d} = \frac{C_d}{C_{d0}} = 1 + 0.104\mathrm{Re}^{0.753} \tag{5.17}$$

When Re = 1, this ratio is 1.104, which means that, in the case of a stationary sphere fixed on the wall in Couette flow, it causes about 10% underestimation to use the zero Reynolds number drag force formula. Therefore, the order of magnitude of the error is acceptable which is caused by using Eq. 5.11 and 5.12 even when Re > 0.2.

One more thing to be considered is fluid dynamic interaction among neighboring cells inside the channel. Brooks and Tozeren simulated laminar flow in a parallel-plate flow channel of which the bottom plate has an array of uniformly aligned spheres [14]. They found that the drag force on a single sphere depends on relative positions with other spheres. First, if the channel has an array of spheres on both the top and bottom surfaces, the drag force increases compared to the channel having the same array only on either of the surfaces. Second, the drag force decreases as the sphere-to-sphere distance decreases. Sugihara-Seki and Skalak also numerically tested the hydrodynamic interaction between adjacent spheres attaching on the inner surface of a circular tube [100]. Their results indicate that the interaction is negligible when

$l/R_{tube} \geqq 3$. Here, l is the distance between neighboring spheres, and R_{tube} is the inner radius of the tube. Therefore, to avoid hydrodynamic interaction among cells, the number of injected cells was controlled, and a *Vorticella* cell was chosen for the experiment which did not have neighboring cells on both the top and bottom surfaces.

5.5 Results

5.5.1 Isometric force and its stalk length dependence

Figure 5-10 shows four measurement cases of the contraction force developed by the stalk of *Vorticella* stalled by the viscous drag force. As the stall force increases, both the contractile force and the stalk length ratio ($L_{s,\min}/L_{s,\max}$) increase. This indicates that *Vorticella* generates greater contractile force contracting over shorter distance. In addition, the contractile force appears to increase linearly with respect to the stalk length ratio. $L_{s,\min}/L_{s,\max} = 1$ means that the *Vorticella* stalk cannot shorten at all although it would contract, so the contractile force at this point is the isometric force of the *Vorticella* stalk. Therefore, the isometric force (F_{iso}) was estimated with a linear extrapolation of the contraction force against the stalk length ratio. Black lines in Figure 5-10 show linear regression results, and they well represent experimental data. The estimated isometric force is in the order of a few hundreds nN (150∼350 nN), and these results agree with measurement results of France [27]. The corresponding isometric tension is $0.85 \sim 1.98 \times 10^5$ N/m^2, which is comparable to that of muscle ($10^5 \sim 10^6$ N/m^2 from [1]).

It is noticeable in Figure 5-10 that the isometric force of the longer stalk is greater than that of the shorter stalk. This suggests that *Vorticella* with a longer stalk can generate greater contractile force. To examine whether the isometric force of the *Vorticella* stalk has a correlation with the relaxed stalk length, I plotted in Figure 5-11 the isometric force values measured from more than ten cells as a function of the relaxed stalk length. The isometric force appears approximately linearly dependent on the stalk length, and this suggests that the contractile force maximally generated

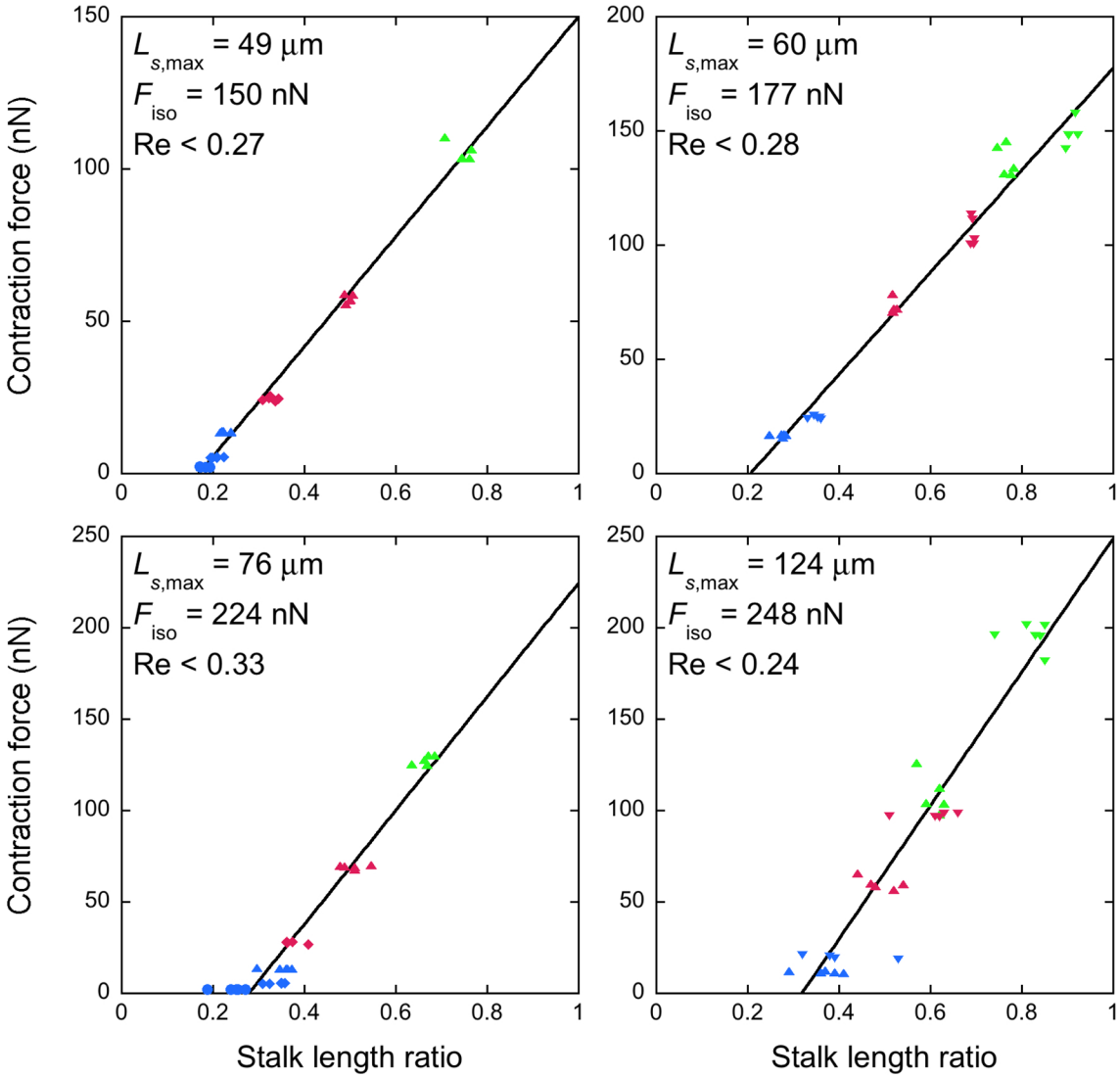

Figure 5-10: The contractile force developed by the stalk of stalled *Vorticella* as a function of the stalk length ratio ($L_{s,\min}/L_{s,\max}$). Each graph shows the length of the relaxed stalk ($L_{s,\max}$), estimated isometric force (F_{iso}) and the maximum Reynolds number. ● - 0% PVP, ♦ - 1% PVP, ▲ - 2% PVP, ▼ - 3% PVP, blue - 1 ml/min, red - 5 ml/min and green - 10 ml/min.

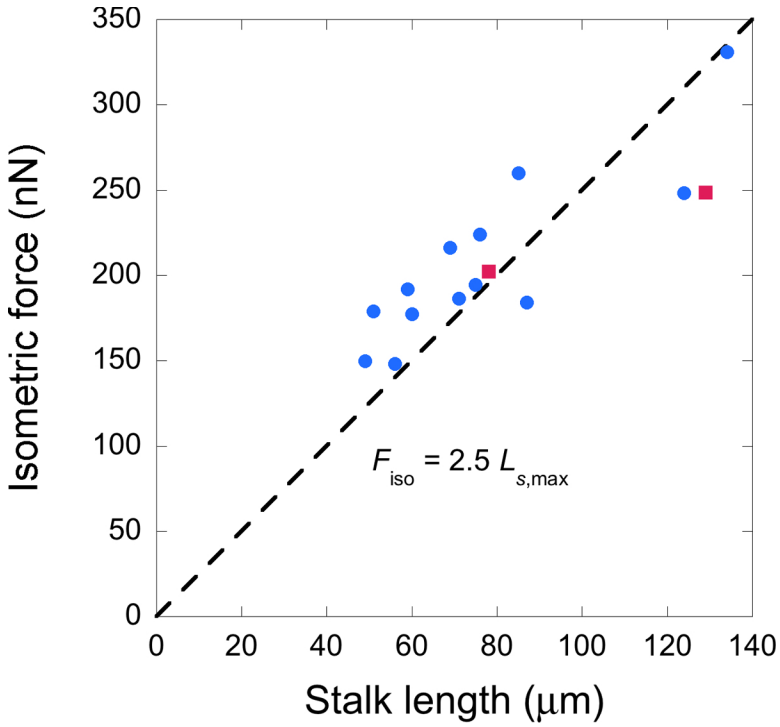

Figure 5-11: The isometric force of the *Vorticella* stalk as a function of the relaxed stalk length. Red squares show the isometric force of a cell measured before and after its stalk growth. The dashed line shows linear regression.

by the unit length of the stalk is roughly constant. The dashed line in the graph is a linear regression line that passes through the origin because the *Vorticella* stalk with zero length cannot generate the contraction force. Because the slope of the regression line is 2.5, 1 μm of the spasmoneme seems to generate the contraction force up to about 2.5 nN.[11]

5.5.2 Maximum force per contractile element

This stalk length dependence of *Vorticella*'s isometric force can be connected to motility models suggested for the spasmonemal contraction or centrin-based contraction [6, 82]. As introduced in Section 1.3, the common idea of these models is that nanofilaments responsible for contraction consist of a calcium-binding protein (spasmin/centrin) and its binding partner (spaconnectin/sfi1p-like protein) and that these

[11]The length of the spasmoneme is a little longer than that of the stalk because the spasmoneme is helically wound inside the stalk. See [97] for spasmoneme length calculation.

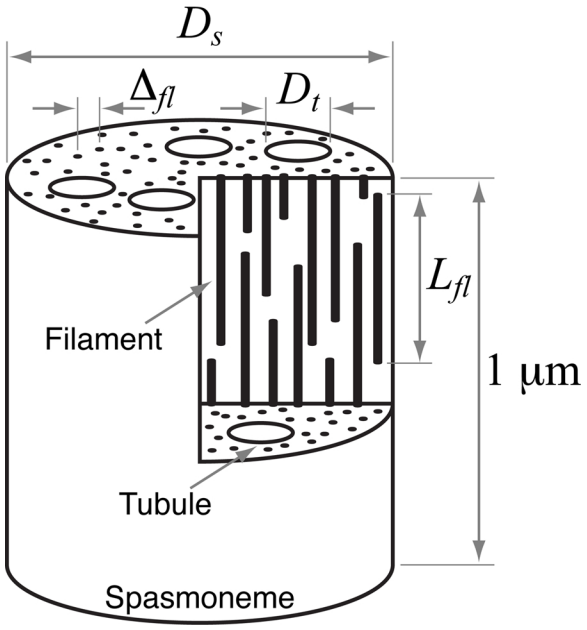

Figure 5-12: A diagram of the spasmoneme's structure: D_s and D_t are the average diameter of the spasmoneme and tubules, respectively. Δ_{fl} is average spacing between filaments, and L_{fl} is the average length of filaments.

filaments shorten with conformation change on calcium binding. The following three assumptions are reasonable: filaments have similar length, each filament generates a certain magnitude of force maximally, and the number of filament per the unit volume of the spasmoneme is constant along the spasmoneme. Then, the isometric force of the spasmoneme will be determined by the number of force-generating filaments. Because the cross-section area of the spasmoneme is rather constant compared to the length among *Vorticella* cells, the isometric force linearly depends on the length of the spasmoneme.

Based on the aforementioned model and isometric force measurement result, I here attempt to estimate the maximum contraction force that each spasmonemal filament can develops. As introduced in Section 1.2, the spasmoneme consists of nano-diameter filaments and tubules. From a simplified diagram of the spasmoneme of which the length is 1μm (Figure 5-12), the number of filaments in the spasmoneme (N_{fl}) is given as

$$N_{fl} \approx \frac{D_s^2 - N_t \cdot D_t^2}{\Delta_{fl}^2} \cdot \frac{1}{L_{fl}} \tag{5.18}$$

where N_t is the average number of tubules found in the cross-section of the spasmoneme. Because 1 μm of the spasmoneme can develop the contraction force up to about 2.5 nN, the contraction force per filament (F_{fl} in nN) is given as

$$F_{fl} \approx \frac{2.5}{N_{fl}}. \tag{5.19}$$

The necessary dimensions can be measured from high-resolution images of the spasmoneme. The *Vorticella* spasmoneme has about 60 tubules in the transverse section of which the diameter is about 60 nm, and tubules are about 250 nm apart whereas the average spacing of the filaments is about 3 nm [3]. Because the diameter of the spasmoneme is about 1.5 μm, the number of the contractile filaments in the cross-section of the spasmoneme is approximately 226,000. However, the length of the filament is still undetermined [1, 92]. Although Amos observed in the spasmoneme of *Zoothamnium geniculatum* that the filaments showed beaded appearance of which the longitudinal periodicity was about 3.5 nm [4], it is not clear whether this longitudinal periodicity is related to the filament length. The length of the spasmonemal filament may be assumed based on similar centrin-based contractile filaments. Li et al. measured that the length of a filament containing about 15 repeats of Sfi1p-centrin complex is about 60 nm [55], and Gogendeau et al. estimated that a filament of PtCenBP1p with 89 centrin molecules is about 600 nm [30].

On the other hand, it is possible to estimate the maximum force per spasmin molecule. As Section 3.4.3 shows, it is postulated that 1.57×10^{-17} moles of calcium ion bind to 1 μm of the spasmoneme. With Avogadro's constant, this value is converted to 9.46×10^6 atoms of calcium per 1 μm of the spasmoneme. Because a molecule of spasmin binds to about two calcium ions [78], it can be assumed that 1 μm of the spasmoneme has about 4.73×10^6 molecules of spasmin. With this number of spasmin molecule, the linear dependence in the isometric force of the spasmoneme leads to a conclusion that a molecule of spasmin may generate force up to 0.53 fN. However, caution should be exercised here because the number of calcium ions binding to the unit length of the spasmoneme was estimated based on the measurement

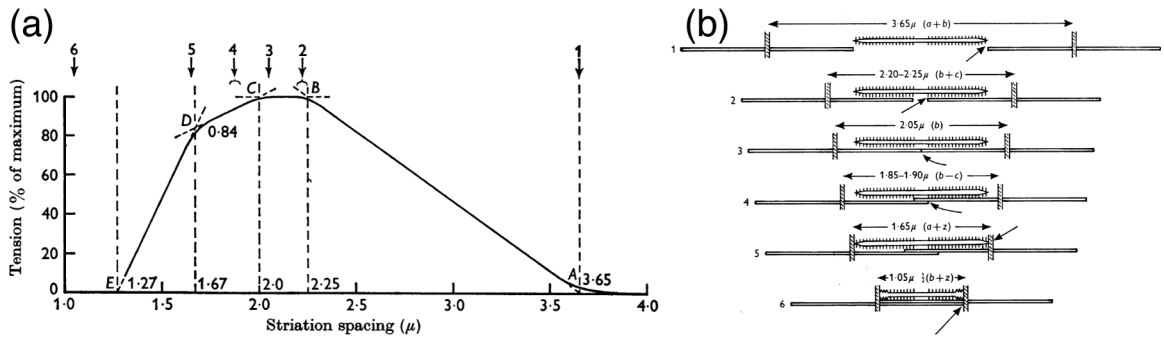

Figure 5-13: The isometric tension of muscle (the figures from [32]): (a) Change of the isometric tension as a function of the sarcomere length of muscle. (b) A diagram of the muscle fiber.

with *Zoothamnium*, not *Vorticella*. Although they are relatives, their contraction characteristics can be different.

5.6 Discussion

5.6.1 Isometric tension of muscle

What is the meaning of the linear dependence of the isometric force on the stalk length? The isometric tension of striated muscle gives clues. In contrast to the spasmoneme, the isometric force of muscle depends not on its length but on its cross-sectional area [98]. In other words, adding muscle fibers in series does not increase the isometric force, but adding them in parallel does. These characteristics of the muscle isometric force are opposite to the spasmoneme that differs not in its diameter but in its length among cells.

However, the isometric tension of a single muscle fiber depends on its sacormere length [32]. In Figure 5-13(a), the isometric tension of the muscle fiber increases as the sacormere length increases. After reaching its maximum, the isometric tension decreases as the sacormere length further increases. This behavior of the isometric tension is explained with the structural change of the muscle fiber as shown in Figure 5-13(b). The striated muscle fiber consists of a thick filament, thin filaments and myosin heads that bridge both filaments. As the sacormere length increases, the

length of overlapped thin filaments decreases, and the effective number of myosin heads increases (4-6 in Figure 5-13). When thin filaments are not overlapped and all the myosin head participate in force generation, the isometric tension of the muscle fiber becomes maximum (2-3 in Figure 5-13). As the sacormere length increases further, the isometric tension decreases because the effective number of myosin heads decreases (1-2 in Figure 5-13). This sacormere-length dependence of the muscle fiber's isometric tension suggests that the isometric tension is determined by the number of force generating units. This idea can be applied to the spasmoneme as shown in Section 5.5.2.

5.6.2 Effects of the stall force on *Vorticella*

The stall force exhausts *Vorticella*, and an exhausted cell is unable to use the whole spasmoneme for contraction. After experiencing the high stall force, some *Vorticella* cells showed partial coiling of their stalk with the stalk remaining straight around the base or initiation of coiling in the middle of the stalk. Sugi observed that a stalk of *Carchesium* showed localized and incomplete contractions as the stalk was more exhausted, so he concluded that an "all-or-nothing" type of contraction is invalid for the fatigued stalk [95]. In addition, he observed that contraction began at the point of the stalk to which a stimulation was applied in the case of the fatigued stalk [96]. Ueda also mentioned abnormal contractions of the severely fatigued *Carchesium* stalk [103]. However, although *Vorticella* was given time to rest during the experiment, fatigue was unavoidable especially in the high stall force condition, and it can be a cause for the variance of the measured isometric force.

I also observed that *Vorticella* exhausted by the high stall force did not contract for a long time and that peristomial cilia of the zooid were not exposed. Patterson had the same observation that *Vorticella convallaria* cells became non-responsive more frequently and for a longer time as they were stimulated repeatedly [74]. He suspected that the mechanoreceptors of the zooid are located in the oral region because *Vorticella* remained insensitive to restimulation if the oral region, including the oral grove and peristomial cilia, was not exposed. Patterson tried to connect this de-

crease in responsiveness of *Vorticella* to calcium ions that may modify the cytoplasmic properties of the cell.

Another effect of the stall force on *Vorticella* is that the stall force seems to stimulate growth of the stalk. The stalk of a few cells grew longer after experiencing the viscous drag force. One example is shown in Figure 5-11 (red squares). The stalk length of the cell was 78 μm during the first channel experiment, and the stalk grew to 129 μm in about 24 hr. This case not only supports the observation of this study that the longer stalk generates the contraction force more but also raises a question about the mechanosensory mechanism of *Vorticella convallaria*.

THIS PAGE INTENTIONALLY LEFT BLANK

Chapter 6

Dynamics of stalled contraction

6.1 Introduction

Vorticella convallaria contracting under the external drag force behaves differently than it does in normal conditions or passive loading conditions. While the cell can fully contract even in a highly viscous medium if the medium is quiescent, it slowly contracts over shorter distance in viscous fluid flow as shown in Figure 5-7(a). Furthermore, it was observed that, under the high drag force, the stalk started coiling a while after the zooid contraction was almost completed. These observations suggest that the contraction dynamics of *Vorticella* in an active loading condition be different from that in a passive loading condition.

France analyzed the contraction dynamics of *Vorticella convallaria* stalled with a micropipette [27]. She obtained the ensemble-averaged stalk length data from contractions of several different cells grabbed by the same micropipette and used the data to calculate the contraction rate of stalled *Vorticella*. In other words, one micropipette was used for several cells, and one set of stalk length data was obtained from those cells for each micropipette. This ensemble average cannot retain differences among cells. As Section 5.5.1 shows, the isometric force of the *Vorticella* stalk depends on the relaxed stalk length, so the contraction dynamics should be different among cells having different length of the stalk. In contrast to France's approach, the microfluidic channel enables observing several contractions of a *Vorticella* cell in a

certain stalling condition, i.e., the medium viscosity and channel flow rate. Therefore, it is possible to ensemble-average the time course of the stalk length of a single cell over several contractions in different loading conditions.

In this chapter, I characterize the stalled contraction of *Vorticella* by measuring the dimension of the cell, the contraction rate, the propagation speed of stalk coiling and the contraction latency. As the stall force increases, the maximum contraction speed of *Vorticella* decreases, and the time to the maximum contraction speed increases whereas the propagation speed of stalk coiling does not change much. The contraction latency between the zooid and stalk also increases with the increasing stall force, and measuring the contraction latency enables estimating the maximum contraction force developing rate of the spasmoneme, which is 40∼50 nN/msec. The contraction energetics show that the stalled contraction of *Vorticella* is limited in the total work, not in its maximum power output, in the active load.

6.2 Methods

Zooid volume measurement

The zooid was assumed to be a body of revolution shown in Figure 6-1(b). Six points including the zooid-stalk junction and the other vertex of the zooid were picked from a half of the zooid profile (for example, the upper half in Figure 6-1(a)), and the volume of the corresponding body of revolution was calculated as the following:

$$V_z \approx \frac{\pi}{3}\left[h_1 r_1^2 + h_2(r_1^2 + r_1 r_2 + r_2^2) + h_3(r_2^2 + r_2 r_3 + r_3^2) + h_4(r_3^2 + r_3 r_4 + r_3^2) + h_5 r_4^2\right] \quad (6.1)$$

where V_z is the volume of the zooid, and r_i and h_i are the radii and heights of the body segments, respectively. The same procedure was repeated for the other half of the zooid profile, and two values of the volume was averaged.[12] The volume of the contracted zooid was measured with the same procedure.

[12]Compared to Figure 5-8(a), $L_z = \sum_i h_i$ and $R_z = \max(r_i)$.

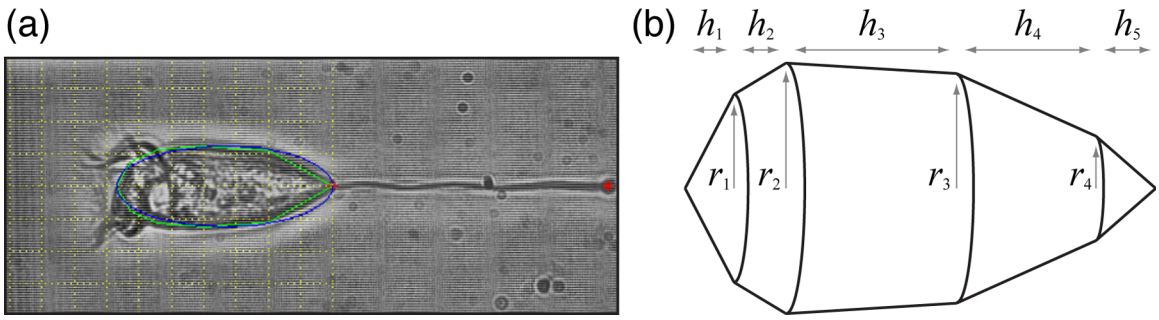

Figure 6-1: Measurement of the zooid volume: (a) An example of the zooid volume measurement. The green polygon inside the zooid is made by connecting points picked from the zooid profile, and it shows the longitudinal cross-section of the corresponding body of revolution from which the zooid volume is calculated. The blue ellipse has the same major and minor radius as those of the zooid. (b) A body of revolution approximated for the zooid. r_i and h_i are the radius and height of each segment, respectively.

Stalk & zooid length measurement

The end-to-end length of stalled *Vorticella*'s stalk and zooid was measured by acquiring the coordinates of three points (the stalk base, the zooid-stalk junction and the stoma of the zooid) with MATLAB from captured images as shown in Figure 5-8(c). Because the stalk is not parallel to the channel bottom, the measured stalk length is the length of the projected stalk (S in Figure 5-8).[13] Therefore, the calculated contraction rate is the component of contraction rate parallel to the bottom surface. In contrast, the measured zooid length (L_z in Figure 5-8) is not a projected dimension because the body is roughly parallel to the bottom surface (Figure 5-7(b)).

In measuring the length, not all frames were used because the decrement of the stalk length per frame was smaller than one pixel in the later stage of contraction. About 20∼50 frames after the zooid began to contract, images were sampled so that the stalk length decrement between adjacent images was greater than one pixel. For ensemble average, the stalk and zooid length data were linearly interpolated for

[13] As explained in Section 5.4.1, S is the shortest distance between the stalk base and the zooid, not the projected length of the stalk, especially in the contracted state. However, it is reasonable to regard S as the projected length of the stalk because the stalk length change near the maximum contraction speed, usually in the early phase of contraction, is important in terms of the contraction dynamics.

missing time steps after the data were adjusted so that the stalk began to coil at $t = 0$ msec. Because the contraction rate is low in the later stage, this sample with linear interpolation does not alter the contraction dynamics. For each flow condition, the stalk length data from 4∼5 contractions were averaged.

Bead attachment

To measure the propagation speed of stalk coiling, 1 μm diameter polystyrene beads were attached to the stalk according to Upadhyaya et al.'s protocol [104]. The beads (10 μl of 10% suspension) were rinsed two times with deionized water (centrifuged at 10,000 **g** for 1 min) and mixed with 800 ml of poly-L-lysine solution diluted to 0.25 mg/ml (0.1 w/v%, Sigma-Aldrich, St. Louis, MO). After being incubated overnight at 4°C, the glue-coated beads were washed one more time with spring water, and 200∼300 μl of the bead solution was injected into the microchannel prepared as described in Chapter 5.2. Beads were found to attach *Vorticella* cells' body and stalk several minutes after the injection. While the poly-L-lysine coated beads endured the shear stress or drag force from the viscous medium in the case of normal contractions, they slid on the cell or detached from the cell in the case of the high drag force [104]. Although beads well adhering to the stalk were chosen to calculate the propagation speed of stalk coiling, stronger bond may be possible with Nagai et al.'s protocol using the streptavidin-biotin bond [70].

6.3 Results

6.3.1 Volume and aspect ratio of the zooid

The dimension of two *Vorticella* cells' zooid was measured and averaged over 4∼6 contractions (Figure 6-2, error bars are not shown for clarity). Although the averaged volume shows fluctuation, the volume seems to remain roughly constant irrespective of the stall force because its standard deviation is not small enough to make this fluctuation meaningful. On the other hand, a question was raised whether the zooid

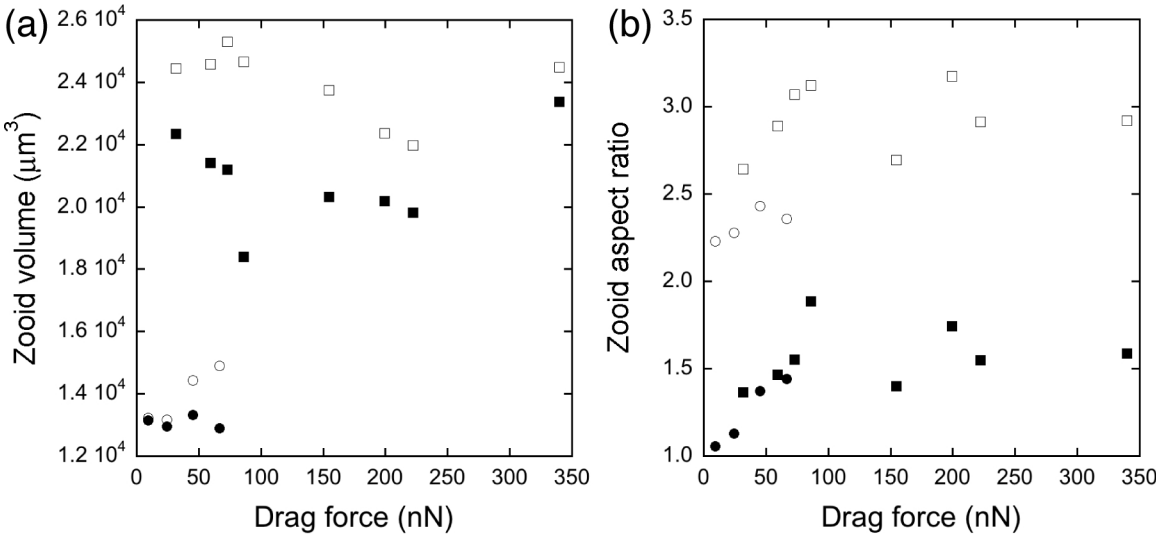

Figure 6-2: The averaged volume and aspect ratio of the *Vorticella* zooid: (a) The zooid volume. (b) The aspect ratio of the zooid. The drag force shown is the stall force on the contracted zooid at the end of contraction. Circle - cell #1, square - cell #2, void - relaxed state and solid - contracted state.

volume is constant before and after contraction. If the volume of the shrunken zooid is smaller than that of the relaxed one, the stalk contraction may be related to injection of the zooid cytoplasm into the stalk. Although the volume of the contracted zooid appears smaller than that of the relaxed zooid in Figure 6-2(a), more accurate measurement of the zooid volume is required to answer the question because of the large standard deviation.

The aspect ratio of the zooid ($L_z/2R_z$, R instead of R_z for the contracted zooid) is measured (Figure 6-2(b)). In contrast to the measured volume, the standard deviation of the aspect ratio is small enough for the averaged value to represent a trend. The stall force stretches the zooid in both the relaxed and contracted states. With the constant volume, the increasing length of the zooid means the decreasing radius of the zooid and hence the increasing aspect ratio. However, the aspect ratio appears to reach a constant value over about 100 nN of the stall force. This limitation in zooid stretching seems related to its cytoskeletal structure and elastic characteristics. At the high stall force, the zooid becomes a shape similar to a rain drop, which is thought to be its adaptation to high shear stress.

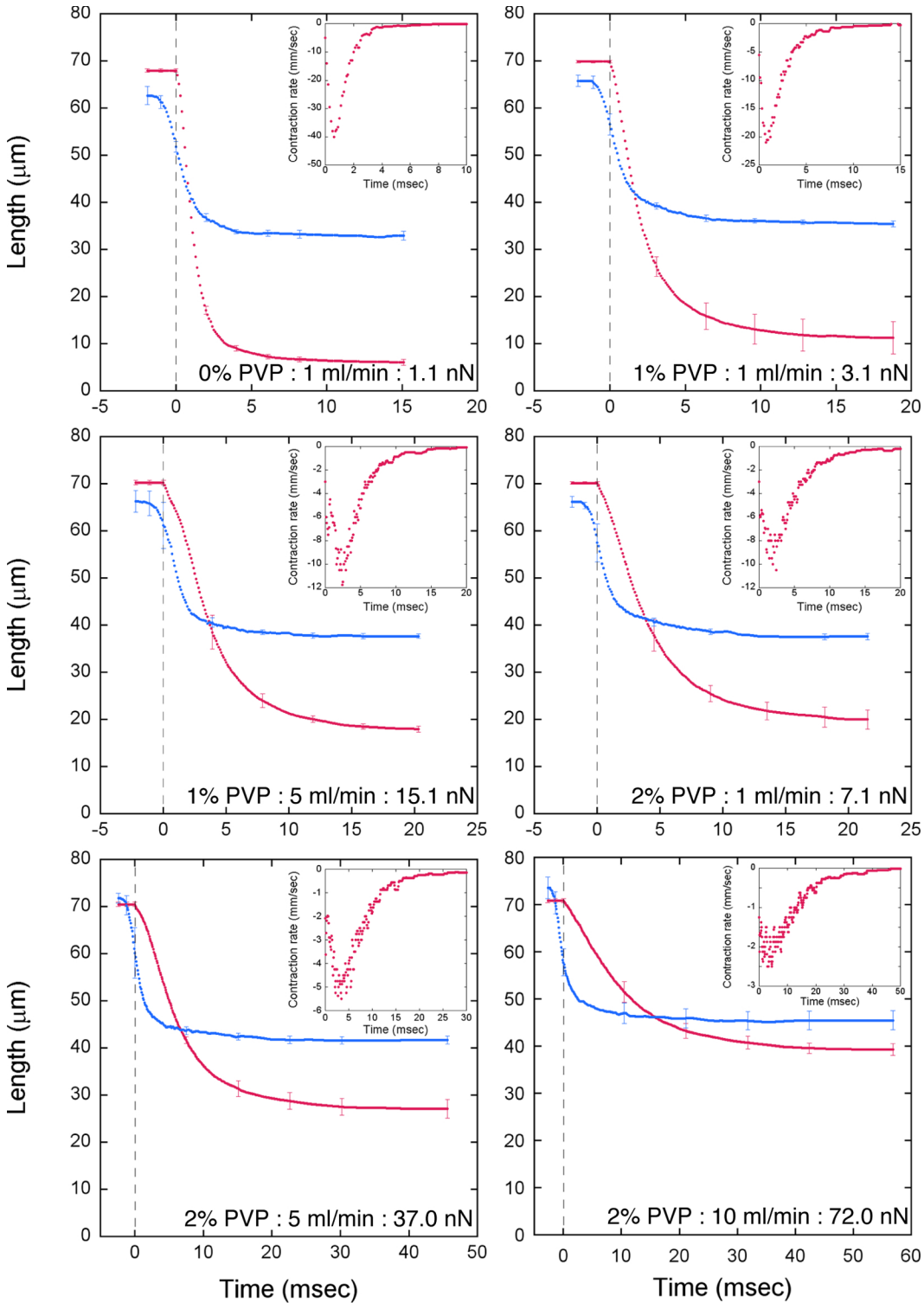

Figure 6-3: Time courses of the stalk length, the zooid length and the contraction rate in different loading conditions. The caption of each plot shows the medium PVP concentration, channel flow rate and averaged stall force on the zooid at the end of contraction. Red dot - the stalk length, blue dot - the zooid length, error bar - standard deviation and inset - contraction rate.

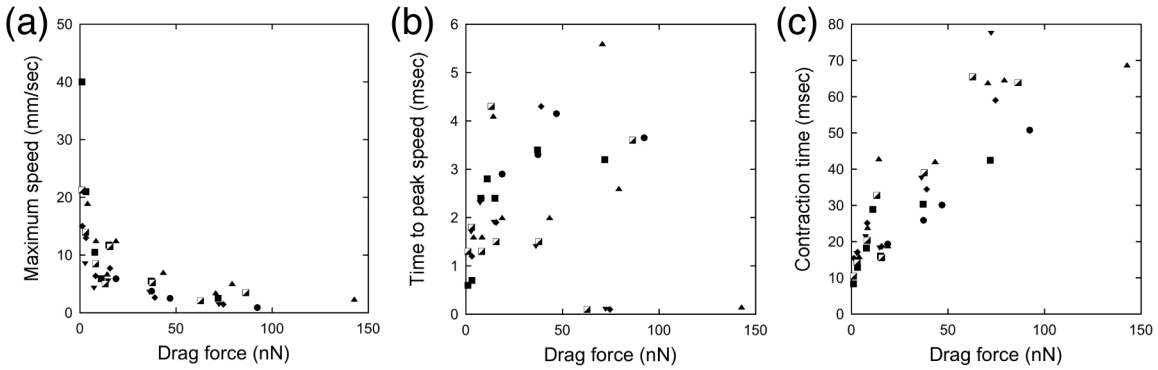

Figure 6-4: Key dynamics parameters of stalled contraction: (a) The maximum contraction speed. (b) The time to the maximum contraction speed. (c) The contraction time. Data were obtained from six cells including the one for Figure 6-3. The drag force shown is the stall force on the zooid estimated at the end of contraction.

6.3.2 Stalk/zooid length and contraction rate

Figure 6-3 compares time courses of the stalk and zooid length of a *Vorticella* cell in different flow conditions. As the stall force increases, the stalk contracts over shorter distance, i.e., the length of the coiled stalk increases, taking a longer time. The length of the relaxed stalk also increases, but this may be because the zooid becomes slenderer (increasing aspect ratio shown in Section 6.3.1) as the stall force increases. With the constant stalk length, the smaller zooid radius leads to the increased length of the projected stalk according to Eq. 5.8. However, it cannot be ignored that the stall force may elongate the stalk. As already shown in Section 6.3.1, the zooid is also affected by the stall force. In the relaxed state, the zooid is more elongated by the stall force compared to the stalk, but the shrunken zooid is less affected compared to the coiled stalk.

The longer contraction time and shorter contraction distance imply the lower contraction speed. The insets of Figure 6-3 show that the peak contraction rate decreases in the magnitude as the stall force increases. In addition, Figure 6-4 shows three key parameters of *Vorticella*'s contraction dynamics as a function of the drag force due to the viscous fluid flow: the maximum contraction speed ($|\dot{S}|_{\max}$), the time to the maximum contraction speed ($\tau_{\max}$), and the contraction time (τ_c). As expected,

the maximum contraction speed decreases and the contraction time increase with the increasing stall force, which is similar to *Vorticella* contracting in the passive load, i.e., the drag force from the stagnant viscous medium. However, the time to the peak contraction rate increases as the stall force increases whereas that measured in stagnant viscous media is rather constant as shown in Table 3.1. In some cases of the high stall force, *Vorticella* reaches its maximum contraction rate at the beginning of contraction and slowly drags the body with the decreasing contraction speed (almost zero $\tau_{\max}$ shown in Figure 6-4(b)).

6.3.3 Energetics of stalled contraction

The drag force shown so far is the drag force on the contracted zooid estimated at the end of contraction, and its magnitude is used to estimate the isometric force of the *Vorticella* stalk. However, in discussing the energetics of *Vorticella*'s stalled contraction, it should be considered the drag force that the zooid experiences while moving in Poiseuille flow. For this purpose, the zooid of *Vorticella* contracting in Poiseuille flow is assumed to be a non-rotating solid sphere translating in the opposite direction to the stream in the channel as Figure 6-5 shows.

As discussed in Section 3.1, it should be decided whether flow around the moving zooid is viscous dominated or not. As a representative case, let's examine *Vorticella* contracting in 1% PVP solution flowing at 1 ml/min. In this case, typical values of the maximum contraction rate, the time to the maximum contraction rate and the zooid radius are 20 mm/sec, 1 msec and 20 μm, respectively (chosen from Section 6.3.2). The Stokes number calculated with Eq. 3.3 is about 0.6. Instead of the shear Reynolds number defined as Eq. 5.13, the maximum particle Reynolds number is defined with the maximum contraction rate and the unperturbed flow velocity at the center of the zooid ($V_c = V|_{y=0,\ z=R-h}$ from Eq. 5.3, see also Figure 6-5) as the following:

$$\mathrm{Re}_{\max} = \frac{2\rho R(V_c + |\dot{S}|_{\max})}{\mu} \tag{6.2}$$

Because V_c is about 2.5 mm/sec, the maximum Reynolds number is 0.3. As the

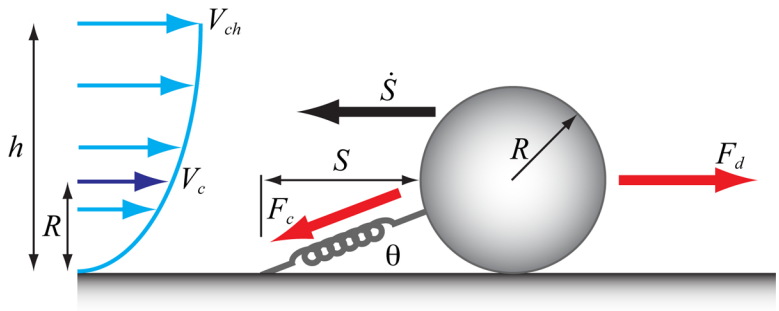

Figure 6-5: A diagram of the zooid translating in Poiseuille flow. $\dot{S}$ is the contraction rate component parallel to the channel bottom, and V_c is the unperturbed flow velocity at the zooid center.

flow rate increases from 1 ml/min to 5 ml/min in the case of 1% PVP solution, V_c increases, so $\mathrm{Re}_{\max}$ may also increase. However, the above Reynolds number does not increase due to the decreasing contraction rate. Increasing medium viscosity decrease the Reynolds number and Stokes number. Therefore, for the cases of interest, the flow around the moving zooid can be regarded steady and viscous dominated, i.e., the creeping flow. Because any results obtained with water flow do not satisfy the above conditions, they are not included in this energetics estimation.

Because flow around translating zooid is in the Stokes regime, the viscous drag force on the zooid is divided into two components as the following:

$$F_d = F_d^t + F_d^p = 6\pi\mu R|\dot{S}|F^t + 6\pi\mu R V_{ch} F^p \tag{6.3}$$

where F_d^t is the drag force due to the zooid's translational motion, and F^t is the translational drag force correction factor taking into account the wall effect from the channel's top and bottom surface [93]. F^t is given as

$$F^t = -\frac{8}{15}\ln\left(\frac{\delta_{\mathrm{LW}}}{R}\right) - \frac{8}{15}\ln\left(\frac{\delta_{\mathrm{UW}}}{R}\right) + \Delta F^t \tag{6.4}$$

where δ_{LW} is the gap between the zooid and the channel's lower surface, δ_{UW} is the gap between the zooid and the channel's upper surface, and ΔF^t is the correction factor for the infinitesimal gap between the zooid and the channel surface [93]. Values

of ΔF^t are summarized in Table 5.1 as a function of R/h, and in this study, a curve fitted against those values near $R/h = 1$ is used:

$$\Delta F^t = 1.33\Big(\frac{R}{h}\Big)^{-0.278}. \tag{6.5}$$

On the other hand, F_d^p is the drag force that Poiseuille flow exerts on the zooid, and it is already introduced with F^p in Eq. 5.11 and 5.12. Because the zooid does not rotate during contraction, the drag force component due to rotation is not included.

To determine which component of Eq. 6.3 is dominant for stalled *Vorticella*, the order of magnitude of the correction factors are compared in the representative case (1% PVP solution flowing at 1 ml/min). Because Eq. 6.4 has a singularity as $\delta_{\mathrm{LW}} \to 0$, which is the case of the zooid contacting the surface, it is assumed that the gap between the zooid and the channel's lower surface is $\frac{1}{100}$ of the zooid radius, i.e., $\delta_{\mathrm{LW}} = 0.01R$.[14] Because δ_{UW} is $2h - 2R$ and ΔF^t is 2.51 (when $R/h = 0.1$ in Table 5.1), F^t is 3.42 and F^p is 0.32. Then, a ratio of the translation drag component to the Poiseuille drag component becomes

$$\frac{F_d^t}{F_d^p} = \frac{|\dot{S}|F^t}{V_{ch}F^p} = \frac{0.02 \times 3.42}{0.013 \times 0.32} \approx 16. \tag{6.6}$$

Therefore, in estimating the energetics of stalled contraction, the drag force due to the zooid motion must be considered.

With the contraction rate shown in Figure 6-3, the drag force on the moving zooid is estimated with Eq. 6.3, and Figure 6-6(a) shows the maximum drag force on the zooid as a function of the drag force on the zooid at the end of contraction (same as F_d^p). The maximum drag force appears to increase as the stall force increases especially when the stall force is greater than 30∼50 nN. Instantaneous work done by the spasmoneme to overcome the viscous drag force is given as

$$W = F_c \Delta S \cos\theta = F_d \Delta S \tag{6.7}$$

[14]This assumption of the infinitesimal gap ignores the friction force on the zooid.

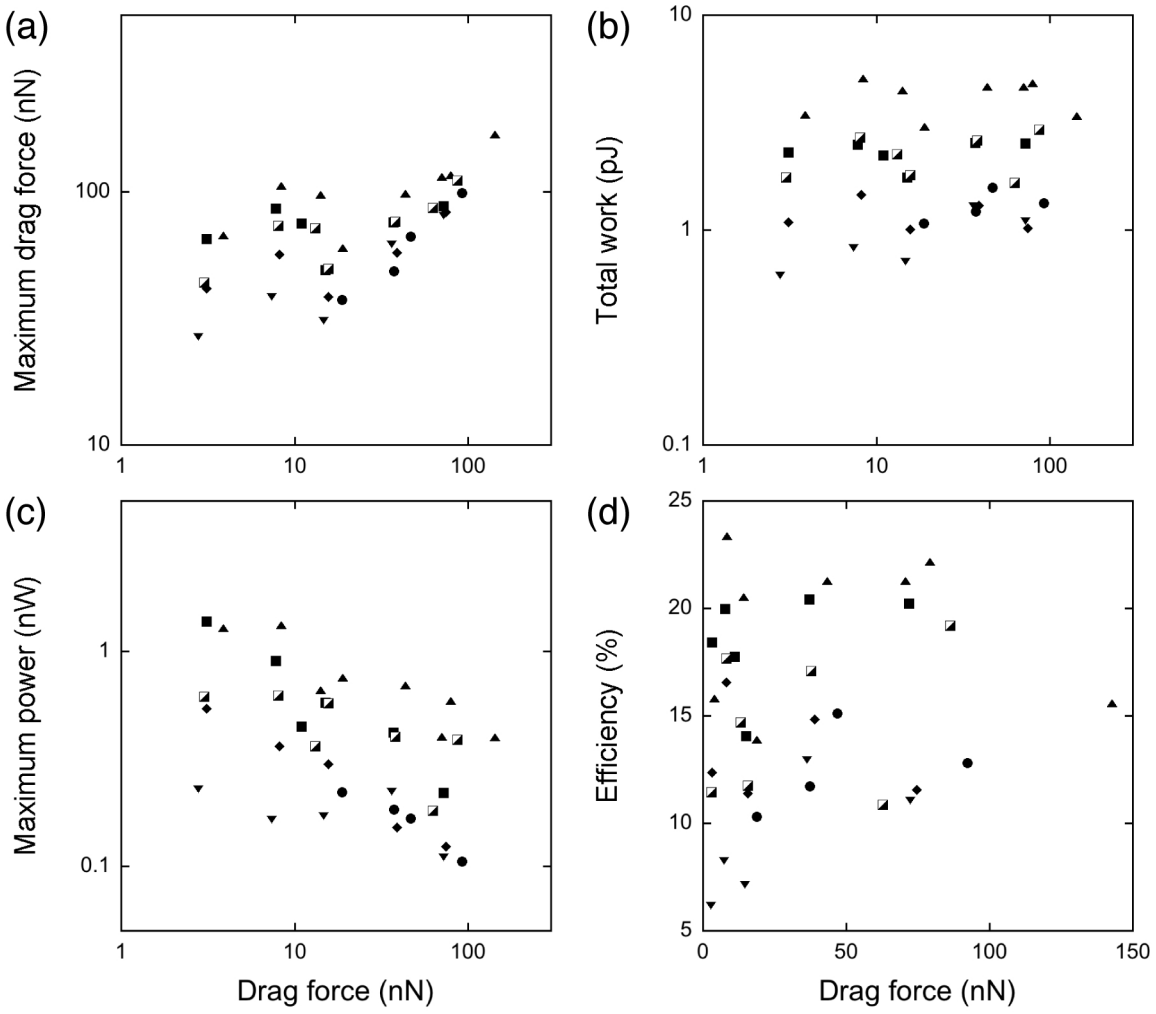

Figure 6-6: Key energetics parameters of stalled contraction: (a) The maximum drag force on the zooid. (b) The total work done by the zooid. (c) The maximum power output. (d) The efficiency of the spasmoneme. Data were obtained from six cells including the one for Figure 6-3. The drag force shown is the stall force on the zooid estimated at the end of contraction.

where ΔS is the decrement in the projected length of the stalk, and the total work done is

$$W_{\mathrm{tot}} = \int_0^{\tau_c} F_d |\dot{S}| dt. \tag{6.8}$$

Here, the friction force due to the zooid-surface contact is ignored. Another key energetics parameter is the maximum power output of stalled *Vorticella*, which is given as

$$P_{\max} = |F_d \dot{S}|_{\max}. \tag{6.9}$$

Upadhyaya et al. suggested that the maximum power output of *Vorticella* does not depend on the medium viscosity in the case of contraction in a stagnant medium [104], and in Section 3.4.3, I confirmed this power-limitedness with the CFD simulation and showed that the cell works more in a more viscous medium. However, *Vorticella* contracting in Poiseuille flow behaves differently. As Figure 6-6(b) and (c) show, the total work done is rather constant irrespective of the stall force, and the maximum power output decreases as the stall force increases. Therefore, the stalk contraction of *Vorticella* is work-limited in the active loading condition, and this suggests that the total amount of energy from calcium binding is a limiting factor.

As calculated in Section 3.4.3, the efficiency of the spasmoneme was calculated for stalled contraction. Because the total energy available from calcium binding linearly depends on the stalk length, the efficiency can be regarded as the total work normalized with the stalk length. The efficiency of the spasmoneme does not show noticeable dependence on the stall force. The maximum efficiency achieved is lower than 25%, and it is a little higher than the maximum efficiency estimated with the CFD simulation in the passive loading condition (18.5% in Table 3.4). Because in estimating energetics it is not considered energy to overcome the friction force on the zooid and to deform the stalk, the efficiency of the the spasmoneme should be greater than the current estimation.

Similar to the efficiency, the specific power is the power output normalized with the relaxed stalk length because the specific power is the power output divided by the wet mass of the spasmoneme. Although not shown in Figure 6-6, the maximum

specific power of the six stalled *Vorticella* cells decreases with the increasing stall force as the maximum power output does, and its range is 1.00∼10.94 W/g.

6.3.4 Propagation speed of stalk coiling

Upadhyaya et al. measured that the propagation of stalk coiling was not affected by the medium viscosity, and they argued that this constant propagation speed is because a related contraction-triggering signal is inherent [104]. Because *Vorticella* behaves differently depending on the type of resistance, this constant propagation speed of stalk coiling should be confirmed for *Vorticella* contracting in viscous fluid flow.

Figure 6-7 shows an example of measuring the propagation speed of stalk coiling. This speed measurement requires tracking at least two points along the stalk. The *Vorticella* cell shown in the left image has a few beads on the stalk close to one another, and one of them (marked by the blue arrow) is chosen for the speed measurement. Because the cell does not have any beads close to the zooid, the zooid-stalk junction is chosen instead (marked by the red arrow). The right kymographs show sequential images of the contracting stalk in different flow conditions, and colored lines indicate how long points of interest do not move. From these kymographs, the distance between two points (L_b) and the time difference between their motion initiation (t_s) are measured, and then the propagation speed is calculated ($V_p = L_b/t_s$).

As Figure 6-8 shows, the averaged propagation speed appears constant regardless of the stall force. Although there is a little decrease in the propagation speed as the stall force increases, the amount of decrease is negligible considering that the stall force increases to more than one order of magnitude. Therefore, the propagation of stalk coiling seems not be affected by the stall force as Upadhyaya et al. observed [104]. However, the low contraction propagation speed (L_b = 12 mm case) may indicate that the cell was fatigued by the stall force because Sugi measured that the propagation speed of a fatigued *Carchesium* cell is about 3 cm/sec (at minimum) in contrast to about 20 cm/sec of healthy one (at maximum) [96].

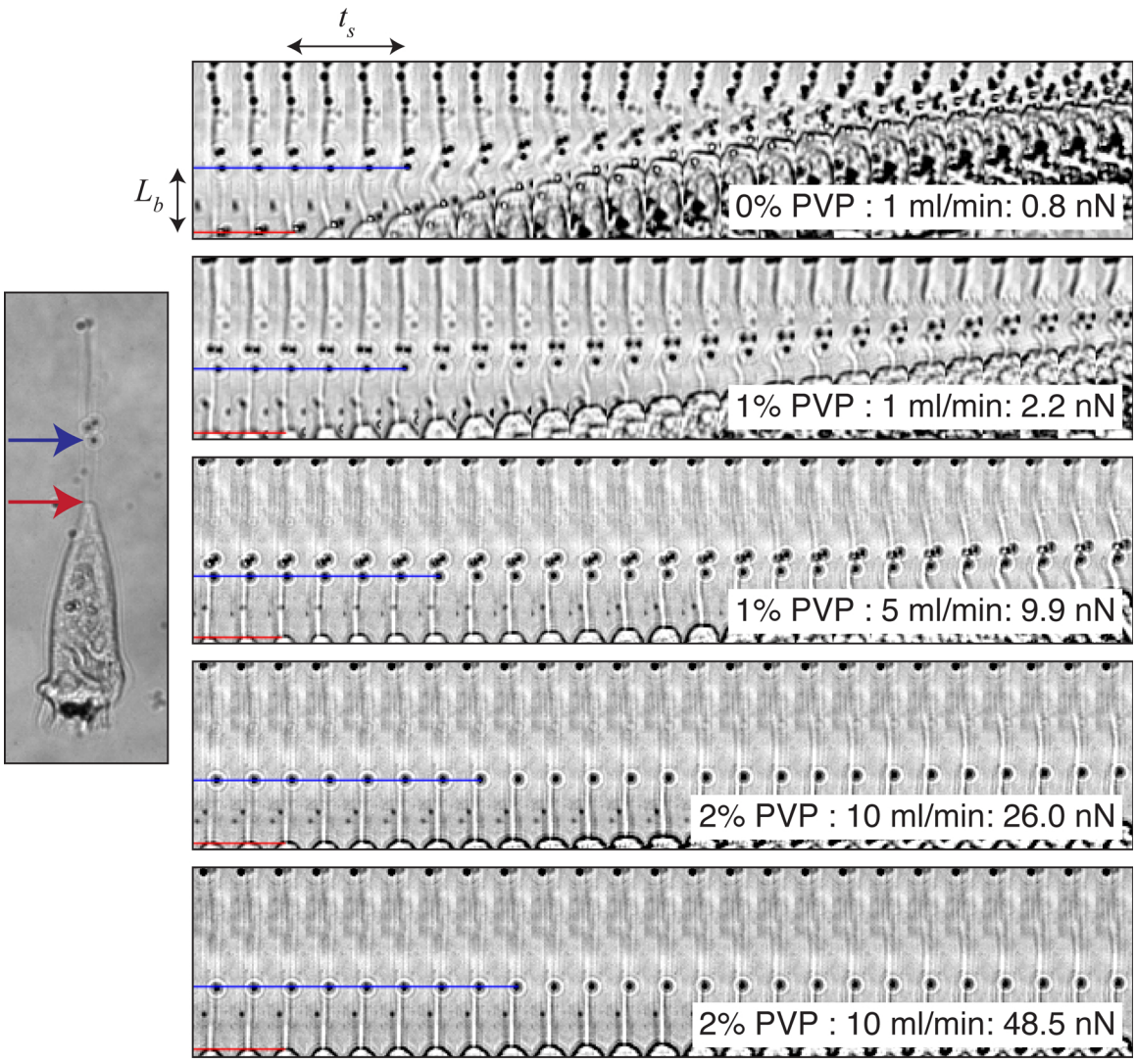

Figure 6-7: Kymographs of contracting *Vorticella convallaria*: L_b is the distance between two points on the stalk (the beads or the bead and the zooid-stalk junction), and t_s is the time difference in the initial motion between the two points. Information on flow condition is shown at a corner of each kymograph in the order of the PVP concentration, flow rate and drag force on the contracted zooid.

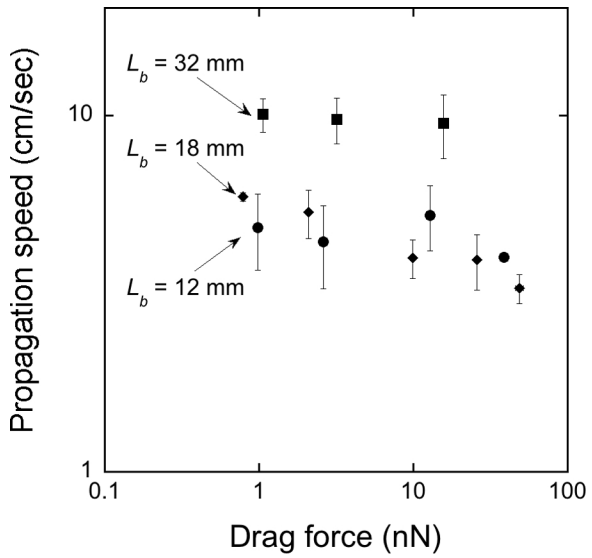

Figure 6-8: The propagation speed of stalk coiling: The speed is averaged over 4∼5 contractions, and error bars show standard deviation. The distance between two points on the stalk is also shown. The drag force shown is the stall force on the zooid estimated at the end of contraction.

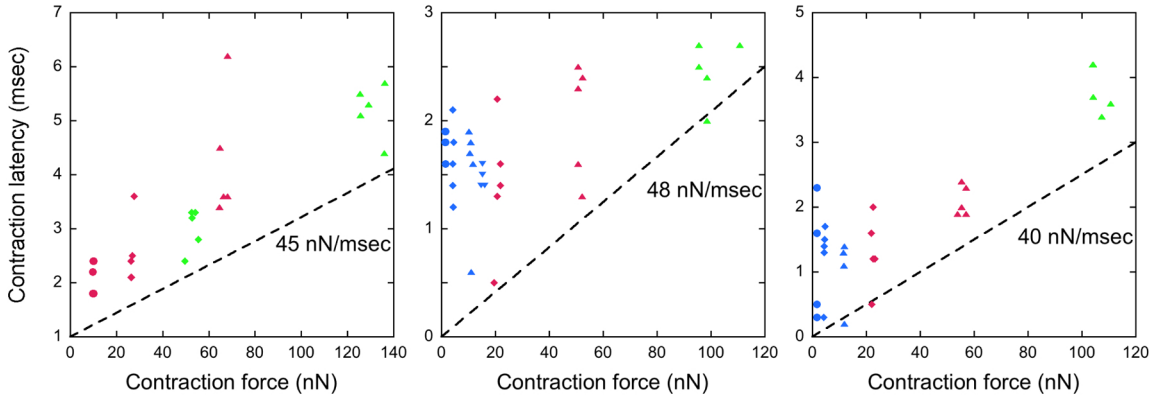

Figure 6-9: Contraction latency measured from three cells. The dashed line shows an approximated limit for the minimum contraction latency. ● - 0% PVP, ♦ - 1% PVP, ▲ - 2% PVP, ▼ - 3% PVP, blue - 1 ml/min, red - 5 ml/min and green - 10 ml/min.

6.3.5 Contraction latency and force developing rate

In Figure 6-3, the zooid contraction seems to take rather constant time regardless of the stall force whereas the stalk contraction takes longer time. Furthermore, when the stalk begins coiling ($t = 0$ msec), the zooid seems to have contracted more as the stall force increases. In normal contraction, the zooid usually leads the stalk in contraction, so there is a latency between the zooid contraction and stalk contraction. Ueda measured that the latent period of *Carchesium* was 1∼4 msec [103], but Sugi observed a wide variation in the contraction latency from a healthy single cell [96]. This contraction latency is related to the stalk coiling propagation. In contrast, in the case of *Vorticella* contracting in viscous Poiseuille flow, the contraction latency increases as the stall force increases.

Because the propagation of a contraction-activating signal is not affected by the stall force and because the propagation speed is much faster than the contraction rate of the stalk, it is reasonable to assume that the spasmoneme will be fully activated right after the zooid contraction. Then, this prolonged latency suggests that, as the drag force applied to the shrinking or shrunken zooid increases, it takes the *Vorticella* stalk longer time to develop the contraction force great enough to overcome the drag force and then to begin coiling. According to this hypothesis, it is possible to measure the rate at which the spasmoneme develops its contraction force by measuring the contraction latency and stall force.

Figure 6-9 shows three cases of contraction latency measurement. Although there is variation in the latency at a certain flow condition, there is a minimum latency for the flow condition, and this minimum latency increases as the contraction force increases. In this case, the contraction force is the force that the stalk develops at the beginning of the stalk coiling. The dashed lines of Figure 6-9 indicate a limit to under which the contraction latency cannot decrease. In other words, with the given maximum contraction force developing rate, the contraction latency should be longer than the value from the dashed line at a certain magnitude of the stall force. Because the slope of the dashed line has the dimension of msec/nN, its reciprocal is

the maximum contraction force developing rate. Figure 6-9 shows that the rate is approximately 40∼50 nN/msec.

6.4 Discussion

6.4.1 Limitations of the microfluidic channel platform

A disadvantage of using the microfluidic channel is that the zooid may contact the channel surface. In estimating the contraction force and energetics of stalled *Vorticella*, the friction force on the zooid is not considered. From Figure 5-8, the friction force can be expressed with

$$F_f = \mu_f(F_c \sin\theta - F_l) \tag{6.10}$$

where μ_f is the friction coefficient between the zooid and channel surface. There are two problems in estimating this friction force: the friction coefficient is unknown, and it is also unknown whether the zooid is always in contact with the channel surface during contraction. In addition, instead of ignoring the friction force, I assumed arbitrarily that the spacing between the zooid and the channel's lower wall is $\frac{1}{100}$ of the zooid radius in calculating the translational drag correction factor. Therefore, it can be said that the current estimates are conservative, but the total work and maximum power output are in the same order of magnitude as the CFD-based estimates.

This contact problem may be overcome with a specially designed microfluidic channel that has columns for *Vorticella*'s residence. Horizontal columns lying in the channel's horizontal symmetry plane ($z = 0$ plane in Figure 5-3) are ideal because *Vorticella* cells on the column do not experience the torque. However, it is hard to control where *Vorticella* attaches inside the channel. I tried a PDMS channel with vertical columns, but *Vorticella* randomly resided. Increasing the size or number of columns will increase the possibility for *Vorticella* to find the column, but it will complicate flow condition inside the channel and augment fluid dynamic interaction between cells and columns.

6.4.2 Relaxation of stalled *Vorticella*

When it comes to the relaxation of *Vorticella* under the stall force, it was expected to take shorter time because the stall force always pulls the zooid in the direction of relaxation. On the contrary to this expectation, however, relaxation time seems to increase as the stall force increases. The same observation was made by Rahat et al. and France [27, 77].

This prolonged relaxation seems to be because the spasmoneme still maintains its contractile force during relaxation. When the flow inside the microchannel is turned off at the end of contraction or at the beginning of relaxation in high stall force conditions, the stalk resumes contraction as the stall force vanishes. Rahat et al. also suspected that the prolonged relaxation under the load may be due to slow decay of the active state of the spasmoneme [77]. In contrast to normal relaxation of which the driving force is the elastic restoring force of the sheath, the driving force for the relaxation of stalled *Vorticella* seems to be the stall force itself, so the cell is forced to relax its stalk. With the resistance to relaxation, which is the remnant contractile force of the spasmoneme, the relaxation takes longer time as the stall force increases.

On the other hand, under a very high stall force condition such as 10 ml/min flow of 3% PVP solution, *Vorticella* repeated contraction before it completed relaxation. Although it is not clear why this repeated contraction happens, the zooid seems to signal the stalk to contract, stimulated by the stall force in the middle of slow relaxation. Calcium ion might be released repeatedly after being pumped back to its storage sites during relaxation. In other words, the contraction-initiating machinery of the zooid is reset and fires the signal while the contraction machinery of the spasmoneme is being reset.

6.4.3 Stalled contraction summary

Figure 6-10 summarizes the effect of the stall force on the stalk contraction of *Vorticella convallaria* by comparing time courses of the contractile force in cases of normal contraction and stalled contraction. Because the spasmoneme needs more time to

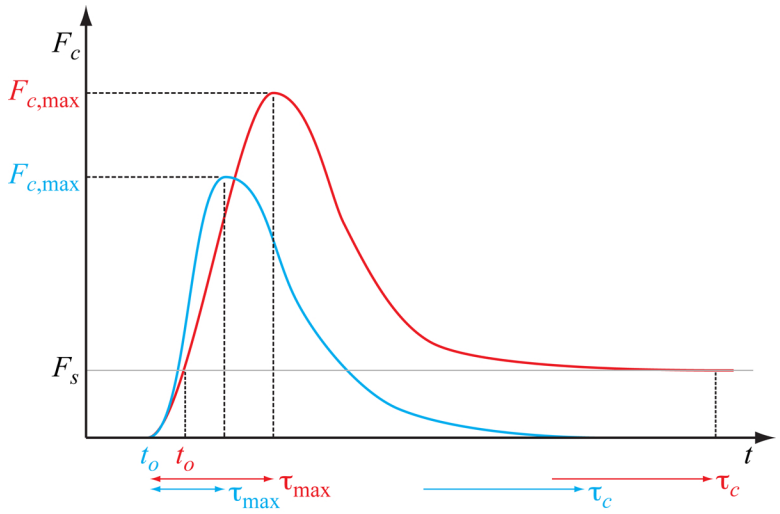

Figure 6-10: A comparison between normal contraction and stalled contraction in terms of contractile force development: Blue curve - normal contraction, red curve - stalled contraction. F_s is the stall force, and t_o indicates the time when the stalk begins to shorten. The origin of the time coordinate indicates the time when the zooid begins to contract.

develop the contraction force great enough to overcome the drag force on the zooid (which is the stall force, F_s), the stalk begins shortening after longer time has elapsed since the zooid contraction (increased t_o). This means that the contraction latency increases as the stall force increases. In addition, the time to the peak contraction force ($\tau_{\max}$) and the contraction time (τ_c) also increase. The spasmoneme generates the greater peak contractile force ($F_{c,\max}$) as the stall force increases. In the case of normal contraction, the spasmoneme retains the contractile force to keep the stalk deformed at the end of contraction. In addition to this force, the spasmoneme maintains more force balanced by the stall force when the stall force is applied. Although the cell generates the contraction force more in stalled contraction, the total work done by the cell is constant because of the decreased contraction distance.

THIS PAGE INTENTIONALLY LEFT BLANK

Chapter 7

Conclusion

7.1 Summary

A microorganism *Vorticella convallaria* is extraordinary in terms of fluid dynamics and cell motility. From a fluid dynamic perspective, water flow induced by contracting *Vorticella* lies on the border between the viscous dominated regime and inertia dominated regime whereas most microorganisms live in the low Reynolds number world. In addition, the contraction-induced flow has a nearby no-slip wall boundary, which makes the flow more complicated. In contrast to other cell movements, on the other hand, the stalk contraction of *Vorticella* relies on neither the acto-myosin mechanism nor the microtubule-dynein/kinesin mechanism. Not consuming energy from ATP for contraction, the stalk has a unique mechanochemical Ca^{2+}-dependent engine called the spasmoneme. This spasmoneme holds a promise as a candidate for bio-inspired actuators because of its contraction speed ($\sim$5 cm/sec), contractile force ($\sim$100 nN) and power ($\sim$4 W/g).

This thesis presented evaluations of the contraction force generated by the spasmoneme of *Vorticella convallaria* and analyses of the dynamics and energetics of the contraction. The lower limit of the contractile force is the peak contraction force that the stalk develops during normal contraction. Stokes' law has been used to evaluate the lower limit, but I showed with fluid dynamic analysis and flow visualization that water flow induced by *Vorticella*'s contraction does not satisfy approximations for

Stokes' law because the flow is not only unsteady and non-creeping but also affected by the substrate. Therefore, instead of using Stokes' law or any relevant analytic drag formulae, I employed computational fluid dynamic simulations to consider simultaneously the effect of the unsteadiness, the finite Reynolds number and the substrate in contraction force estimation. Simulation-based force estimates revealed that this combined effect comprises about 35% of the total force in the case of contraction in water, and that the effect of the unsteadiness and finite Reynolds numbers is dominant in the early contraction phase whereas the wall effect of the substrate is important in the later phase. However, as the medium viscosity increases, the transient/convective inertia becomes negligible whereas the wall effect remains. Estimated energetics show that the work done in the early contraction phase and the maximum power output are similar regardless of the medium viscosity. This suggests that, during the force developing phase, *Vorticella* uses a common mechanism to perform mechanical work irrespective of viscous loading conditions and that the cell adjusts its stalk contraction behavior according to viscous environment. However, I pointed out that *Vorticella* may show this power-limitedness only for passive loadings.

The upper limit of the contractile force is the isometric force that the spasmoneme develops while it cannot shorten at all due to an external resistance. I applied viscous drag force to the zooid with a microfluidic channel to stall the contraction of *Vorticella* and developed a model to estimate the isometric force from the dimension of the stalled cell and flow conditions. This method enables to control the magnitude of the stall force and to observe several contractions of a single cell under different stall force conditions. As the stall force increases, the cell contracts over shorter distance with lower contraction speed and longer contraction time. The estimated isometric force is in the order of 100 nN, and it linearly depends on the relaxed stalk length. This stalk length dependence suggests that 1 μm of the spasmoneme can generate the contractile force up to about 2.5 nN, and it enables estimating the contractile force per the spasmonemal filament. On the other hand, as the stall force increases, it takes the stalk longer time to begin coiling after the zooid has begun contraction. This increased contraction latency suggests that the *Vorticella*

stalk needs longer time to develop the contraction force great enough to overcome the increasing stall force. By measuring the contraction latency and stall force, I estimated that the maximum contraction force developing rate of the spasmoneme is about 40∼50 nN/msec. Finally, the energetics of stalled contraction revealed that *Vorticella* in viscous fluid flow behaves differently than the cell does in stagnant viscous media: the total work is constant regardless of the stall force whereas the maximum power output decreases as the stall force increases.

7.2 Future work: in vitro contraction assay

Among possible research projects related to this thesis (some of them are mentioned in related chapters), I would especially like to propose an idea about in vitro reconstruction of the centrin-based contraction mechanism. Because it is still unknown how spasmin and spaconnectin interact and form a filament, it may be possible to reconstruct contractile filaments with centrin and melittin. Melittin is a peptide extracted from honey bee venom, and one molecule of centrin binds to a molecule of melittin [23]. An advantage of using melittin instead of Sfi1p is that melittin is commercially available and can be synthesized.

The main feature of models suggested for the centrin-based motility is the Ca^{2+}-dependent conformation change of filaments containing pairs of centrin and centrin binding partner. It was suggested to form a filament by concatenating melittin peptides, but this approach may have limitations due to the amino acid sequence of melittin (James Tam, personal communication). Instead, I suggest using a filamentous bacteriophage M13 as the backbone of the filament. It seems possible to express on the surface of M13 binding sites for melittin molecules to which a few amino acids are added for binding (Yoonsung Nam, personal communication). According to this idea, the filament consists of one M13 bacteriophage, multiple melittin molecules binding to the bacteriophage and centrin molecules binding to melittin.

Various imaging techniques can be employed to confirm the binding of peptides to the backbone and the conformation change of the filament responding to change

in free calcium ion concentration. On the other hand, the conformation change of the filament can be measured by stretching the filament with the optical tweezer [46]. If the filament shortens responding to increase in free calcium ion concentration, its persistence length will decrease, which is expected to be measured with the optical tweezer. The optical tweezer will also enable measuring the isometric force of the filament, which can be compared to one of main results of this thesis.

Appendix A

Preliminary CFD simulation

To test possible moving mesh methods for the CFD simulation, I created two cases of two-dimensional axial symmetric mesh with triangular elements as shown in Figure A-1. The axisymmetry condition is assigned to boundary ① and ④. The no-slip wall condition is assigned to boundary ⑤ representing the substrate, and the moving wall condition to boundary ② and ③ corresponding to the sphere. In other words, boundary ② and ③ are set to move according to velocity defined as

$$U = -66.186t^{0.969}\exp\Big(\frac{t^{1.969}}{-2.914\times10^{-6}}\Big) \tag{A.1}$$

where t is time in sec, and U is velocity in m/sec. In Mesh 2, the domain is split to two subdomains, and boundary ⑨, the border between the subdomains, moves along with the sphere at the same speed. To reduce deformation of elements, we set boundary ① and ④ of Mesh 1 and boundary ①, ④, ⑥ and ⑦ of Mesh 2 to shorten or lengthen linearly based on the curve parameter `s` corresponding to the sphere's movement.

Because the simple model is axial symmetric, the continuity equation and the Navier-Stokes equation in the cylindrical coordinate system for incompressible flow are the governing equations to be solved. They are given as

$$\frac{1}{r}\frac{\partial \rho u_r}{\partial r} + \frac{\partial u_z}{\partial z} = 0 \tag{A.2}$$

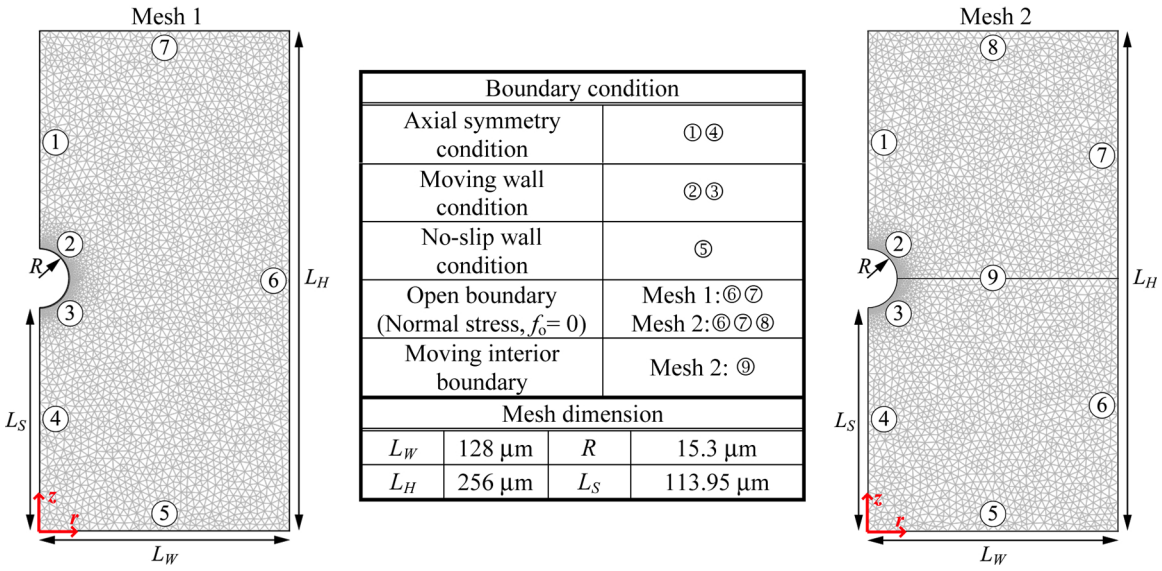

Boundary condition	
Axial symmetry condition	①④
Moving wall condition	②③
No-slip wall condition	⑤
Open boundary (Normal stress, f_o= 0)	Mesh 1:⑥⑦ Mesh 2:⑥⑦⑧
Moving interior boundary	Mesh 2: ⑨

Mesh dimension			
L_W	128 μm	R	15.3 μm
L_H	256 μm	L_S	113.95 μm

Figure A-1: CFD models for preliminary simulations and assigned boundary conditions.

and

$$\rho\left(\frac{\partial u_r}{\partial t}+u_r\frac{\partial u_r}{\partial r}+u_z\frac{\partial u_r}{\partial z}\right)=-\frac{\partial p}{\partial r}+\mu\left[\frac{1}{r}\frac{\partial}{\partial r}\left(r\frac{\partial u_r}{\partial r}\right)+\frac{\partial^2 u_r}{\partial z^2}-\frac{u_r}{r^2}\right]$$
$$\rho\left(\frac{\partial u_z}{\partial t}+u_r\frac{\partial u_z}{\partial r}+u_z\frac{\partial u_z}{\partial z}\right)=-\frac{\partial p}{\partial z}+\mu\left[\frac{1}{r}\frac{\partial}{\partial r}\left(r\frac{\partial u_z}{\partial r}\right)+\frac{\partial^2 u_z}{\partial z^2}\right] \tag{A.3}$$

where u_r and u_z are flow velocity in the r and z direction, respectively. Using COMSOL Multiphysics, I combined the transient analysis solver of the incompressible Navier-Stokes equation and the transient analysis solver of ALE (Arbitrary Lagrangian-Eulerian) moving mesh mode. The drag force on the sphere was calculated by integrating the total z-direction force over the spheres boundaries using postint(fem, '2ϕR(T_z_ns)').

Because the quality of the mesh is critical in CFD simulations, I tried three moving mesh methods as Figure A-2 shows. The first case using Mesh 1 does not have any special treatment for deformed elements, so elements around the sphere are expected to undergo severe deformation. The second case also employs Mesh 1, but it is different in that the mesh is automatically remeshed with the same element size

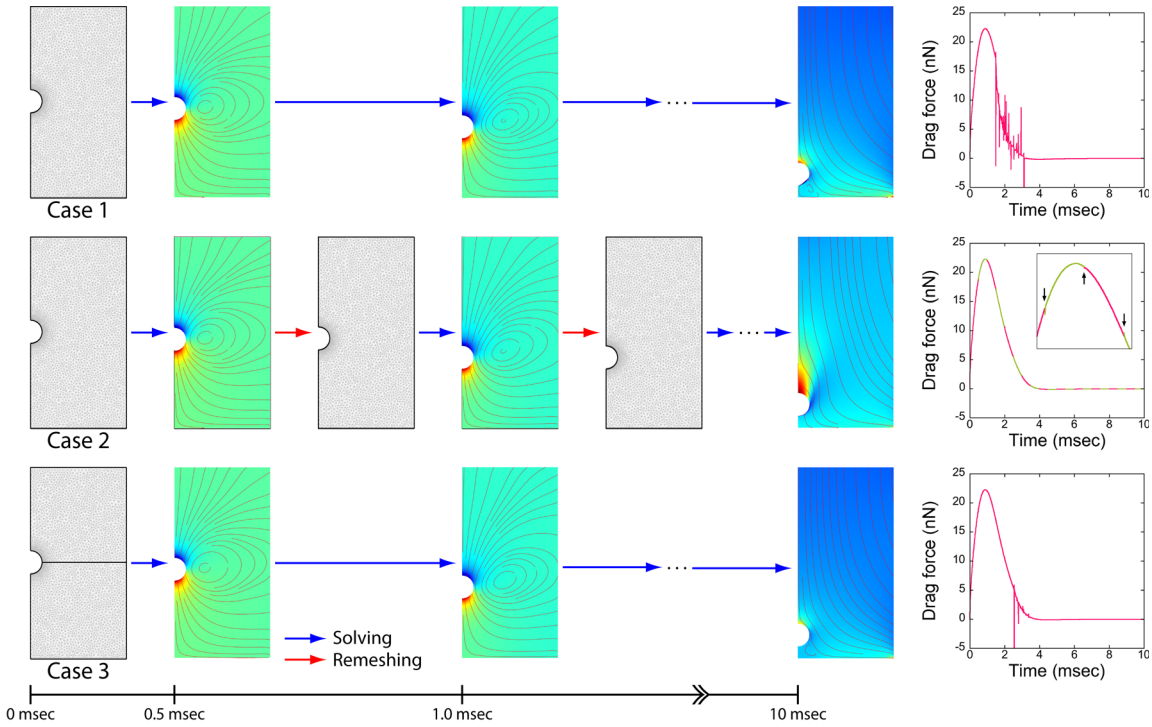

Figure A-2: Three methods of moving mesh and their drag force calculation results.

every 0.5 msec. The last time step solution of the old mesh is mapped to the new one as the initial condition, and then solving is resumed. The final case uses Mesh 2 that has the moving interior boundary. Elements of the top and bottom subdomain are elongated and compressed in the z-direction, respectively. In all cases, flow was simulated for 10 msec with a time step of 0.01 msec.

Figure A-2 shows drag force calculation results with pressure distribution and streamlines at 0.5, 1.0 and 10 msec. In Case 1, inverted elements first appeared at 1.48 msec, and they are found near the stagnation point of the sphere. Severely deformed elements seem to have caused fluctuations in the drag force calculation. In contrast, Case 2 did not show any inverted elements owing to automatic remeshing, and its drag force calculation result is reasonable. However, the Case 2 result shows discontinuities at every time step when remeshing was done (arrows in the inset). Solution mapping seems to have caused these discontinuities. Even in Case 3, which was designed to minimize element deformation without remeshing, inverted elements were unavoidable because the final gap distance is small ($L_s \approx R$). Although some

elements started to be reversed at 2.55 msec in Case 3, the moving interior boundary helped reducing severe deformation of elements. Therefore, the moving interior boundaries are adopted in the model shown in Section 3.2.

Appendix B

Forces on a sphere fixed in shear flow

In the stall experiment using the microfluidic channel, the contracted zooid of *Vorticella* is modeled to be a solid sphere fixed on the channel surface in Poiseuille flow. Estimating the stalk's contraction force requires to know forces on the zooid in Poiseuille flow. Here, I briefly summarize previous relevant studies about the drag force and torque on a sphere in shear flow.

B.1 Couette flow

When it comes to a sphere located in Couette flow, there have been many studies in the low Reynolds number regime. By applying the bipolar coordinate system to solve Stokes equations, Goldman et al. obtained an exact solution of the motion of a neutrally buoyant solid sphere in Couette flow [31]. Based on the solution, they expressed the shear-induced drag force and torque on an immobilized sphere as the following:

$$\begin{aligned} F_d &= 6\pi\mu RH\dot{\gamma}F^s \\ T &= 4\pi\mu R^3\dot{\gamma}T^s \end{aligned} \tag{B.1}$$

where H is the distance from the sphere center to the plane wall, $\dot{\gamma}$ is the shear rate of Couette flow, and F^s and T^s are correction factors of the drag force and torque for Couette flow, respectively. Goldman et al. calculated values of these correction factors in a function of H/R, and for the limiting case of $H/R = 1$ in which the sphere contacts the wall, F^s becomes 1.7005 and T^s becomes 0.9440. They also suggested asymptotic forms of the correction factors based on the method of reflections as the following:

$$\begin{aligned} F^s &\approx 1 + \frac{9}{16}\frac{R}{H} \\ T^s &\approx 1 - \frac{3}{16}\Big(\frac{R}{H}\Big)^3. \end{aligned} \tag{B.2}$$

These formulas are valid for the larger values of H/R. Goldman et al.'s result has been used in calculating the drag force and torque on a spherical cell attached on the bottom of a flow cell [33].

At the Reynolds number not less than unity, the drag force on the spherical particle will increase with an introduction of the inertia effect. According to Goldman et al., the shear Reynolds number defined as

$$\mathrm{Re} = \frac{\rho R^2 \dot{\gamma}}{\mu}. \tag{B.3}$$

plays a role as an independent parameter to reflect the convective inertia effect of the flow [31]. This definition is used for Eq. 5.13. Regarding the drag force correction factor for the finite Reynolds number, the study of Zeng et al. was introduced in Section 5.4.3 [115].

B.2 Poiseuille flow

When it comes to zero Reynolds number Poiseuille flow past a solid sphere fixed between two stationary walls, the flow induces the drag force and torque given as Eq. 5.11. For $H/(2h) = 0.25$, i.e., when the sphere center is located at a quarter of the channel height from a closer wall, Wakiya obtained the following correction

factors [110]:

$$F^p = \frac{\frac{3}{4}\left[1 - \frac{1}{9}\left(\frac{R}{H}\right)^2\right]}{1 - 0.6526\left(\frac{R}{H}\right) + 0.3160\left(\frac{R}{H}\right)^3 - 0.242\left(\frac{R}{H}\right)^4} \qquad (B.4)$$
$$T^p = \frac{1}{4}\left(\frac{R}{H}\right)\left[1 + 0.0758\left(\frac{R}{H}\right) + 0.049\left(\frac{R}{H}\right)^2\right].$$

When the sphere contacts the closer wall ($R = H$) while its center is fixed, these factors become $F^p = 1.5820$ and $T^p = 0.2812$.

Ganatos et al. obtained exact solutions for two-dimensional Poiseuille flow past a stationary sphere located between two parallel planes based on their three-dimensional boundary collocation theory, and then they suggested values of the two correction factors as a function of $H/(2h)$ and R/H [29]. According to their result, the drag force on the sphere decreases as h/R increases, and the maximum drag force occurs when the sphere is located at the center-line of the two-dimensional channel. Regarding the torque, the sphere experiences zero torque at the center-line because of symmetry while the torque increases in an almost linear fashion as $H/(2h)$ decreases. However, Ganatos et al. did not suggest values of F^p and T^p for the limiting case of $R/H = 1$.

Brooks and Tozeren used a finite-difference method (FDM) to simulate the three-dimensional laminar flow in a parallel-plate flow channel of which the bottom plate has an array of uniformly aligned spheres [14]. They argued that Goldman et al.'s solution for the simple shear flow can be used when $R/(2h) < 1/15$ and that the solution begins to overestimate the drag force and torque as R increases. Furthermore, Brooks and Tozeren showed that the flow-induced drag force depends on relative positions among spheres as introduced in Section 5.4.3. Therefore, caution should be exercised when study results on a single sphere in Poiseuille flow is applied to multiple spheres. Regarding the hydrodynamic interaction among particles, Sugihara-Seki and Skalak suggested a criterion for negligible interaction as introduced in Section 5.4.3 [100]. Moreover, Sugihara-Seki suggested that the flow-induced drag force and torque depend more on the height of a particle rather than on the detailed shape of the

particle [99].

On the other hand, Poiseuille flow of the interest can be represented with semi-infinite unidirectional flow parallel to a plane wall. To calculate correction factors for the drag force and torque, Pozrikidis expressed unperturbed unidirectional shear flow along the streamwise direction (the x-axis) as

$$V^{\infty} = \dot{\gamma}_w z + \frac{1}{2\mu}\frac{dp}{dx}z^2 \tag{B.5}$$

where $\dot{\gamma}_w$ is the shear rate at the plane wall ($z = 0$) [76]. When $dp/dx = -2\mu\dot{\gamma}_w/(2h)$, V^{∞} becomes zero at $z = 2h$, so the flow can be an approximation to Hagen-Poiseuille flow in a channel of height $2h$. With this flow velocity profile, Pozrikidis suggested the correction factor correlations shown as Eq. 5.12.

Pasol et al. had a similar approach using the bipolar coordinates technique [73]. They used the most general form of second-order polynomial for unperturbed velocity field given as

$$V^{\infty} = k_s z + k_q z^2 + 2k_m yz \tag{B.6}$$

where k_s, k_q and k_m are constants (s: shear flow, q: quadratic flow, m: modulated shear flow), and the y-axis is the spanwise direction. For semi-infinite flow mimicking Poiseuille flow, $k_s = 2V_{ch}/h$, $k_q = -V_{ch}/h^2$ and $k_m = 0$. Because the linearity of the Stokes equation, forces on a sphere fixed in Poiseuille flow can be obtained by summing forces induced by shear flow and forces induced by quadratic flow as the following:

$$\begin{aligned} F_d &= F_x^s + F_x^q = 6\pi\mu RH\frac{2V_{ch}}{h}f_{xx}^s - 6\pi\mu RH^2\frac{V_{ch}}{h^2}f_{xx}^q \\ T &= T_z^s + T_z^q = 4\pi\mu R^3\frac{2V_{ch}}{h}c_{zx}^s - 8\pi\mu R^3 H\frac{V_{ch}}{h^2}c_{zx}^q \end{aligned} \tag{B.7}$$

where f and c are the dimensionless force and torque in the notation of Pasol et al. Values of these two parameters are suggested as a function of H/R for shear flow in [19] and for quadratic flow in [73]. For the sphere contacting the wall ($H/R = 1$), values of the corresponding dimensionless force and torque are $f_{xx}^s = 1.7006$, $c_{zx}^s = 0.9440$,

$f_{xx}^q = 1.9428$ and $c_{zx}^q = 0.9908$. As a result, correction factors for the drag force and torque are obtained as

$$\begin{aligned} F^p &= 3.4012\Big(\frac{R}{h}\Big) - 1.9428\Big(\frac{R}{h}\Big)^2 \\ T^p &= 0.9440\Big(\frac{R}{h}\Big) - 0.9908\Big(\frac{R}{h}\Big)^2. \end{aligned} \tag{B.8}$$

As discussed in Section 5.4.3, the correction factor correlations of Pasol et al. agree well with those of Pozrikidis, and all of them show a good agreement with Staben et al.'s result in the range of when $R/h < 0.2$ [93, 94].

THIS PAGE INTENTIONALLY LEFT BLANK

Appendix C

Relaxation of *Vorticella convallaria*

C.1 Introduction

The relaxation of *Vorticella convallaria* is quite different from its contraction in many aspects. Relaxation is much slower than contraction: relaxation takes several seconds while contraction takes several milliseconds. The driving force of relaxation is the elastic restoring force of the deformed sheath, not from the spasmoneme [2]. Studies using extracted models showed that the stalk length course of relaxation is different from that of contraction: the contraction-relaxation cycle of *Vorticella* has hysteresis [72]. It seems that ATP is consumed during relaxation to pump back calcium ions released for contraction to storage sites [79].

Japanese researchers studied relaxation of *Carchesium polypinum* experimentally in 1950s. Ueda showed that the relaxation speed of *Carchesium* increased as the temperature increased [102]. Sugi observed that relaxation began from the stalk base and propagated toward the zooid [95]. Having immobilized locally or severed the stalk, Sugi measured the propagation of relaxation and found that the relaxation of a certain point of the stalk occurred at similar time after contraction to that of the normal stalk. This observation led Sugi to think that the relaxation phase is not a passive process.

Under tension applied externally, relaxation takes longer time. This is opposite to usual expectation because the tension is applied in the direction of relaxation, so the force is expected to help the cell relax faster. Rahat et al. first mentioned this observation from their experiment in which they exerted tension on *Carchesium* by the spring-balance [77]. They conjectured that the active state of the contracted spasmoneme might decay slowly due to the external tension and that the sheath would contribute negligibly to the slowing of relaxation. France also had the same observation [27]. She applied centrifugal force on *Vorticella convallaria* in the direction opposite to contraction to stall contraction and observed that relaxation became slower as she increased the stall force. As mentioned in Section 6.4, I observed that the relaxation of *Vorticella* was prolonged due to the drag force externally applied on the cell.

The relaxation of the contracted stalk is an indispensable phase of *Vorticella*'s contraction which resets the contraction mechanism. In spite of its significance, however, the relaxation phase has been less studied compared to the contraction phase which is more dynamic and powerful. I believe that more attention should be paid on relaxation because studies on relaxation can accelerate our discovery of *Vorticella* contraction mechanism. In this study, I analyzed relaxation characteristics of *Vorticella convallaria* by employing the mass-spring model.

C.2 Mass-spring model

The mass-spring system model was first used by Moriyama et al. to estimate the spring constant of contracting *Vorticella* stalks [67]. I employed the same approach for relaxation. As Figure C-1 shows, the zooid of relaxing *Vorticella* is modeled to be a solid sphere moving away perpendicularly from a rigid plane, and the stalk is modeled to be an elastic spring. Relaxation is so slow that the relaxation-induced flow can be regarded as steady. Furthermore, the Reynolds number defined as

$$\mathrm{Re} = \frac{2\rho R\bar{U}_r}{\mu} \tag{C.1}$$

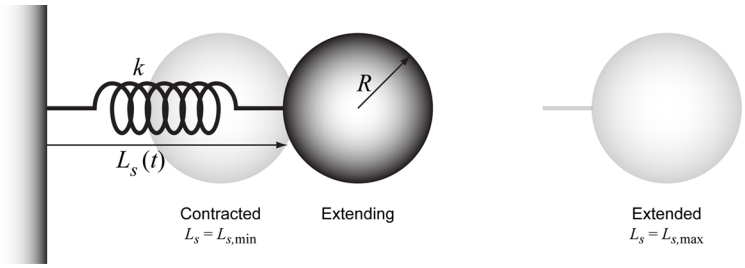

Figure C-1: A mass-spring model for *Vorticella* relaxation.

is much less than unity, so the zooid of relaxing *Vorticella* experiences viscous drag force represented by the Stokes drag formula with the wall effect corrected while any effects from the stalk and other surfaces are ignored. In Eq. C.1, ρ is the density of the medium, R is the radius of the zooid, $\bar{U_r}$ is the mean relaxation speed of *Vorticella* and μ is the viscosity of the medium. Then, from force balance on the zooid, the governing equation is obtained as.

$$m\frac{d^2L_s}{dt^2} = k(L_{s,\max} - L_s) - 6\pi\mu R\lambda\frac{dL_s}{dt} \tag{C.2}$$

where m is the mass of the zooid, L_s is the end-to-end length of the stalk, k is the spring constant of the stalk, $L_{s,\max}$ is the end-to-end length of the fully extended stalk, λ is the wall effect correction factor and t is time. According to the measurement of which the method will be explained later, the inertia term is so small compared to the viscous drag force term that the inertia term is negligible as the following:

$$\frac{\left|m\dfrac{d^2L_s}{dt^2}\right|}{\left|6\pi\mu R\dfrac{dL_s}{dt}\right|} \sim 10^{-3}. \tag{C.3}$$

Therefore, the dynamics of *Vorticella* relaxation is determined by balance between the elastic restoring force of the stalk and the viscous drag force on the zooid with the following initial condition:

$$L_s(t=0) = L_{s,\min} \tag{C.4}$$

The governing equation will result in different solutions depending on how the wall effect correction factor is defined. Brenner and Maude obtained the exact solution of the Stokes drag force on a solid sphere moving slowly toward a rigid plane using the bi-spherical coordinate, respectively [13, 63]. However, as Eq. 3.5 shows, their wall effect correction factor is too complex to be applied for the current model. Instead, I employed the following approximated form of the wall effect correction factor that MacKay and Mason used [58, 59]:

$$\lambda = \frac{R}{L_s}. \tag{C.5}$$

Applying the above correction factor results in the fractional stalk length shown as

$$L_s^* = \frac{L_s - L_{s,\min}}{L_{s,\max} - L_{s,\min}} = 1 - \frac{1}{1 + \frac{L_{s,\min}}{L_{s,\max}}\left[\exp\left(\frac{kL_{s,\max}}{6\pi\mu R^2}t\right) - 1\right]}. \tag{C.6}$$

In addition, I tried another form of the correction factor given as [25, 56]

$$\lambda = 1 + \frac{9}{8}\frac{R}{L_s + R} \tag{C.7}$$

and obtained a more complicated solution shown as

$$\left(\frac{L_s + R}{L_{s,\min} + R}\right)^{\frac{9R}{8(R+L_{s,\max})}} \left(\frac{L_{s,\max} - L_{s,\min}}{L_{s,\max} - L_s}\right)^{\frac{17R+8L_{s,\max}}{8(R+L_{s,\max})}} = \exp\left(\frac{k}{6\pi\mu R}t\right). \tag{C.8}$$

C.3 Relaxation measurement

Relaxation of a few *Vorticella* cells in PVP solution was observed with an inverted bright field microscope (Nikon Eclipse TE300) and a high-speed camera (Photron FASTCAM-PCI). The magnification ratio and numerical aperture of the used objective lens were 20× and 0.45, respectively. Images were captured at 30 fps, and image size is 512×512 pixels. One pixel of images corresponds to 0.79 μm. Cells forming right angle with the substrate were chosen for measurement. The zooid radius and

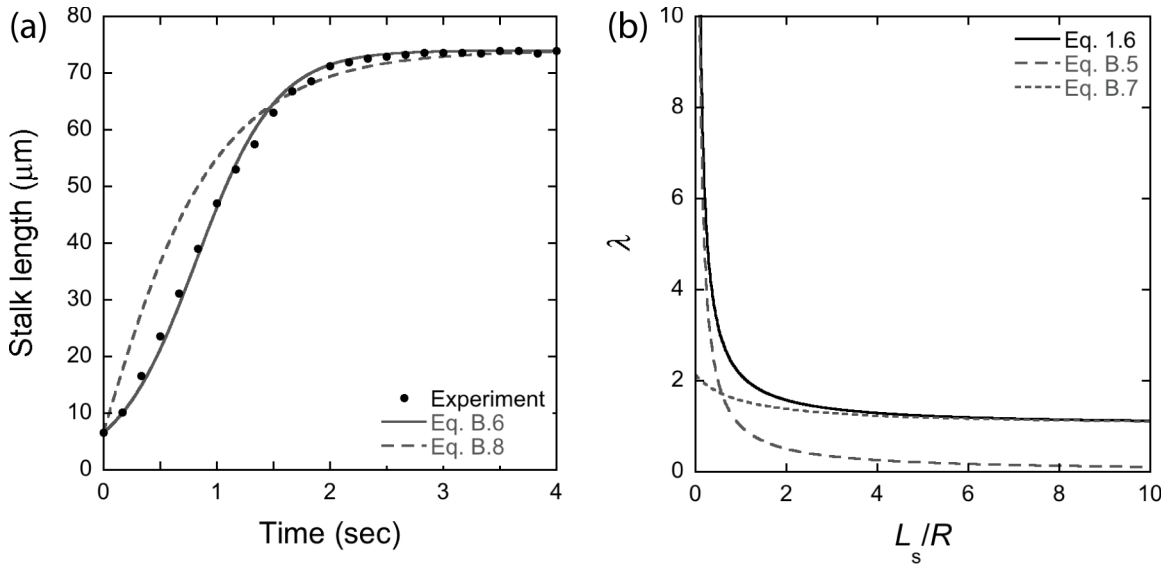

Figure C-2: Verification of relaxation models: (a) Application of relaxation models to *Vorticella* relaxing in water ($k_{\text{Eq.B.6}} = 0.20 \times 10^{-6}$ N/m and $k_{\text{Eq.B.8}} = 0.45 \times 10^{-6}$ N/m). (b) A comparison of wall effect correction factors.

stalk length were measured with MATLAB at every 0.1 sec from the beginning of relaxation. The spring constant of the stalk was obtained by fitting the model over the measured stalk length with the method of least square.

C.4 Spring constant of the relaxing stalk

Figure C-2(a) shows one case of relaxation model application to *Vorticella* relaxing water, and it shows that Eq. C.6 describes relaxation better than Eq. C.8 does. Especially Eq. C.6 shows better performance in describing the stalk length course in the early stage of relaxation in which the wall effect of the substrate is important. This is because Eq. C.5 is close to Brenner's wall effect correction factor (λ in Eq. 3.5) when $L_s \approx 0$ as Figure C-2(b) shows. In contrast, Eq. C.7 is better when $L_s > 4R$, but in this region, the wall effect correction factor is not much greater than unity. Therefore, Eq. C.6 is used to estimate the spring constant of the stalk of relaxing *Vorticella*. On the other hand, it is noticeable that the characteristic time scale of Eq. C.6 ($6\pi\mu R^2/kL_{s,\max}$) includes the length of the fully extended stalk.

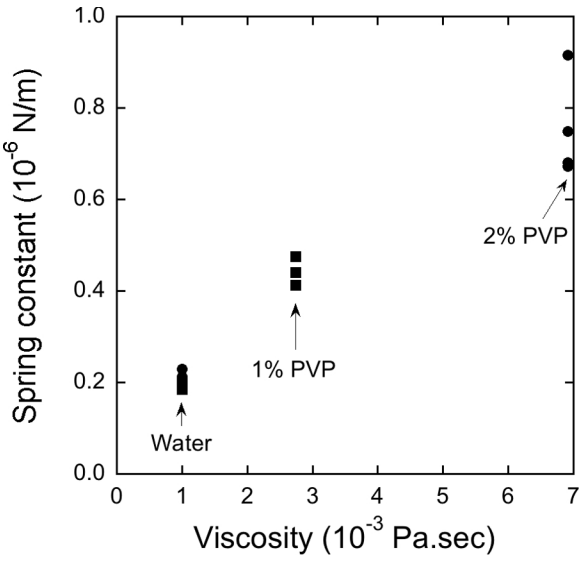

Figure C-3: Estimated spring constant values of the relaxing *Vorticella* stalk.

If the relaxation phase of *Vorticella* is a passive process, characteristic scales of relaxation should not be affected by environment. However, it was already observed that an externally applied stall force increases the relaxation time. Figure C-3 shows that the spring constant of the reextending stalk of several cells increases as the medium viscosity increases. Blue squares of the figure show values of the spring constant obtained from an identical cell in two different viscous media, and the spring constant of the cell's stalk increases in more viscous environment. This supports that the relaxation of *Vorticella* is not a passive process.

C.5 Discussion

In contrast to contraction, acquiring images of normal relaxation is difficult for a few reasons. First, the stalk does not stay in the focal plane of the microscope because the zooid and stalk rotate as the stalk having twisted during contraction untwists. In the case of contraction, the zooid rotates at the end of contraction because contraction is fast. Second, the stalk does not maintain constant orientation with respect to the substrate because of the zooid. In contraction, the stalk pulls the zooid toward the substrate, so the relative orientation between the zooid and

the stalk and between the stalk and the substrate does not change. In contrast, the reextending stalk pushes the zooid away from the substrate, so the zooid rotates with respect to the stalk and it plays as if a rudder. Therefore, the stalk and the zooid cannot keep constant alignment with respect to the stalk. In other words, the zooid of contracting *Vorticella* is similar to a front-wheel drive car on a upslope whereas the zooid of relaxing *Vorticella* is similar to a rear-wheel drive car on a upslope.

THIS PAGE INTENTIONALLY LEFT BLANK

Bibliography

[1] R. D. Allen. Contractility and its control in peritrich ciliates. *J. Eukaryot. Microbiol.*, 20:25–36, 1973.

[2] W. B. Amos. Reversible mechanochemical cycle in the contraction of *Vorticella*. *Nature*, 229:127–128, 1971.

[3] W. B. Amos. Structure and coiling of the stalk in the peritrich ciliates *Vorticella* and *Carchesium*. *J. Cell. Sci.*, 10:95–122, 1972.

[4] W. B. Amos. Contraction and calcium binding in the vorticellid ciliates. In S. Inoué and R. E. Stephens, editors, *Molecules and Cell Movement*, pages 411–435. Raven Press, New York, 1975.

[5] W. B. Amos, L. M. Routledge, and F. F. Yew. Calcium-binding proteins in a vorticellid contractile organelle. *J. Cell. Sci.*, 19:203–213, 1975.

[6] H. Asai. ca^{2+}-driven contraction of spasmoneme in vorticellidae. *Jpn. J. Protozool.*, 38:133–152, 2005.

[7] H. Asai. Structure and function of general motor proteins systems for motility, including the spasmoneme in vorticellidae stalk. *Jpn. J. Protozool.*, 39:104–106, 2006.

[8] H. Asai, T. Ninomiya, R. Kono, and Y. Moriyama. Spasmin and a putative spasmin binding protein(s) isolated from solubilized spasmonemes. *J. Eukaryot. Microbiol.*, 45:33–39, 1998.

[9] H. Asai, T. Ochiai, K. Fukui, M. Watanabe, and F. Kano. Improved preparatioin and cooperative calcium contraction of glycerinated *Vorticella*. *J. Biochem.*, 83(3):795–798, 1978.

[10] I. S. Berezin and N. P. Zhidkov. *Computing methods Volume I*. Addision-Wesley Publishing Company, Inc., Reading, MA, 1st edition, 1965.

[11] D. Boal. *Mechanics of the cell*. Cambridge University Press, New York, NY, 2002.

[12] D. Bray. *Cell movements: from molecules to motility*. Garland, New York, 2001.

[13] H. Brenner. The slow motion of a sphere through a viscous fluid towards a plane surface. *Chem. Eng. Sci.*, 16:242–251, 1961.

[14] S. B. Brooks and A. Tozeren. Flow past an array of cells that are adherent to the bottom plate of a flow channel. *Comp. Fluids*, 25(8):741–757, 1996.

[15] Jr. Buhse, H. E. *Vorticella*: "a cell for all seasons". *J. Euk. Microbiol.*, 45:469–474, 1998.

[16] Jr. Buhse, H. E. and J. C. Clamp. *Vorticella*. In *Encyclopedia of life sciences*. Nature Publishing Group, 2001.

[17] C. Bustamante, J. C. Macosko, and G. J. L. Wuite. Grabbing the cat by the tail: manipulating molecules one by one. *Nat. Rev. Mol. Cell Bio.*, 1:130–136, 2000.

[18] J. Cao, S. Usami, and C. Dong. Development of a side-view chamber for studying cell-surface adhesion under flow conditions. *Ann. Biomed. Eng.*, 25:573–580, 1997.

[19] M. Chaoui and F. Feuillebois. Creeping flow around a sphere in a shear flow close to a wall. *Q. J. Mech. Appl. Math.*, 56(3):381–410, 2003.

[20] J. C. Clamp and D. Williams. A molecular phylogenetic investigation of *Zoothamnium* (ciliophora, peritrichia, sessilida). *J. Eukaryot. Microbiol.*, 53:494–498, 2006.

[21] R. Clift, J. R. Grace, and M. E. Weber. *Bubbles, drops, and particles*. Dover Publications, Inc., Mineola, New York, first edition, 1978.

[22] R. Cox and H. Brenner. The slow motion of a sphere through a viscous fluid towards a plane surface - ii small gap widths, including inertial effect. *Chem. Eng. Sci.*, 22:1753–1777, 1967.

[23] I. Durussel, Y. Blouquit, S. Middendorp, C. T. Craescu, and J. A. Cox. Cation- and peptide-binding properties of human centrin 2. *FEBS Lett.*, 472:208–212, 2000.

[24] J. Fang, B. Zhang, and H. Asai. Chemical modification of contractile 3-nm-diameter filaments in *Vorticella* spasmoneme by diethyl-pyrocarbonate and its reversible renaturation by hydroxylamine. *Biochem. Biophys. Res. Comm.*, 310:1067–1072, 2003.

[25] F. Feuillebois. Some theoretical results for the motion of solid spherical particles in a viscous fluid. In G. F. Hewitt, J. M. Delhaye, and N. Zuber, editors, *Multiphase science and technology*, volume 4, pages 583–789. Hemisphere Publishing Corporation, New York, 1989.

[26] D. A. Fletcher and J. A. Theriot. An introduction to cell motility for the physical scientist. *Phys. Biol.*, 1:T1–T10, 2004.

[27] D. C. France. *Structure and mechanics of the spasmoneme, a biological spring within the protozoan* Vorticella convallaria. PhD thesis, Massachusetts Institute of Technology, Cambridge, MA, 2007.

[28] E. Fuchs, J. S. Jaffe, R. A. Long, and F. Azam. Thin laser light sheet imcroscope for microbial oceanography. *Opt. Express*, 10:145–154, 2002.

[29] P. Ganatos, R. Pfeffer, and S. Weinbaum. A strong interaction theory for the creeping motion of a sphere between plane parallel boundaries. Part 2. Parallel motion. *J. Fluid Mech.*, 99:755–783, 1980.

[30] D. Gogendeau, J. Beisson, N. G. de Loubresse, J.-P. Le Caer, F. Ruiz, J. Cohen, L. Sperling, F. Koll, and C. Klotz. An Sfi1p-like centrin-binding protein mediates centrin-based Ca^{2+}-dependent contractility in *Paramecium tetraurelia*. *Eukaryot. Cell*, 6:1992–2000, 2007.

[31] A. J. Goldman, R. G. Cox, and H. Brenner. Slow viscous motion of a sphere parallel to a plane wall - ii couette flow. *Chem. Eng. Sci.*, 22:653–660, 1967.

[32] A. M. Gordon, A. F. Huxley, and F. J. Julian. The variation in isometric tension with sarcomere length in vertebrate muscle fibers. *J. Physiol.*, 184:170–192, 1966.

[33] D. A. Hammer and D. A. Lauffenburger. A dynamical model for receptor-mediated cell adhesion to surfaces. *Biophys. J.*, 52:475–487, 1987.

[34] R. B. Hawkes and M. Rahat. Contraction and volume reduction of the glycerolated *Carchesium* spasmoneme: Effects of alkali earth cations. *Experientia*, 32:160–162, 1976.

[35] H. Hoffmann-Berling. Der mechanismus eines neuen, von der muskelkontraktion verschiedenen kontraktionskzyklus. *Biochim. Biophys. Acta*, 27:247–255, 1958.

[36] J. Howard. *Mechanics of motor proteins and the cytoskeleton*. Sinauer Associates, Sunderland, MA, 2001.

[37] S. Inoué, R. A. Knudson, M. Goda, K. Suzuki, C. Nagano, N. Okada, H. Takahashi, K. Ichie, M. Iida, and K. Yamanaka. Centrifuge polarizing microscope. I. Rationale, design and instrument performance. *J. Microsc.*, 201:341–356, 2001.

[38] S. Inoué and K. R. Spring. *Video microscopy: the fundamentals*. Plenum Press, New York, 2nd edition, 1997.

[39] T. Itabashi, K. Mikami, and H. Asai. Characterization of the *spasmin 1* gene in *Zoothamnium arbuscula* strain kawagoe (protozoa, ciliophora) and its relation to other spasmins and centrins. *Res. Microbiol.*, 154:361–367, 2003.

[40] T. Itabashi, K. Mikami, J. Fang, and H. Asai. Phylogenetic relationships between *Vorticella convallaria* and other species inferred from small subunit rrna gene sequences. *Zool. Sci.*, 19:931–937, 2002.

[41] A. R. Jones and T. L. Jahn. Contraction of protoplasm iv. cinematographic analysis of the contraction of some peritrichs. *J. Cell. Physiol.*, 75:9–20, 1970.

[42] G. Joseph. *Collisional dynamics of macroscopic particles in a viscous fluid*. PhD thesis, California Institute of Technology, Pasadena, CA, 2003.

[43] S. K. Karanfilian and T. J. Kotas. Drag on a sphere in unsteady motion in a liquid at rest. *J. Fluid Mech.*, 87:85–96, 1978.

[44] K. Katoh and M. Kikuyama. An all-or-nothing rise in cytosolic [Ca^{2+}] in *Vorticella* sp. *J. Exp. Biol.*, 200:35–40, 1997.

[45] K. Katoh and Y. Naitoh. A mechanosensory mechanism for evoking cellular contraction in *Vorticella*. *J. Exp. Biol.*, 168:253–267, 1992.

[46] A. S. Khalil, J. M. Ferrer, R. R. Brau, S. T. Kottmann, Noren C. J., M. J. Lang, and A. M. Belcher. Single m13 bacteriophage tethering and stretching. *Proc. Natl. Acad. Sci. USA*, 104:4892–4897, 2007.

[47] J. V. Kilmartin. Sfi1p has conserved centrin-binding sites and an essential function in budding yeast spindle pole body duplication. *J. Cell Biol.*, 162:1211–1221, 2003.

[48] I. Kim, S. Elghobashi, and W. A. Sirignano. On the equation for spherical-particle motion: effect of reynolds and acceleration numbers. *J. Fluid Mech.*, 367:221–253, 1998.

[49] M. Knoblauch and W. S. Peters. Biomimetic actuators: where technology and cell biology merge. *Cell. Mol. Life Sci.*, 61:2497–2509, 2004.

[50] R. Kono, T. Ochiai, and H. Asai. Chemical modification of amino acid residue in glycerinated *Vorticella* stalk and Ca^{2+}-induced contractility. *Cell Motil. Cytoskel.*, 36:305–312, 1997.

[51] T. Kreis and R. Vale, editors. *Guidebook to the cytoskeleton and motor proteins*. Oxford University Press, Oxford, 2nd edition, 1999.

[52] D. A. Lauffenburger and A. F. Horwitz. Cell migration: a physically integrated molecular process. *Cell*, 84:359–369, 1996.

[53] S.W. Lee, S. Sohn, S. H. Ryu, C. Kim, and K. Song. Experimental studies on the axisymmetric sphere-wall interaction in newtonian and non-newtonian fluid. *Korea-Aust. Rheol. J.*, 13:141–148, 2001.

[54] L. Li, W. Song, A. Warren, M. K. Shin, Z. Chen, D. Ji, and P. Sun. Reconsideration of the phylogenetic positions of five peritrich genera, *Vorticella*, *Pseudovorticella*, *Zoothamnopsis*, *Zoothamnium*, and *Epicarchesium* (ciliophora, peritrichia, sessilida), based on small subunit rrna gene sequences. *J. Eukaryot. Microbiol.*, 55:448–456, 2008.

[55] S. Li, A. M. Sandercock, P. Conduit, C. V. Robinson, R. L. Williams, and J. V. Kilmartin. Structural role of Sfi1p-centrin filaments in budding yeast spindle pole body duplication. *J. Cell Biol.*, 173:867–877, 2006.

[56] H. A. Lorentz. A general theorem concerning the motion of a viscous fluid and a few consequences derived from it. *Versl. Kon. Akad. Wet. Amst.*, 5:168–175, 1897.

[57] J. J. Maciejewski, E. J. Vacchiano, S. M. Mccutcheon, and Jr. Buhse, H. E. Cloning and expression of a cDNA encoding a *Vorticella convallaria* spasmin: an EF-hand calcium-binding protein. *J. Eukaryot. Microbiol.*, 46:165–173, 1999.

[58] G. D. M. MacKay and S. G. Mason. Approach of a solid sphere to a rigid plane interface. *J. Coll. Sci.*, 16:632–635, 1961.

[59] G. D. M. MacKay, M. Suzuki, and S. G. Mason. Approach of a solid sphere to a rigid plane interface. Part 2. *J. Coll. Sci.*, 18:103–104, 1963.

[60] L. Mahadevan and P. Matsudaira. Motility powered by supramolecular springs and ratchets. *Science*, 288:95–99, 2000.

[61] W. F. Marshall. Don't blink: observing the ultra-fast contraction of spasmonemes. *Biophys. J.*, 94:4–5, 2008.

[62] J. Martinez-Sanz, A. Yang, Y. Blouquit, P. Duchambon, L. Assairi, and C. T. Craescu. Binding of human centrin 2 to the centrosomal protein hsfi1. *FEBS J.*, 273:4504–4515, 2006.

[63] A. D. Maude. End effects in a falling-sphere viscometer. *Br. J. Appl. Phys.*, 12:293–295, 1961.

[64] C. D. Meinhart, S. T. Wereley, and M. H. B. Gray. Volume illumination for two-dimensional particle image velocimetry. *Meas. Sci. Technol.*, 11:809–814, 2000.

[65] L. M. Milne-Thomsom. *Theoretical hydrodynamics*. Macmillan & Co, Ltd., London, UK, fifth edition, 1968.

[66] R. B. Moreton and W. B. Amos. Electrical recording from the contractile ciliate *Zoothamnium geniulatum* ayrton. *J. Exp. Biol.*, 83:159–167, 1979.

[67] Y. Moriyama, S. Hiyama, and H. Asai. High-speed video cinematographic demonstration of stalk and zooid contraction of *Vorticella convallaria*. *Biophys. J.*, 74:487–491, 1998.

[68] Y. Moriyama, H. Okamoto, and H. Asai. Rubber-like elasticity and volume change in the isolated spasmoneme of giant *Zoothamnium* sp. under Ca^{2+}-induced contraction. *Biophys. J.*, 76:993–1000, 1999.

[69] Y. Moriyama, K. Yasuda, S. Ishiwata, and H. Asai. Ca^{2+}-induced tension development in the stalks of glycerinated *Vorticella convallaria*. *Cell Motil. Cytoskel.*, 34:271–278, 1996.

[70] M. Nagai, M. Kumemura, H. Asai, and H. Fujita. Binding of artificial object to *Vorticella* for a microsystem powered by a microorganism. *e-J. Surf. Sci. Nanotech.*, 7:673–676, 2009.

[71] Moeto Nagai, Masamichi Oishi, Marie Oshima, Hiroshi Asai, and Hiroyuki Fujita. Three-dimensional two-component velocity measurement of the flow field induced by the *Vorticella picta* microorganism using a confocal microparticle image velocimetry technique. *Biomicrofluidics*, 3(1):014105, 2009.

[72] T. Ochiai, H. Asai, and K. Fukui. Hysteresis of contraction-extension cycle of glycerinated *Vorticella*. *J. Protozool.*, 26(3):420–425, 1979.

[73] L. Pasol, A. Sellier, and F. Feuillebois. A sphere in a second degree polynomial creeping flow parallel to a wall. *Q. J. Mech. Appl. Math.*, 59(4):587–614, 2006.

[74] D. J. Pattersion. Habituation in a protozoan *Vorticela convallaria*. *Behaviour*, 45:304–311, 1973.

[75] R. E. Pepper, M. Roper, S. Ryu, P. Matsudaira, and H. A. Stone. Eddies near microscopic filter feeders are due to the influence of boundaries. In preparation, 2009.

[76] C. Pozrikidis. Effect of pressure gradient on viscous shear flow past an axisymmetric depression or protuberance on a plane wall. *Comp. Fluids*, 29:617–637, 2000.

[77] M. Rahat, Y. Pri-Paz, and I. Parnas. Properties of stalk-'muscle' contractions of *Carchesium* sp. *J. Exp. Biol.*, 58:463–471, 1973.

[78] L. M. Routledge, W. B. Amos, B. L. Gupta, T. A. Hall, and T. Weis-Fogh. Microprobe measurements of calcium binding in the contractile spasmoneme of a vorticellid. *J. Cell. Sci.*, 19:195–201, 1975.

[79] L. M. Routledge, W. B. Amos, F. F. Yew, and T. Weis-Fogh. New calcium-binding contractile proteins. In R. Goldman, T. Pollard, and J. Rosenbaum, editors, *Cell motility book A: motility, muscle and non-muscle cells*, pages 93–113. Cold Spring Harbor Laboratory, 1976.

[80] J. L. Salisbury. Centrin, centrosomes, and mitotic spindle poles. *Curr. Opin. Cell Biol.*, 7:39–45, 1995.

[81] J. L. Salisbury. Roots. *J. Euk. Microbiol.*, 45:28–32, 1998.

[82] J. L. Salisbury. Centrosomes: Sfi1p and centrin unravel a structural riddle. *Current Biology*, 14:R27–R29, 2004.

[83] I. F. Sbalzarini and P. Koumoutsakos. Feature point tracking and trajectory analysis for video imaging in cell biology. *J. Struct. Biol.*, 151:182–195, 2005.

[84] E. Schiebel and M. Bornens. In search of a function for centrins. *Trends Cell Biol.*, 5:197–201, 1995.

[85] W. R. Schneider and R. N. Doetsch. Effect of viscosity on bacterial motility. *J. Bacteriol.*, 117:696–701, 1974.

[86] J. H. Shin, L. Mahadevan, G. S. Waller, L. Langsetmo, and P. Matsudaira. Stored elastic energy powers the 60-μm extension of the *Limulus polyphemus* sperm actin bundle. *J. Cell Biol.*, 162:1183–1188, 2003.

[87] J. H. Shin, B. K. Tam, R. R. Brau, M. J. Lang, L. Mahadevan, and P. Matsudaira. Force of an actin spring. *Biophys. J.*, 92:3729–3733, 2007.

[88] H. Shiono, R. Hara, and H. Asai. Spontaneous membrane potential changes associated with the zooid and vacuolar contractions in *Vorticella convallaria*. *J. Protozool.*, 27(1):83–87, 1980.

[89] H. Shiono and Y. Naitoh. Cellular contraction precedes membrane depolarization in *Vorticella convallaria*. *J. Exp. Biol.*, 200:2249–2261, 1997.

[90] T. J. B. Simons. Vanadate - a new tool for biologists. *Nature*, 281:337–338, 1979.

[91] M. A. Sleigh and D. Barlow. Collection of food by *Vorticella*. *Trans. Am. Microsc. Soc.*, 95:482–486, 1976.

[92] J. R. Sotelo and O Trujillo-Cenóz. The fine structure of an elementary contractile system. *J. Biophys. Biochem. Cytol.*, 6:126–127, 1959.

[93] M. E. Staben, A. Z. Zinchenko, and R. H. Davis. Motion of a particle between two parallel plane walls in low-reynolds-number poiseuille flow. *Phys. Fluids*, 15(6):1711–1733, 2003.

[94] M. E. Staben, A. Z. Zinchenko, and R. H. Davis. Erratum: "motion of a particle between two parallel plane walls in low-reynolds-number poiseuille flow". *Phys. Fluids*, 16(11):4206, 2004.

[95] H. Sugi. Contraction and relaxation in the stalk muscle of *Carchesium*. *Annot. Zool. Jpn.*, 32:163–169, 1959.

[96] H. Sugi. Propagation of contraction in the stalk muscle of *Carchesium*. *J. Fac. Sci. Univ. Tokyo Section IV: Zoology*, 8:603–615, 1960.

[97] H. Sugi. Volume change during contraction in the stalk muscle of *Carchesium*. *J. Fac. Sci. Univ. Tokyo Section IV: Zoology*, 9:155–170, 1961.

[98] H. Sugi. Molecular mechanism of actin-myosin interaction in muscle contraction. In H. Sugi, editor, *Muscle contraction and cell motility: Molecular and cellular aspects*, volume 12 of *Advances in Comparative and Environmental Physiology*, pages 132–171. Springer-Verlag, 1992.

[99] M. Sugihara-Seki. Flow around cells adhered to a microvessel wall. I. Fluid stresses and forces acting on the cells. *Biorheology*, 37:341–359, 2000.

[100] M. Sugihara-Seki and R. Skalak. Force acting on spheres adhered to a vessel wall. *Biorheology*, 34(4/5):249–260, 1997.

[101] M. C. Thompson, T. Leweke, and K Hourigan. Sphere-wall collisions: vortex dynamics and stability. *J. Fluid Mech.*, 575:121–148, 2007.

[102] K. Ueda. Studies on the stalk muscle of *Carchesium* (I). *Zool. Mag.*, 61:367–371, 1952.

[103] K. Ueda. Electric stimulation of the stalk muscle of *Carchesium* II. *Zool. Mag.*, 63:9–14, 1954.

[104] A. Upadhyaya, M. Baraban, J. Wong, P. Matsudaira, A. van Oudenaarden, and L. Mahadevan. Power-limited contraction dynamics of *Vorticella convallaria*: an ultrafast biological spring. *Biophys. J.*, 94:265–272, 2008.

[105] E. Vacchiano, A. Dreisbach, D. Locascio, L. Castaneda, T. Vivian, and Jr. Bushe, H. E. Morphogenetic transitions and cytoskeletal elements of the stalked zooid and the telotroch stages in the peritrich ciliate *Vorticella convallaria*. *J. Protozool.*, 39:101–106, 1992.

[106] E. J. Vacchiano, J. L. Kut, M. L. Wyatt, and H. E. Bushe. A novel method for mass-culturing *Vorticella*. *J. Protozool.*, 38:608–613, 1991.

[107] S. Vogel. *Life in moving fluids: the physical biology of flow*. Princeton University Press, Princeton, NJ, 2nd edition, 1994.

[108] K. Vopel, C. H. Reick, G. Arlt, M. Pöhn, and J. Ott. Flow microenvironment of two marine peritrich ciliates with ecobiotic chemoautotrophic bacteria. *Aquat. Microb. Ecol.*, 29:19–28, 2002.

[109] L. Wakaba and S. Balachandar. On the added mass force at finite reynolds and acceleration numbers. *Theor. Comput. Fluid Dyn.*, 21:147–153, 2007.

[110] S. Wakiya. Effect of a submerged object on a slow viscous flow (Report VII). Two spheres and a plane wal. *Res. Rept. Fac. Engng. Niigata Univ.*, 9:31, 1960.

[111] T. Weis-Fogh and W. B. Amos. Evidence for a new mechanism of cell motiliy. *Nature*, 236:301–304, 1972.

[112] F. M. White. *Viscous fluid flow*. McGraw-Hill, Inc., New York, NY, second edition, 1991.

[113] R. M. Wu and D. J. Lee. Hydrodynamic drag force exerted on a highly porous sphere moving towards an impermeable plate. *Chem. Eng. Sci.*, 53:3571–3578, 1998.

[114] F. Yang. *Interaction law for a collision between two solid particles in a viscous liquid*. PhD thesis, California Institute of Technology, Pasadena, CA, 2006.

[115] L. Zeng, F. Najjar, S. Balachandar, and P. Fischer. Forces on a finite-sized particle located close to a wall in a linear shear flow. *Phys. Fluids*, 21(3):033302–1–18, 2009.

[116] J. Zhang, L. Fan, C. Zhu, R. Pfeffer, and D. Qi. Dynamic behavior of collision of elastic spheres in viscous fluids. *Pow. Tech.*, 106:98–109, 1999.